Observatório Nacional

TESE DE DOUTORADO

DARK DEGENERACY: THEORETICAL AND OBSERVATIONAL ASPECTS

DINORAH BARBOSA DA FONSECA TEIXEIRA

RIO DE JANEIRO
2024

Ministério da Ciência, Tecnologia, Inovações e Comunicações
Observatório Nacional
Programa de Pós-Graduação

Tese de Doutorado

DARK DEGENERACY: THEORETICAL AND OBSERVATIONAL ASPECTS

por

Dinorah Barbosa da Fonseca Teixeira

Tese submetida ao Corpo Docente do Programa de Pós-graduação em Astronomia do Observatório Nacional, como parte dos requisitos necessários para a obtenção do Grau de Doutor em Astronomia.

Orientador: Dr. Jailson Souza de Alcaniz

Rio de Janeiro, RJ – Brasil
Outubro de 2024

B837 Barbosa da Fonseca Teixeira, Dinorah
Dark degeneracy: theoretical and observational aspects [Rio de Janeiro] 2024.
xviii, 111 p. 29,7 cm: graf. il. tab.

Tese (doutorado) - Observatório Nacional - Rio de Janeiro, 2024.

1. Cosmologia. 2. Degenerescência no setor escuro. 3. Energia escura. 4. Matéria escura. I. Observatório Nacional. II. Título.

CDU 000.000.000

“DARK DEGENERACY: THEORETICAL AND OBSERVATIONAL ASPECTS”

DINORAH BARBOSA DA FONSECA TEIXEIRA

TESE SUBMETIDA AO CORPO DOCENTE DO PROGRAMA DE PÓS-GRADUAÇÃO EM ASTRONOMIA DO OBSERVATÓRIO NACIONAL COMO PARTE DOS REQUISITOS NECESSÁRIOS PARA A OBTENÇÃO DO GRAU DE DOUTOR EM ASTRONOMIA.

Aprovada por:

Dr. Jailson Souza de Alcaniz – Observatório Nacional (Orientador)

Dr. Carlos André Paes Bengaly Júnior – ON

Dr. Rodrigo de Sousa Gonçalves – UFRRJ, ON

Dr. José Carlos Neves de Araújo – INPE

Dr. Raimundo Silva Júnior – UFRN

Dr. Humberto de Almeida Borges – UFBA

RIO DE JANEIRO, RJ – BRASIL
31 DE OUTUBRO DE 2024

I am no longer accepting the things I cannot change. I am changing the things I cannot accept.

Angela Davis

Acknowledgments

Pursuing a doctorate degree goes much beyond obtaining a diploma. To me, doing a doctorate has brought me questioning my own life. My academic career, my worth as a person and as a scientist. For a long time, I thought that better than going forth, was leaving everything behind. Something that was severely worsened by the fact that I started this post-grad in the beginning of a pandemic, in a strange city. My husband always said “Don’t worry. The product of the doctorate is the doctor, not the work". Thus, here we are, a bit more than four years later. Today I am proud of the mere fact that this work even exists, something I thought it was impossible until two years ago, given my mental health struggles. What you have in your hands is not a reflection of the best I could’ve done, but a testament of my resistance and stubbornness to get here. It is a reflection of who I am today, which doesn’t necessarily represents who I can become in the future. Mostly, the success in this conclusion is thanks to the fact that I was in great company. That being said, I’d like to thank first and foremost my eternal partner, Marcus Prado. I hope that the rest of our lives is enough for me to thank you for saving mine. To my recently deceased grandma, Inês, who dedicated a lot of time to me and my sister. To my beloved mother, Izolda, and also my father, George, for always encouraging my interest in science and have offered me unconditional support to pursuing an academic career. To my sister, Irene, with who I shared the good, the bad and the ugly. To all my pets, Laika, Bife, Mini Gata, Yoda, Nobara and Megumi. Also to my foster pets, Fumaça, Pipoca, Twix and Tina. To all my friends in Aracaju, but specially to Yonã, Kássia and Renata, for whom I have a care for that it’s impossible to put into words and who saw me become the person I am today. To all my friends in Rio de Janeiro, but specially to my friends at Casa Branca: Thaís, Ellen, Mariana, Fernanda, Rodolpho, Jonatã, Ester, Feliphe, Thiago, Madalena, Christiane, Shao, Jaiane, Danilo, Karyne, Sousa, Rayff, Ayslana, Bruno Wesley, Larissa, Gabriel, and of course, the feline Tangerina. The experience of becoming a PhD was incredibly joyful thanks to all of you. I’d also like to thank my friends Pedro Bessa, Larissa Inácio and Flávia Crossetti for sharing laughs and tears of the academic life with me. To my advisor, Jailson Alcaniz, who chose to advise me during such a crucial moment in my life. To Rodrigo von Marttens, whose support was fundamental to the realization of this research, and that never denied helping me when necessary. To my research group at Observatório Nacional, full of

incredible, empathetic people, some of which have become great friends, for showing me that academia can be healthy and enjoyable. To my parents in law, Cláudia and Marcos, whom I'm proud to call family. To my psychologist, Tiala, that accompanied me through this difficult time. To Hideaki Anno, for changing my life. To Gege Akutami, for writing something so twisted and cruel that made me work even harder on my thesis just so I didn't have to think about it. To CAPES, for funding the scholarship. To Observatório Nacional, for giving me the opportunity to be a part of this institution. Finally, I'd like to thank the examination committee members for taking their time to read this work.

To my father, thank you. To my mother, farewell. And to all the children...congratulations!

Resumo

O fato de que as equações de campo de Einstein conectam a geometria do espaço-tempo à contribuição total dos componentes escuros do substrato cósmico, ao invés de suas contribuições individuais, pode ser entendido como uma degenerescência no setor escuro do Universo. Consequentemente, modelos cosmológicos que apresentam decomposições distintas do setor escuro, mantendo valores idênticos da soma dos componentes escuros do tensor energia-momento, permanecem indistinguíveis mediante observações baseadas em medidas de distâncias. Nesta tese, investigamos aspectos cosmológicos dessa degenerescência do setor escuro no contexto de duas abordagens: (i) um vácuo interagente; (ii) um modelo de energia escura dinâmica. No primeiro trabalho, derivamos e estudamos alguns aspectos físicos de uma parametrização dinâmica uniparamétrica da energia escura, obtida a partir de um modelo interagente de gás de Chaplygin generalizado não adiabático. Determinamos que este modelo dinâmico não admite valores de energia escura fantasma. Realizamos uma análise de seleção de parâmetro utilizando os mais recentes dados observáveis disponíveis publicamente, como os dados do Planck 2018, eBOSS DR16, Pantheon e KiDS-1000. Sob essa análise, nós avaliamos como nosso modelo responde à tensão de $S_8 \equiv \sigma_8(\Omega_m/0.3)^{0.5}$, uma quantidade cosmológica associada ao crescimento de perturbações cosmológicas. Encontramos que os dados de radiação cósmica de fundo (CMB) impõe fortes vínculos para este modelo e concluímos que a tensão de S_8 pode ser aliviada apenas para valores de parâmetros para os quais o modelo se aproxima do ΛCDM. No segundo trabalho, exploramos a possibilidade de romper essa degenerescência através da utilização de medidas de fração de massa de gás observada em aglomerados galácticos gravitacionalmente relaxados e massivos. Esses dados são particularmente interessantes para esse propósito, visto que eles isolam a contribuição de matéria, possivelmente permitindo uma quebra da degenerescência. Estudamos o caso especial do wCDM e sua contrapartida interagente. Comparamos os resultados obtidos para as duas descrições do setor escuro com uma análise não-paramétrica obtida através de Processos Gaussianos. Apesar de que essa degenerescência pode ter sido desfeita do ponto de vista téorico, encontramos que os dados atuais de fração de massa de gás aparentam ser insuficientes para uma conclusão determinante sobre qual cenário cosmológico é favorecido, mesmo quando combinado com medidas de Supernova tipo Ia (SN Ia), Oscilações Acústicas de Bárions (BAO) e CMB.

Abstract

The fact that Einstein's equations connect the space-time geometry to the total dark content of the cosmic substratum, but not to individual contributions of its constituents, can be translated into a degeneracy in the cosmological dark sector. Consequently, cosmological models featuring distinct decompositions within the dark sector, while sharing identical values for the sum of dark components' energy-momentum tensor, remain indistinguishable when assessed through observables based on distance measurements. In this thesis, we investigate cosmological aspects of this degeneracy in the dark sector in the context of two approaches: (i) an interacting vacuum; (ii) a dynamical dark energy model. In the first work, we derive and study some physical aspects of a varying one-parameter dynamical DE parameterization, obtained from an interacting non-adiabatic generalized Chaplygin gas (gCg) model. We find that this dynamical model does not allow phantom crossing. We perform a parameter selection using the most recent publicly available data, such as the data from Planck 2018, eBOSS DR16, Pantheon and KiDS-1000. In light of this analysis, we assess how our model responds to the $S_8 \equiv \sigma_8(\Omega_m/0.3)^{0.5}$ tension, a quantity associated to the growth of cosmological perturbations. We find that the data for the cosmic radiation background (CMB) impose strong constraints on the model and conclude that the S_8 tension can be alleviated only for values of the model parameters very close to the ΛCDM cosmology. In the second work, we explore the possibility of breaking this degeneracy by using measurements of the gas mass fraction observed in massive and relaxed galaxy clusters. This data is particularly interesting for this purpose because it isolates the matter contribution, possibly allowing the degeneracy breaking. We study the particular case of the wCDM model with its interactive counterpart. We compare the results obtained from both descriptions with a non-parametric analysis obtained through Gaussian Process. Even though the degeneracy may be broken at background level from the theoretical point of view, we find that current gas mass fraction data seems to be insufficient for a final conclusion about which approach is favored, even when combined with Supernovae type Ia (SN Ia), Baryon Acoustic Oscillations (BAO) and CMB measurements.

List of Figures

List of Tables

Contents

Introduction

Since the dawn of mankind, we looked up to the sky, wondering about our existence within the *cosmos*. As humanity evolved, so did our questions: "Is the Universe infinite in time? Or did it have a beginning?" "What is it made of?" "Do we exist in a special place in the Universe?". This study of the origin, properties and evolution of the Universe constitutes the cosmology. Bounded by our scientific development, questions about our Universe remained in the realm of philosophical discussions for centuries. It was in 1915 that Albert Einstein revolutionized cosmology by developing the general relativity theory (GR) [1]. In its proposal, the GR portrays time and three-dimensional space as a single entity, the spacetime, while gravity is interpreted as the curvature of said spacetime. This concept was fundamental to explain some local properties at larger scales, including the correction of Mercury's orbit in our own solar system [2]. To this day, GR has achieved outstanding success among several observational and experimental tests (see, e.g., [3, 4]). Furthermore, GR was the cornerstone to the first physical description of our Universe. More specifically, Einstein described a static Universe, composed only of matter and curvature in a homogeneous and isotropic spacetime. Interestingly, this model of the Universe, albeit based on the observations at the time, evolved into a calamitous state: without anything to stop matter from clustering, the equations lead to a collapsing Universe. This compelled Einstein to introduce a term in his field equations in order to prevent gravity to triumph. The term in question, Λ, received the name of cosmological constant [5].

However, in 1922, Alexander Friedmann pointed out, from Einstein's field equations, that this disastrous fate of the Universe could be avoided, without the need for a cosmological constant, if one assumes the Universe as dynamic, i.e., that spacetime is allowed to expand and contract [6]. Friedmann was later proved to be correct about his supposition, when Edwin Hubble observed galaxies that were moving with radial velocities proportional to their distances, showing that the Universe was, in fact, expanding [7].

The second half of the 20th century was marked by a succession of important events in cosmology. The first one being the accidental detection of the Cosmic Microwave Background (CMB) [8], an observational snapshot of the primordial Universe, which had already been predicted in the 1940s, by George Gamow, Ralph Alpher and Robert Herman, as a remnant of the process of generation of elements in the early Universe, the

Big Bang nucleosynthesis [9, 10]. Alternatively, in 1970, Vera Rubin and William Kent Ford noticed that the rotation curve of Andromeda galaxy (M31) decreased slower than expected for greater distances from the galactic nucleus, where peculiar motions are expected to be small, indicating the presence of undetectable matter at the halo of such objects [11]. Furthermore, as early as 1933, Fritz Zwicky had already demonstrated, through the virial theorem, that the mass of the Coma galaxy cluster also contained a larger amount of matter (around 400 times more) than the visible matter obtained from astronomical observations [12]. This type of matter, that so far can only be detected by its gravitational effects, is the so-called dark matter (DM), a term coined by Fritz Zwicky himself.

Finally, in the late 90s, two separate observational groups, the High-z Supernovae Search Team and the Supernovae Cosmology Project, independently presented distance measurements obtained from Supernovae Type Ia (SN Ia) that suggested that the Universe was undergoing a period of cosmic acceleration [13, 14]. This scientific discovery, however, was in conflict with the idea of an expanding decelerated Universe accepted at the time. More importantly, there wasn't a cosmic component that could be responsible for generating an accelerated expansion of the current Universe. In light of this newfound evidence, two major routes emerged in the literature. The first one provides modifications to GR, known as modified gravity. The second introduces another "dark" component to the Universe, the dark energy (DE), an exotic constituent with negative pressure which causes the Universe to expand with positive acceleration. On this basis, one particular model gained relevancy in the cosmological scenario: the ΛCDM model.

In the ΛCDM, the dark energy is described by a cosmological constant Λ[1], whose equation of state is $p_\Lambda = -\rho_\Lambda$, with p_Λ and ρ_Λ the pressure and energy density of the fluid, respectively. Furthermore, the remaining letters, "CDM" stand for the dark matter in its non-relativistic, i.e., "cold", form, which is the prevalent form of DM in the Universe. From an observational standpoint, technological innovations in the past 50 years or so, have paved the way for high quality ground and space experiments, allowing us to describe the Universe with astonishing precision. Moreover, the accumulation of such observations were instrumental to the triumph of the ΛCDM as the standard cosmological model [15–21]. In particular, the current measurements place dark energy as contributing with $\sim 70\%$ of the energy density of the Universe, while dark matter corresponds about 25% of the total energy density. The last 5 or so percent are divided between baryonic (i.e., ordinary, non-dark matter) and radiation, the latter with $< 1\%$.

Despite its undeniable success in explaining the observed Universe, there are also instances where the ΛCDM fails, e.g., the notorious cosmological constant problem (CCP) [22], as well as the recent cosmological tensions (see, e.g., [23]). These open

[1]The cosmological constant was conveniently brought back with the discovery of recent acceleration of the Universe.

problems create an urge to explore cosmologies beyond ΛCDM. To some extent, these difficulties arise due to our ignorance concerning the dark sector of the Universe, i.e., the dark matter plus dark energy components. In particular, although we are able to obtain cosmological quantities associated to the dark sector, these measurements are obtained through indirect observations, i.e., through gravitational interactions, meaning we are unable to discern the individual contributions of the dark constituents.

This fact is reflected in Einstein's field equations, and manifests as a degeneracy in the dark sector, the dark degeneracy [24–29]. As a consequence, models degenerated through the dark degeneracy will exhibit indistinguishable features, such as similar expansion rate, $H(z)$. On the other hand, as argued in Ref. [30], the conditions imposed by this degeneracy enable us to construct a mapping between degenerated pairs, providing a route to explore the dark degeneracy.

In this context, the work presented in this thesis aims to investigate the aforementioned aspects of the dark degeneracy, exploring the viability of cosmological degenerated scenarios as well as investigating a route for breaking the degeneracy at background level. In order to provide powerful statistical results, we resort to Monte Carlo techniques (MC), which have become a robust tool for parameter estimation in cosmology, widely used in the majority of cosmological experiments analyses. Following [30], we examine the dark degeneracy through the lens of two approaches. The first one consisting of cold, pressureless, dark matter and a dark energy parameterized by a time-varying equation of state $w_x(a)$. The second approach is the one where we consider a coupling between the dark matter and a cosmological constant $w_x = -1$.

The thesis in question is divided as follows. In Chapter 1, we present an overview of the fundamentals and current state of cosmology. Chapter 2 considers the possibility of an interacting dark sector, which will be relevant when discussing the dark degeneracy. Chapter 3 properly introduces the concept of a degeneracy in the dark sector and presents some cases of degenerated models. Chapters 4 and 5 present the results of our investigations, published in Ref. [31] and [32]. In Chapter 4, we conduct a case study for a dynamical model from an interacting decomposed generalized Chaplygin gas (gCg), using a mapping from interacting to dynamical approach. In Chapter 5, we perform a test to break the dark degeneracy using measurements of gas mass fraction data. Finally, we state our final remarks in Chapter 6.

Chapter 1

The current state of cosmology

Cosmology is an extensive and complex subject. A careful, detailed review of cosmology would take much more than just a single chapter in a book. In this chapter, we merely aim to get acquainted with the necessary concepts and topics discussed through this thesis. Aside from updates from recent cosmological data, everything presented here can be found in standard cosmology textbooks such as [33–35], reviews and lecture notes, e.g., [22, 36] and [37], respectively. This chapter is divided in two parts: in the first one we present the fundamentals of cosmology, starting from the metric and closing with the perturbed equations; the other half is mostly dedicated to the types of information that can be extracted from observations, and how this data affects what we know about the Universe.

1.1 Modern cosmology

1.1.1 The geometry of the Universe

In order to properly introduce the physical properties of the Universe, we must first define the distance between two points in space, that is, the metric. A metric that accurately describes the observed Universe should not only describe a 3-dimensional spacetime, but also incorporate some of its features. For instance, at large scales ($\simeq$ 100Mpc) the Universe is statistically both homogeneous and isotropic. Homogeneity means that the Universe appears the same in every point, while isotropy means it looks the same at every direction (see Fig. 1.1). A homogeneous Universe does not imply an isotropic Universe. However, an isotropic spacetime, along with the supposition that there is no privileged observer in the Universe, necessarily mean that the Universe is homogeneous. The hypothesis that the Universe is both homogeneous and isotropic is formally known as the cosmological principle (CP).

On the other hand, observations from the past century indicated that the Universe itself is expanding [7]. Combining these aforementioned characteristics, the most general

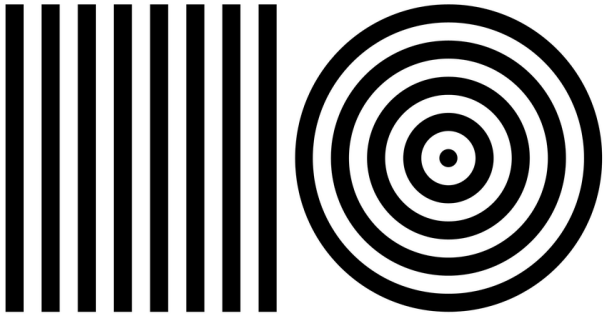

Figure 1.1: **Left:** a homogeneous, but not isotropic space in two dimensions. **Right:** an isotropic, but not homogeneous two-dimensional space . Adapted from [38].

metric to obey Einstein's equations for general relativity while considering the CP and a dynamical Universe is the Friedmann-Lemaître-Robertson-Walker metric, or simply FLRW. In hyperspherical coordinates, the line element for FRLW is given by:

$$ds^2 = -c^2dt^2 + a(t)^2\Big[d\chi^2 + S_k^2(\chi)d\Omega^2\Big], \tag{1.1}$$

$S_k(\chi)$ is given by:

$$S_k(\chi) = \begin{cases} R_0 \sinh(\chi/R_0), & \text{if } k = -1 \\ \chi, & \text{if } k = 0 \\ R_0 \sin(\chi/R_0), & \text{if } k = +1. \end{cases} \tag{1.2}$$

With $d\Omega^2 = d\theta^2 + sin^2(\theta)d\phi^2$ and the chosen metric signature is $(-,+,+,+)$. Here, c is the speed of light[1], t is the cosmic time and $a(t)$ is the scale factor, which is dimensionless. The latter quantifies how much the Universe has expanded (or contracted) with time, and is normalized at the present time: $a(t = t_0) = 1$, with t_0 is the age of the Universe today. Furthermore, since we assume the CP, the curvature of the spacetime is determined by the constant k, which can take values $0, +1$ or -1 for flat, spherical and hyperbolic spaces, respectively. R_0 is the (physical) curvature radius today. χ is the comoving coordinate, and relates to the usual radial coordinate through $d\chi = dr/\sqrt{1 - kr^2/R_0}$. If the observers are in a referential in rest of the cosmic expansion, they are called comoving observers. Since comoving observers experience an uniform expansion, any distance measured within this referential remains constant with time, and is called comoving distance. Additionally, the time measured by a comoving observer is referred to as the proper time.

1.1.2 Distances

In a Universe capable of expanding or contracting, determining distances is not a trivial task. So far, we've seen the comoving distance, χ, that does not change with respect to time. For a time interval dt between the emission of the photon and its detection at t_0,

[1] From now on, $c = 1$

the comoving distance is calculated by

$$\chi(t) = \int_t^{t_0} \frac{dt'}{a(t')}. \tag{1.3}$$

Additionally, we can define the proper distance, d_P:

$$d_P(t) = a(t)\chi, \tag{1.4}$$

which gives us the physical distance at a given time t. Just like physical distances grow with time, the physical wavelength of a photon traveling through the Universe is affected by the Doppler effect. Suppose a photon is emitted at a time t_e with wavelength λ_e and observed today at t_0 with λ_0. The cosmological redshift z caused be the expansion of the Universe will be given by:

$$1 + z = \frac{\lambda_0}{\lambda_e}, \tag{1.5}$$

and is related to the scale factor through

$$a(z) = \frac{1}{1+z}. \tag{1.6}$$

Noticeably, higher redshifts mean we are looking further in the past of the Universe, while we expect the redshift for objects nearby to be close to zero. It is convenient to express distances in terms of the Hubble rate, which is the relative expansion rate of the Universe:

$$H(a) \equiv \frac{\dot{a}}{a}, \tag{1.7}$$

where dot represents the derivative in relation to time t. For the present time, H_0 receives the name of Hubble constant. Therefore, we can rewrite Eqs. 1.3 and 1.4 as the following

$$\chi = \int_0^z \frac{dz'}{H(z')}, \tag{1.8}$$

and

$$d_P = \frac{1}{(1+z)} \int_0^z \frac{dz'}{H(z')}, \tag{1.9}$$

where we have used the relation in Eq. 1.6.

Although the aforementioned comoving and proper distances are equally correct, they represent the distance at a fixed time. Therefore, they are not measurable, since the quantity we are trying to determine is changing in time. In practice, we must be able to determine the distance to an object through observations. One possible way of achieving this is through the luminosity distance.

For luminous objects with uniform energy flow, the flux, that is, the energy/area/time

decays with the square of the distance:

$$F = \frac{L}{4\pi d^2}, \tag{1.10}$$

where L is the luminosity, the energy/time emmitted by the source. Evidently, this distance d increases with time. For the FRLW metric, d is given by the proper distance $S_k(\chi)$, which is called the metric distance, d_M:

$$F = \frac{L}{4\pi d_M^2}. \tag{1.11}$$

Moreover, we must also account for two different effects of the expansion of the Universe in the flux. First, a photon emitted at t_e and detected t_0 looses energy through redshift:

$$\frac{E_0}{E_e} = \frac{h\lambda_e}{h\lambda_0} \Rightarrow \frac{E_0}{E_e} = \frac{1}{(1+z)}, \tag{1.12}$$

where h is the Planck constant. On the other hand, the distance between two consecutive photons emitted increases as they travel across space. Let the initial time separation be δt_e. By the time the photons arrive, the Universe increased $(1 + z)$, and the time separation between the photons will be $\delta t_0 = \delta t_e(1 + z)$. Thus, the rate at which the photons arrive is reduced by $1/(1 + z)$, as is the flux. Finally, the resulting observed flux is

$$F = \frac{L}{4\pi d_M^2 (1+z)^2} = \frac{L}{4\pi d_L^2}. \tag{1.13}$$

Here, d_L is the luminosity distance. The luminosity distance is useful because it relies on the the flux of the observed object in order to obtain distance measurements. However, Eq. 1.13 requires us to know the luminosity of the source L, an intrinsic property, beforehand. That is made possible through objects whose brightness are predictable, known as standard candles. One typical example of standard candles is the type Ia supernovae, an astronomical event caused by a particular set of objects. The physics behind standard candles will be discussed in greater detail in Sec. 1.2.1.

Alternatively, for objects that occupy an angular size in the sky, we can calculate the angular diameter distance, d_A. If the angular size subtended by the source is $\delta\theta$, then

$$\delta\theta = \frac{l}{d_A}, \tag{1.14}$$

with l the true size of the object. We have used the small angle approximation $\sin(\delta\theta) \approx \delta\theta$, which holds for the typical angular sizes in cosmology ($\delta\theta \ll 1$ in radians). Much like we need the standard candles to determine the luminosity distance, for the angular diameter distance we have the so-called standard rulers. Standard rulers represent characteristic scales of the Universe that can be determined through cosmological quantities.

1.1.3 Friedmann equations

The theory of general relativity (GR) defines gravity as a distortion in spacetime caused by the presence of physical constituents of the Universe. This fundamental relation is quantified through Einstein's field equation:

$$G_{\mu\nu} = 8\pi G T_{\mu\nu}, \tag{1.15}$$

with G the universal gravitational constant. $G_{\mu\nu}$ is known as Eintein's tensor:

$$G_{\mu\nu} = R_{\mu\nu} - \frac{1}{2} g_{\mu\nu} R, \tag{1.16}$$

with $R_{\mu\nu}$, R and $g_{\mu\nu}$ are the Ricci's tensor, Ricci's scalar and the metric, respectively. Finally, $T_{\mu\nu}$ is the energy-momentum tensor, a rank 2 tensor that is related to the cosmic components. Once we impose the conditions of spatial symmetry from the cosmological principle, that is, the homogeneity and isotropy, the energy-momentum tensor assumes the simple form of a perfect fluid:

$$T^{\mu}_{\nu} = \begin{bmatrix} -\rho & 0 & 0 & 0 \\ 0 & p & 0 & 0 \\ 0 & 0 & p & 0 \\ 0 & 0 & 0 & p \end{bmatrix}, \tag{1.17}$$

where ρ is the energy density and p is the energy pressure of the fluid. For Eq. 1.17, the relation $T^{\mu}_{\nu} = g^{\mu\lambda} T_{\lambda\nu}$ was used to raise an index. Additionally, for an independent component, the conservation equation applies

$$\dot{\rho} + 3\frac{\dot{a}}{a}\Big(\rho + p\Big) = 0. \tag{1.18}$$

For a perfect fluid, we have the following equation of state (EoS)

$$p = w\rho, \tag{1.19}$$

with w the equation of state parameter. Therefore, the general solution for ρ of the i-th fluid when w is a constant is simply

$$\rho_i(a) = \rho_{i,0} a^{-3(1+w)}. \tag{1.20}$$

Combining Einstein's field equations (Eq. 1.15) with the FRLW metric, we arrive to two equations, the first one being the Friedmann equation

$$\Big(\frac{\dot{a}}{a}\Big)^2 = \frac{8\pi G}{3}\rho - \frac{k}{a^2 R_0^2}. \tag{1.21}$$

The second relation is known as the acceleration equation:

$$\frac{\ddot{a}}{a} = -\frac{4\pi G}{3}\rho\Big(1 + 3w\Big), \tag{1.22}$$

from what it is possible to see that for $w < -1/3$ we have an accelerating Universe, that is, $\ddot{a}/a > 0$.

Equations 1.21 and 1.22, along with Eq. 1.18, are enough to describe the evolution of the Universe at scales where the PC is valid. Here, ρ and p are the total energy density and pressure of all cosmic constituents, that is $\rho = \sum_i \rho_i$, $p = \sum_i p_i$, with subindex i related to the i-th component. Before describing the components of the Universe, it is useful to define the current energy density for a flat Universe ($k = 0$ in Eq. 1.21) as the critical density

$$\rho_{crit} \equiv \frac{3H^2}{8\pi G}, \tag{1.23}$$

as well as the density parameter for the i-th perfect fluid:

$$\Omega_i \equiv \frac{\rho_i}{\rho_{crit}}. \tag{1.24}$$

We can also relate the total density parameter Ω to the curvature of the Universe:

$$\Omega \begin{cases} > 1, & \text{if } k = -1 \\ = 1, & \text{if } k = 0 \\ < 1, & \text{if } k = +1. \end{cases} \tag{1.25}$$

1.1.4 Cosmic components

Friedmann equation, paired with the continuity equation, determine the evolution of the Universe at large scales, where the CP is valid. As we can see, this evolution depends on the constituents of the Universe. Below, we describe three crucial components of the cosmic inventory.

- **Radiation:** We refer to radiation as particles that have ultra-relativistic velocities, for which the kinetic energy dominates. As of today, radiation in the Universe is mostly present in photons but also constituted by a small percentage of relativistic neutrinos. Electrodynamics states that the radiative pressure is one third of the energy density $p_r = 1/3\rho_r$. Thus

  $$w_r = \frac{1}{3}, \tag{1.26}$$

  and solving equation 1.20 for radiation:

  $$\Omega_r = \frac{\Omega_{r,0}a^{-4}}{H^2/H_0^2}. \tag{1.27}$$

- **Non-relativistic matter:** For particles at non-relativistic velocities, the energy density is much larger than the pressure so that we can approximate $p_m = 0$. This applies for baryonic matter[2] and is often used to describe (cold) dark matter as well, as will be detailed later in Sec. 1.2.2. In this case, the matter contribution can be expressed as $\rho_m = \rho_b + \rho_c$ and $p_m = p_b = p_c = 0$, where the subscript b and c represent baryons and cold dark matter, respectively. The solution in terms of the density parameters for matter is

$$\Omega_m = \frac{\Omega_{m,0} a^{-3}}{H^2/H_0^2}. \tag{1.28}$$

- **Cosmological constant:** The cosmological constant, also known as Λ, is defined as an exotic fluid with negative pressure and the following EoS:

$$p_\Lambda = -\rho_\Lambda, \tag{1.29}$$

so that this component is independent of time:

$$\Omega_\Lambda = \frac{\Omega_{\Lambda,0}}{H^2/H_0^2}. \tag{1.30}$$

As aforementioned, a Universe filled with a fluid with $w < -1/3$ will accelerate, such is the case for the cosmological constant. In the standard cosmological model, the cosmological constant is the source of the late time acceleration of the Universe. Furthermore, a natural candidate for Λ is the vacuum energy, as the vacuum is not diluted as spacetime expands or contracts. Although quantum field theory predicts a value for the vacuum energy density, it severely contradicts the current $\rho_{\Lambda,0}$ values from observations (see Sec. 1.2.3).

Finally, a Universe composed by radiation, matter and Λ will have the following Friedmann equation

$$H(a) = H_0 \sqrt{\Omega_{r,0} a^{-4} + \Omega_{m,0} a^{-3} + \Omega_{\Lambda,0} + \Omega_{k,0}}, \tag{1.31}$$

with $\Omega_{k,0} = \frac{-k}{H_0^2 R_0^2} a^{-2}$ the density parameter associated to the curvature. Eq. 1.31 allows us to see that for different values of scale factor, different components dominate the expansion rate of the Universe, as illustrated in Fig. 1.2. Each dominating component defines an epoch. For example, for z from infinity to $\sim 10^4$ we have a Universe dominated by radiation, which later turns into a matter dominated Universe. Crossing points between the curves mark the transition between epochs and when they happen will depend on the

[2]In cosmology, the term baryonic is used to express particles that compose ordinary matter such as protons, neutrons and leptons. This is because the particles of the atomic nuclei are overly massive ($\sim 10^4$ times) in regards to leptons, and therefore the mass contribution for this type of matter is largely dominated by baryons.

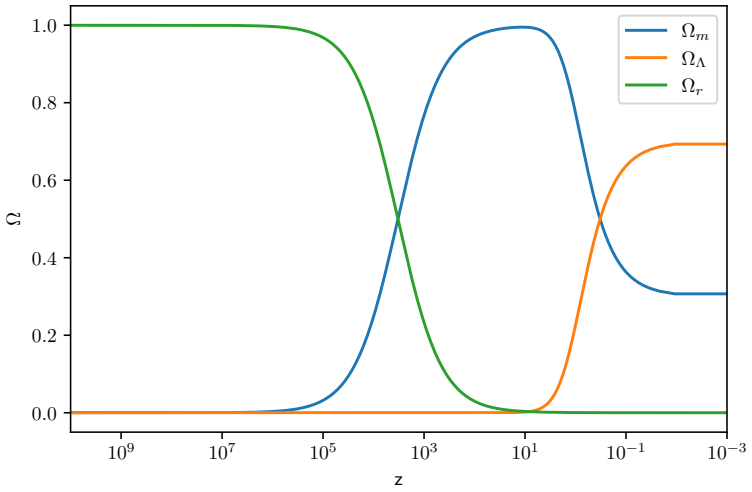

Figure 1.2: Evolution of the components of a flat Universe filled with radiation, matter and the cosmological constant for $\Omega_{c,0} = 0.25$, $\Omega_{\Lambda,0} = 0.70$. Figure made with CLASS code [39].

values of the density parameters of the species. In a general sense, the quantity of every constituent of the Universe will be deeply related to events of the cosmic history, as well as structures of the present Universe. Therefore, the density parameters as well as other equally important parameters, such as H_0, compose the set of cosmological parameters that we need in order to properly describe the Universe.

1.1.5 Perturbed equations

At scales where variations of energy density relative to the mean energy density are small, i.e., $\delta\rho/\rho \ll 1$, inhomogeneities of the Universe become relevant and we must adopt a perturbative cosmological theory. In this section, we briefly introduce the necessary elements for our understanding of structure formation for the dark sector elements. We limit our discussion to the linear level, and consider a flat FRLW metric, that is, $\Omega = 1$, for the background. We refer to the reader to [33] for details on perturbation theory.

The line element (Eq. 1.1) is now:

$$ds^2 = a^2(\tau)[-(1+2A)d\tau^2 + 2B_i dx^i d\tau(\delta_{ij} + 2E_{ij})dx^i dx^j], \tag{1.32}$$

where $\tau = dt/a(t)$ is the conformal time. A, B_i, E_{ij} are functions of (τ, x^i) and can be decomposed into scalar, vector and tensor perturbations. While vector perturbations decay rapidly with the expansion of the Universe, and therefore are not of interest for us, the scalar and tensor perturbations cases must be analyzed separately.

- **Scalar perturbations:** Scalar perturbations of the metric can be described by the conformal Newtonian gauge, for which the line element ds^2 can be expressed in

terms of the gauge-invariant Bardeen potentials Ψ and Φ [40]:

$$ds^2 = a^2(\tau)[-(1+2\Psi)d\tau^2 + (1+2\Phi)d\vec{x}^2], \tag{1.33}$$

with τ is the conformal time. In this gauge, Ψ, Φ act as scalar gravitational potentials. The perturbed energy momentum-tensor of the total fluid is

$$\delta T^0_0 = -\delta\rho, \tag{1.34}$$

$$\delta T^0_i = (\rho + p)v_i, \tag{1.35}$$

$$\delta T^i_j = \delta p\, \delta^i_j + \Sigma^j_i, \tag{1.36}$$

with $\delta\rho$ and δp the perturbations for the energy density and pressure, respectively. v_i, is the total spatial 3-velocity and Σ^i_j the total anisotropic shear perturbation, for which $\Sigma^i_i = 0$. The linear perturbed Einstein equations will provide the following relations in Fourier k-space:

$$-k^2\Phi + 3\mathcal{H}(-\Phi) = 4\pi G a^2 \delta T^0_0, \tag{1.37}$$

$$k^2(-\Phi' + \mathcal{H}(\Psi) = 4\pi G a^2(\rho + p)\theta, \tag{1.38}$$

$$-3\Phi'' + 3\mathcal{H}(\Psi' - 2\Phi') + 3\Big(2\frac{a''}{a} - \mathcal{H}^2\Big)\Psi - k^2(\Phi + \Psi) = 4\pi G a^2 \delta T^i_i, \tag{1.39}$$

$$-k^2(\Phi + \Psi) = 12\pi G a^2(\rho + p)\sigma, \tag{1.40}$$

with prime denoting a derivative in regards to the conformal time and k is the wavenumber. Here, θ and σ are the defined by

$$(\rho + p)\sigma = -(\hat{k}^i\hat{k}_j - \frac{1}{3}\delta^i_j)\Sigma^j_i, \tag{1.41}$$

$$(\rho + p)\theta = ik^j \delta T^0_j. \tag{1.42}$$

For a fluid, Eq. 1.42 is simply the divergence of the fluid velocity

$$\theta = ik^j v_j. \tag{1.43}$$

On the other hand, the perturbed conservation equations for the i-th independent cosmic component are given by the following

$$\delta\rho_i' + 3\mathcal{H}(\delta\rho_i + \delta p_i) + (\rho_i + p_i)(3\Psi' + \theta_i) = 0, \tag{1.44}$$

$$[(\rho_i + p_i)\theta_i]' + (\rho_i + p_i)(4\mathcal{H}\theta_i - k^2\Psi) - k^2\delta p_i + (\rho_i + p_i)k^2\sigma_i = 0. \tag{1.45}$$

We will be interested in describing the evolution of perturbations of the dark sector, therefore, we limit our discussion to these components on this section as well. The conservation equations for are shown bellow.

For CDM, we assume $p_c = \sigma_c = 0$, so the conservation equations become

$$\delta\rho_c' + 3\mathcal{H}\delta\rho_c + \rho_c(3\Phi' + \theta_c) = 0, \tag{1.46}$$

$$\theta_c' + \mathcal{H}\theta_c - k^2\Psi = 0. \tag{1.47}$$

While for a dark energy component with EoS $p_x = w_x\rho_x$, with $w_x < -1/3$, we have

$$\delta\rho_x' + 3\mathcal{H}(\delta\rho_x + \delta p_x) + \rho_x(1 + w_x)(3\Psi' + \theta_x) = 0, \tag{1.48}$$

$$\theta_x' + \frac{w_x'}{1 + w_x}\theta_x + \mathcal{H}(1 - 3w_x)\theta_x - k^2\Psi - \frac{k^2\delta p_x}{\rho_x(1 + wx)} + k^2\sigma_x = 0. \tag{1.49}$$

- **Tensor perturbations:** So far, it has been shown that scalar perturbations are related to the evolution of the energy density perturbation. Tensor perturbations, on the other hand, are responsible for the astrophysical phenomenon of gravitational waves. Considering only tensorial modes of perturbation, the perturbed line element is given by the following

$$ds^2 = a^2(\tau)[-d\tau^2 + (\delta_{ij} + h_{ij}^T dx^i dx^j)], \tag{1.50}$$

with h_{ij}^T the tensor associated to the tensorial perturbations. Assuming perturbations in the x-y plane, h_{ij}^T takes the form [37]:

$$h_{ij}^T = \begin{bmatrix} h_+ & h_\times & 0 \\ h_\times & -h_+ & 0 \\ 0 & 0 & 0 \end{bmatrix}. \tag{1.51}$$

Finally, Einstein equations can be related to the anisotropic stress for tensorial perturbations Π_{ij}^T:

$$h_{ij}^T + 2\mathcal{H}h_{ij}'^T + k^2 h_{ij}^T = 16\pi G a^2 \Pi_{ij}^T. \tag{1.52}$$

When the right side of Eq. 1.52 is zero, that is, in the absence of anisotropic stress, Einsteins equation describe a wave equation, where h_+, $h_\times$ are the wave modes.

1.2 The standard cosmological scenario

We shall now describe the physics behind some of the cosmological probes that are most relevant to the work presented in this thesis.

1.2.1 Cosmological probes

1. **CMB:** In the early Universe, at $\sim 1eV$, photons and baryons were tightly coupled in what can be viewed as a single fluid, the photon-baryon fluid. As the Universe expanded, the interaction rate of the photons via Compton scattering became smaller than the expansion rate of the Universe, causing the photons to decouple from the baryons, thus making the Universe transparent. The thermal radiation remnant from this decoupling form a background known as the cosmic microwave background (CMB).

   The CMB has a blackbody power spectrum and is observed today at radio spectrum with $T_0 \simeq 2.73\,K$ [41]. Aside from the CMB dipole, with $|\delta T/T| \sim 10^{-3}$ at $(l, b) \approx (264°, 48°)$ [42], the CMB is highly uniform across the sky, and has small temperature fluctuations, $|\delta T/T| \sim 10^{-5}$. This radiation is also polarized, with E and B-modes, although current observations show B consistent with zero [3] [15]. A temperature map is shown in Fig. 1.3. The information contained in the temperature and polarization maps can be described by a two-point correlation function. In Fourier space, the auto-correlation power spectrum for the temperature takes the form

$$C_l^{TT} = \frac{1}{2\pi^2}\int \frac{dk}{k}\Theta^2(k, z=0)\mathcal{P}_R(k), \tag{1.53}$$

   where $\Theta(k, z = 0)$ is the transfer function, while $\mathcal{P}_R(k) = A_s(k/k_0)^{(n_s-1)}$ is the primordial power spectrum. k_0 is the so-called pivot scale, and A_s, n_s are the amplitude of primordial fluctuations, and spectral index, respectively. An image of this power spectrum is presented in Fig. 1.4. A feature of the CMB power spectrum is that it contains a signature of oscillations that happened in the photon-baryon fluid in the primordial Universe, manifested as peaks in the spectrum. The position of these peaks, as well as their amplitudes, are directly related to the horizon scale of the Universe at the time of decoupling $z = z_\star \approx 1100$. This decoupling defines a surface[4], known as the last scattering surface, whose physical size is given by:

$$l_A = \frac{\pi}{\delta\theta} = \frac{\pi(1+z_*)d_A(z_*)}{r_s(z_*)}, \tag{1.54}$$

   the horizon scale is defined as

$$r_s(z_*) = \frac{1}{\sqrt{3}H_0}\int_{z_*}^{\infty}\frac{dz}{\sqrt{1+3\omega_b/4\omega_\gamma}E(z)}. \tag{1.55}$$

   Here, $E(z) = H(z)/H_0$ whereas ω_b, ω_γ are the physical density of baryons and

[3] This could change for future experiments with enhanced resolution.

[4] Since the decoupling was a gradual process, what we have in practice is not a single surface, but many. A more correct term would be layer.

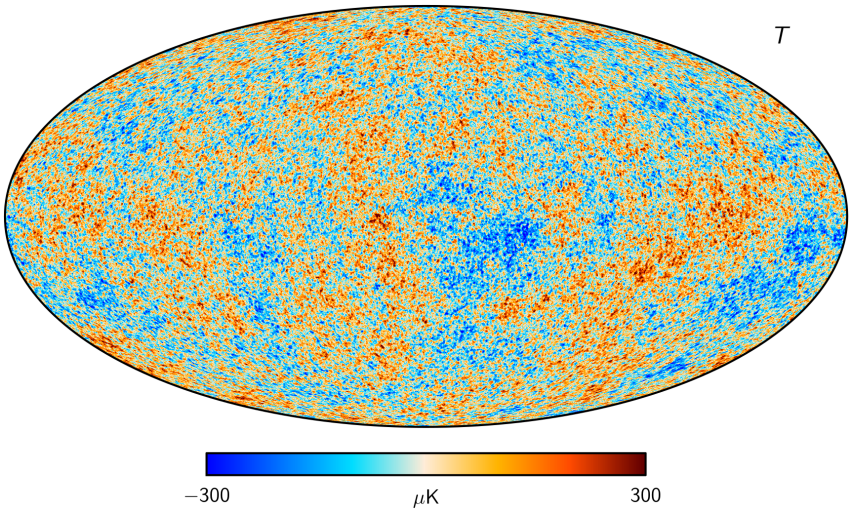

Figure 1.3: Temperature anisotropies map from Ref. [43]

photons, respectively. They relate to the density parameter by $\omega_i = \Omega_i h^2$ for the i-th species, where $h = H_0/(100\,\mathrm{km/s/Mpc})$ is the reduced Hubble constant.

As we can see from Eqs. 1.54 and 1.55, the position of the CMB peaks can be related to cosmological parameters such as ω_b, ω_γ. In the next section, we will present the constrains on CMB for some cosmological models, such as ΛCDM.

2. **BAO:** Oscillations in the photon-baryon plasma in the primordial Universe manifested as baryon density waves, the baryon acoustic oscillations (BAO). Soon after decoupling, the photon drag suffered by the baryons stops, at a time known as the drag epoch. As a consequence, the density waves stop propagating. The maximum distance covered by the BAO is defined by the sound horizon at drag epoch:

$$r_s = \int_{z_{drag}}^{\infty} \frac{c_s(z)dz}{H(z)}, \tag{1.56}$$

with c_s the sound speed. By assuming a Universe largely dominated by matter and radiation at early times, we find the following expression for the sound speed

$$c_s = \frac{1}{\sqrt{3\left[1 + \frac{3\Omega_{b,0}}{4\Omega_{\gamma,0}}\right]}}. \tag{1.57}$$

The acoustic scale defined by the comoving sound horizon at ~ 150 Mpc is present in the clustering of galaxies as an increase in probability for finding two galaxies separated at this scale (Fig. 1.5). Thus, the BAO can be used as a standard ruler to study the properties of the Universe. The BAO signal can be decomposed into

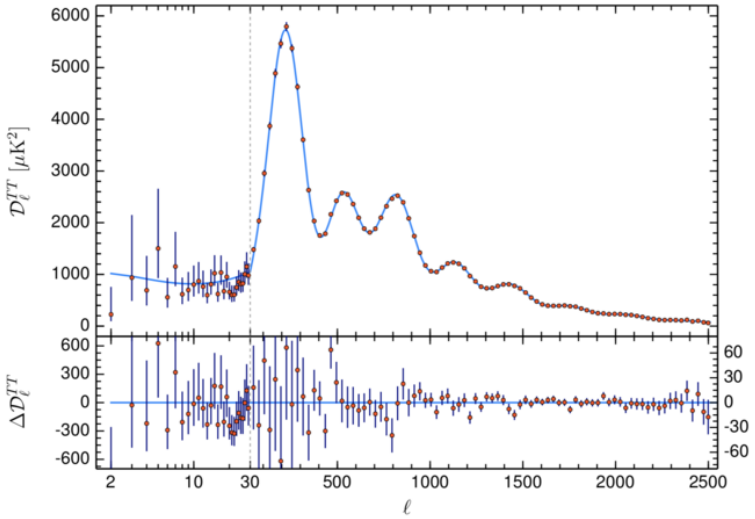

Figure 1.4: Angular power spectrum for the temperature anisotropies of the CMB. The data points are shown in red, and a theoretical curve prediction for ΛCDM is presented as a blue line. The spectrum is given in terms of $D_l^{TT} = l(l+1)/2\pi C_l^{TT}\bar{T}_0^2$, with $\bar{T}_0$ the average CMB temperature today. Figure adapted from Ref. [15].

radial ($\parallel$) and transversal ($\perp$) contributions relative to the line of sight:

$$r_\parallel = (1+z)d_A, \tag{1.58}$$

$$r_\perp = \frac{cz}{H(z)}, \tag{1.59}$$

where d_A is the angular diameter distance. Often times, the measured quantity used to determine the BAO scale is the averaged spherical distance D_V:

$$D_V = (r_\perp^2 r_\parallel)^{1/3} = \left[(1+z)^2 d_A^2(z)\frac{cz}{H(z)}\right]^{1/3}. \tag{1.60}$$

3. **SN Ia:** White dwarfs are stars associated to the final stages of stellar evolution. These objects are gravitationally governed by the degeneracy pressure of electrons, their mass limit is determined by the Chandrasekhar limit at $\sim 1.4\mathrm{M}_\odot$. If an astrophysical process, such as mass accretion by a companion star in the stellar system, happens to surpass the Chandrasekhar mass, the white dwarf enters gravitational collapse, resulting in a thermonuclear explosion known as Supernovae type Ia (SNIa). The physical energy liberated in this explosion can be calculated from nuclear processes. By accurately measuring the light curve of SNIa, it is possible to calibrate them through consecutive methods which form the cosmological ladder (See e.g. Ref. [45]). The quantity derived from observations is the distance modulus

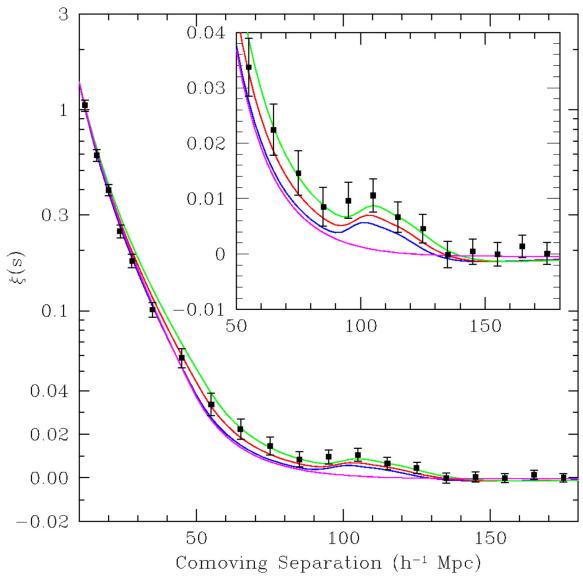

Figure 1.5: Large-scale correlation function in redshift-space for the SDSS LGR sample from Ref. [44]. The BAO peak is located around $100\mathrm{h}^{-1}$Mpc. The colored curves represent different cosmological models: $\Omega_m h^2 = 0.12$, $\Omega_m h^2 = 0.13$ and $\Omega_m h^2 = 0.14$ for green, red and blue, respectively. The magenta line is for a pure CDM model, with $\Omega_m h^2 = 0.105$, which predicts no BAO feature, as expected.

μ:

$$\mu = m - M = 5\log\left(\frac{d_L}{1\mathrm{Mpc}}\right) + 25. \tag{1.61}$$

Here, m is the apparent magnitude of the SNIa, while M corresponds to the absolute magnitude, that is, the magnitude of the object if it is at 10 pc from us. As mentioned in Sec. 1.1.2, d_L is the luminosity distance, which can be rewritten as:

$$d_L = (1+z)\int_0^z \frac{dz'}{H(z')}, \tag{1.62}$$

with

$$H(z) = H_0\sqrt{\Omega_{m,0}a^{-3} + \Omega_{r,0}a^{-4} + \Omega_{\Lambda,0}}.$$

for the flat ΛCDM. Therefore, observations from the SNIa will provide us direct measurements of $H(z)$, thus imposing constrains mainly on H_0, but also on the density parameters for a given cosmological model.

4. **Weak lensing:** Massive objects on the Universe act as a lens, bending the light rays of background sources and thus causing distortions to the original source image, an effect know as gravitational lensing. While bigger distortions are able to produce multiple images of the source, most of the time, these effect occurs in the form of weak gravitational lensing, where the direct effect cannot be determined by a single background source, but rather they are detected in the form of a statistical signal.

The main goal of studying weak lensing is to provide a mapping from the unlensed image in the source plane to the distorted image visualized in the sky, and from that, use it to provide information about cosmological parameters of our Universe. We can calculate the mapping of the image to the source in terms of the lensing potential. For the weak lensing regime, this mapping is singular: only one image is generated for each source.

From an observational point, we cannot directly measure the deflection angle, the difference from the source to the image. However, the mapping allows us to separate 3 different components, the magnification, and the shear components γ_+, $\gamma_\times$. Magnification is related to effects on the apparent size of the object, brightness and the number density of galaxies. The shear contributions can be attributed to E-modes for stretches parallel or perpendicular to the wave vector, and B-modes, which are stretches at 45° to the wave vector. It is possible to show that B-modes vanish (see Ref. [34] Ch. 13.5), leaving only E-modes to cosmic shear. Thus, under the small angle approximation, the lensing power spectrum is given by

$$C_{EE}(l) = l^4 \int_0^\chi [cot_K(\chi_1) - cot_K(\chi)]^2 \frac{P_\Phi(k = l/d_{A1})}{d_{A1}^2} d\chi_1, \tag{1.63}$$

where χ is the comoving distance. $\cot_K(\chi)$ is

$$\cot_K(\chi) \begin{cases} \chi^{-1}, & \text{if flat} \\ K^{1/2}\cot(K^{1/2}\chi), & \text{if closed} \\ |K|^{1/2}\coth(|K|^{1/2}\chi), & \text{if open.} \end{cases} \tag{1.64}$$

Here, $K = -\Omega_k(c/H_0)^{-2}$ is the physical curvature. We can rewrite $P_\Phi(k)$ in terms of the matter density fluctuations from Poisson's equation:

$$P_\Phi(k) = \left[\frac{3}{2}\Omega_m H_0^2(1+z)\right]^2 k^{-4} P_\delta(k). \tag{1.65}$$

Thus, Eq. 1.63 becomes

$$C_{EE}(l) = \int_0^\chi [W(\chi_1, \chi)]^2 \frac{P_\delta}{d_{A1}^2} d\chi_1. \tag{1.66}$$

$W(\chi_1, \chi)$ is the so-called window function:

$$W(\chi_1, \chi) = \frac{3}{2}\Omega_m H_0^2(1+z)\frac{\chi_1(\chi - \chi_1)}{\chi}\Theta(\chi - \chi_1), \tag{1.67}$$

with $\Theta(\chi - \chi_1)$ the step function.

The statistics of the weak lensing can be applied in many ways, such as galaxy-galaxy

lensing and power spectrum tomography. For a general idea of these methods, see Ref. [46]. Nevertheless, Eqs. 1.66 and 1.67 evidence the sensitivity of weak lensing to the matter density parameter, Ω_m. Furthermore, it can also be used to infer cosmological information about σ_8, the amplitude of the power spectrum at $8h^{-1}$Mpc, establishing weak lensing as an important probe to study the matter content of the Universe.

5. **Gas mass fraction:** The X-ray emission from the intracluster medium (ICM) in hot, massive, virialized galaxy clusters can be used as a tool to study their properties, such as their mass. In this context, a quantity of particular interest is the gas mass fraction of a cluster:

$$f_{gas} = \frac{M_{gas}}{M_{tot}}, \tag{1.68}$$

where M_{gas}, M_{tot} are the mass of the gas and the total mass of the cluster, respectively. One can assume that f_{gas} remains roughly constant in time to constrain cosmological parameters [47], which has proven to be a good approximation, as hydrodynamical simulations suggest that f_{gas} evolution is minimal and that it has low cluster-to-cluster scatter [48–52]. On the other hand, in order to properly estimate f_{gas}, X-ray mass measurements for the galaxy clusters are calibrated using weak lensing mass measurements [53, 54]. The gas mass fraction calculated in a spherical shell the center of the cluster is given by [55]:

$$f_{gas}^{ref}(z) = K(z)A(z)\Upsilon(z)\left(\frac{\Omega_{b,0}}{\Omega_{m,0}}\right)\left[\frac{d_A^{ref}(z)}{d_A(z)}\right]^{3/2}, \tag{1.69}$$

where the superscript "ref" stands for the fiducial cosmological model in the data analysis. $K(z)$ is the X-ray to weak lensing mass relation that is obtained from calibration:

$$K(z) = K_0(1 + K_1 z), \tag{1.70}$$

and $\Upsilon(z)$ accounts for the gas depletion of the cluster to the observer

$$\Upsilon(z) = \Upsilon_0(1 + \Upsilon_1 z). \tag{1.71}$$

Finally, $A(z)$ the angular correction relative to the cosmological model of reference

$$A(z) = \left(\frac{H(z)d_A(z)}{H^{ref}(z)d_A^{ref}(z)}\right)^{\eta}. \tag{1.72}$$

The $\Omega_{b,0}/\Omega_{m,0}$ ratio present in Eq. 1.69 for f_{gas} allows us to constrain $\Omega_{m,0}$ (or $\Omega_{c,0}$) given external information on $\Omega_{b,0}$ is provided. Furthermore, as f_{gas} data is sensitive to distances, it can also be used to constrain dark energy parameters such as the

EoS parameter w_x [55–57].

1.2.2 The ΛCDM model

Cosmological probes like the ones that described in the previous section help us study physical properties of the Universe. In most cases, however, there is a need to assume a referential cosmology model beforehand. This particular model, which is the cosmological concordance model, is the so-called ΛCDM. It assumes general relativity to be correct, and an FLRW metric. In this scenario, the Universe is presently dominated by a cosmological constant Λ ($w_x = -1$), which corresponds to about 70% of the energy distribution of the Universe, while the matter content is composed of $\approx 5\%$ of baryons and $\approx 25\%$ of dark matter. The remaining $\lesssim 1\%$ is in the form of radiation ($\Omega_{r,0} \sim 10^{-5}$), which as aforementioned is composed largely of photons and a small percentage of neutrinos.

From an observational perspective, the tightest constrains for Ω_Λ comes from CMB data, more specifically the Planck satellite, providing $\Omega_{\Lambda,0} = 0.6847 \pm 0.0073$ at 1σ [15] for the (flat) baseline-ΛCDM with the dataset TT,TE,EE+lowE+lensing, which uses the temperature and polarization auto- and cross-correlation, as well as lensing corrections. For SNIa, the latest result comes from Pantheon+& SH0ES sample [16, 21], with $\Omega_{\Lambda,0} = 0.666 \pm 0.018$ at 1σ confidence level (CL) for the flat ΛCDM.

On the other hand, the matter content of the Universe is mostly composed of dark matter, a type of matter that can so far only be detected through its gravitational effects. Evidence for the dark matter exists since the 70s for galaxy rotation curves [11], and can be supported today by different astrophysical objects and cosmological probes of distinct origin [15–20]. Although the nature of the dark matter remains an unsolved problem in cosmology and particle physics, some of its proposed candidates include weakly interactive massive particles (WIMPs), axions, primordial black holes and massive compact halo objects (MACHOs). We refer to [58, 59] for a review on dark matter and possible candidates. The dark matter in the Universe is largely in its non-relativistic form, the cold dark matter (CDM). In this context, constrains for the dark matter density parameter $\Omega_{c,0}$ (or $\omega_{c,0}h^2$) and $\Omega_{b,0}$ are given mainly by CMB measurements, SNIa samples, and redshift surveys. Just as in the case for dark energy, the best measurement is found by Planck data [15] for TT,TE,EE+lowE+lensing as $\omega_{c,0}h^2 = 0.1200 \pm 0.0012$ and $\omega_{b,0}h^2 = 0.02237 \pm 0.00015$ for the physical baryon density. The latter is also compatible with results from BBN at 2σ. Additionally, the Pantheon+ found $\Omega_{m,0} = 0.334 \pm 0.018$ at 1σ when in combination with SH0ES host Cepheid calibration [16]. Recently, the DESI survey reported $\Omega_{m,0} = 0.295 \pm 0.015$, the newest measurement of $\Omega_{m,0}$ up to date [60]. Similar results can also be found for other cosmological probes [17–20, 57], as well as in combination with other probes [61]. A figure of constraints for Ω_Λ and Ω_m for CMB, BAO and SNIa is presented in Fig. 1.6.

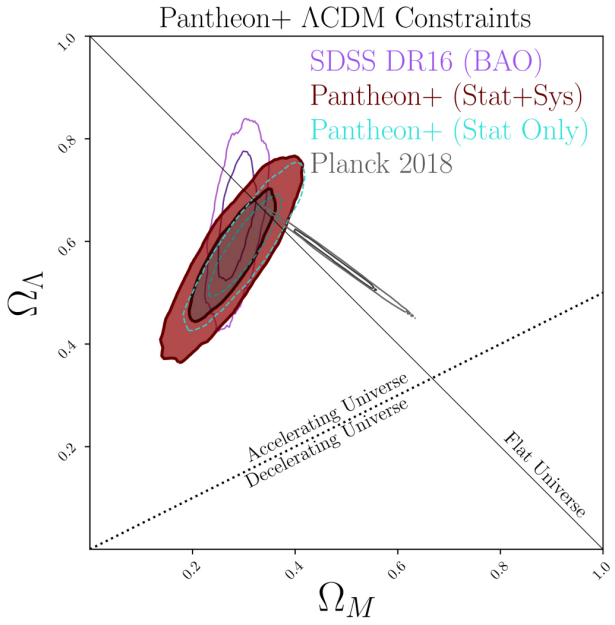

Figure 1.6: Constrains at 1σ and 2σ for Ω_Λ and Ω_m from SDSS DR16 (BAO), Planck DR3 (CMB) and the Pantheon+ sample (SNIa). Pantheon+ provides results for both statistic and systematic uncertainties. Vertical lines separate parameter regions for which the Universe is accelerating and/or flat. From Ref. [16]

Finally, results for ΛCDM with free curvature Ω_K lie mostly from CMB measurements and redshift surveys. The best constraint is $\Omega_K = -0.0000 \pm 0.0018$ at 68% confidence level from Planck data in combination with eBOSS and Pantheon data [15, 62], meaning a spatially flat Universe at 2% accuracy. While eBOSS data alone also agrees with an euclidean Universe at 1σ, Planck data alone shows preference for a closed Universe at 3σ, with $\Omega_K = -0.044^{+0.018}_{-0.015}$. KiDS-1000 finds Ω_K consistent with zero at 68% confidence level as well [63]. Nevertheless, a flat Universe is compatible with predictions from inflationary model.

1.2.3 Open problems in current cosmology

Although the tremendous success of the ΛCDM in explaining several aspects of the Universe in different scales is undeniable, it fails to answer certain questions, the most notorious being the so-called cosmological constant problem (CCP) [22]. As aforementioned, the most natural candidate to the cosmological constant Λ is the quantum energy density associated with the vacuum. While a theoretical value can be estimated through the quantum field theory (QFT) from the zero-point energy [64], an experimental value can also be obtained from cosmological observations such as [15]. The problem lies in the outstanding disagreement between those values:

$$\frac{\rho_{\Lambda,\mathrm{QFT}}}{\rho_{\Lambda,\mathrm{obs}}} \sim 10^{120}, \tag{1.73}$$

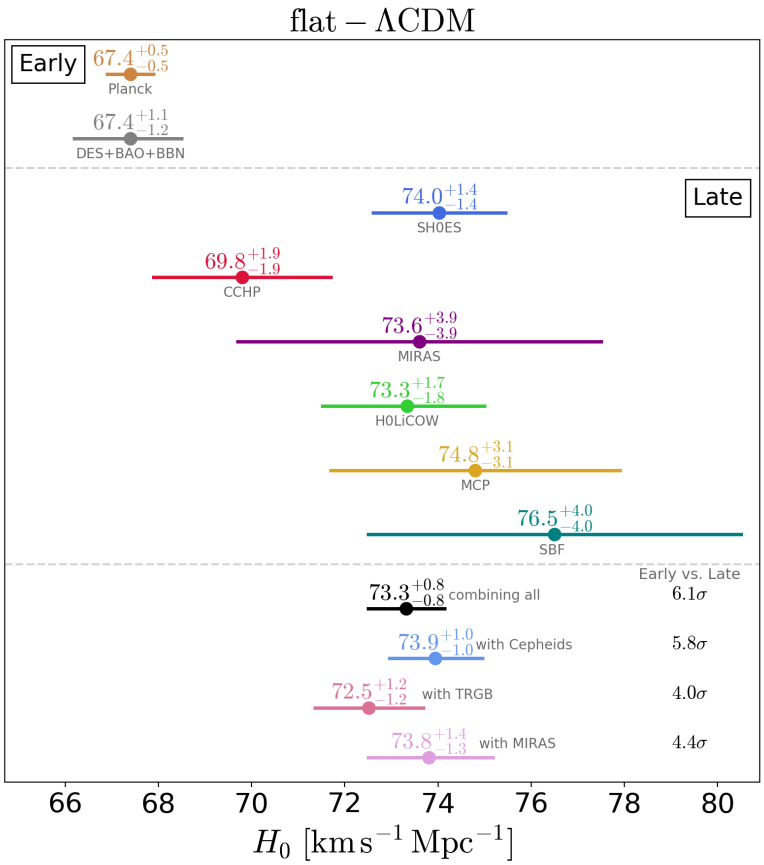

Figure 1.7: H_0 measurments from different cosmological probes, separated by early and late Universe. While early-type data preffers lower values ($H_0 \sim 67.4\,\mathrm{km/s/Mpc}$), late-type typically finds $H_0 > 70\,\mathrm{km/s/Mpc}$. Figure from Ref. [66]

where "obs" and "QFT" stand for the observed and the QFT values, respectively. This mismatch strongly suggests that there is a mistake in either the theoretical or experimental value, that the vacuum is not the cosmological constant, or rather, that the dark energy for our Universe must not be in the form of a cosmological constant after all. Another issue that arises with the ΛCDM is the cosmic coincidence [65]. It concerns the fact that matter and Λ energy densities are of the same order at the present time, while radiation and curvature are at least 2 orders of magnitude lower. In fact, at the Planck scale ($a \approx 10^{-32}$) their ratio is $\rho_\Lambda/\rho_m \approx 10^{-96}$. Although the coincidence problem can be interpreted as a consequence of the initial conditions of the Universe, it could also hint to a mechanism that establishes a relation between the two components.

Lastly, the remaining major issue with the standard cosmological scenario is the cosmological tensions. Despite the fact that cosmological probes largely agree with respect to the values of the density parameters, that is often not the case for the Hubble constant, H_0. In particular, Planck satellite reports $H_0 = 67.36 \pm 0.54\,\mathrm{km/s/Mpc}$ [15] at 1σ for the flat ΛCDM, while Pantheon+& SH0ES finds $H_0 = 73.6 \pm 1.1\,\mathrm{km/s/Mpc}$ [16] at 1σ as well, which translates to a $\approx 5\sigma$ tension. This trend repeats for other experiments of the early

versus late Universe, and does not vanish even for joint analysis, receives the name of Hubble tension. Efforts of solving the Hubble tension through systematic effects, along with a plethora of cosmological models have been made in the past years without much success (See Ref. [23] for an extensive review of this topic). A figure that illustrates different values for H_0 from the most relevant observational probes can be seen in Fig. 1.7.A similar effect, although less critical, happens for the σ_8 (or S_8), with tensions of about $2-3\sigma$ when compared to the latest CMB data [18–20, 63, 67–70].

1.3 Beyond ΛCDM

The issues discussed in the previous section demonstrate the urge for a new cosmological model. In general, one can approach modifications for cosmology through two routes: firstly modifying the gravitational theory, that is, assuming that the General Relativity theory must be extended. These are referred to as modified gravity theories (see e.g. [71] and references therein). The second path consists on formulating new theories for the dark components of the Universe, mainly to the dark energy component. In this thesis, we rely on the latter, focusing on dark energy theories to tackle the open problems in cosmology.

In this context, several different dark energy theories have been proposed in the literature. The most trivial way to modify dark energy is to simply leave $w_x = w_0$ as a free parameter, with w_0 a constant, but not necessarily -1. The constraints for this particular model are vast, and mostly place $w_0 \approx -1$, close to ΛCDM [16, 60, 61], although in some cases, such as CMB+BAO, is also possible to find a preference for phantom dark energy ($w_0 < -1$) [15, 57, 60]. Another important class of dark energy theory comes from considering dark energy to evolve with time, $w_x = w_x(a)$. Many parameterizations have been proposed in the literature, such as the Barboza-Alcaniz parameterization [72], but the most explored one is the Chevallier-Polaski-Linder (CPL) [73, 74]. For the CPL, the $w_x(a)$ is given by $w_x(a) = w_0 + w_a(1-a)$, with w_0, w_a constants, for which Pantheon+& SH0ES finds $w_0 = -0.93 \pm 0.15$ and $w_a = -0.1^{+0.9}_{-2.0}$ [16]. More DE models include treating the dark energy as a scalar field, such as quintessence models [75]. Early dark energy models have also been proposed as an attempt to solve the Hubble tension [76]. Finally, one can also consider the possibility of an interactive dark sector. The latter is part of the discussion of this thesis, and we'll dedicate the next chapter to motivating this hypothesis.

Chapter 2

Interactions in the dark sector

In the previous chapter, we presented the success of the standard cosmological model, ΛCDM, along with instances where it fails to explain certain aspects of the Universe. Among those problems, we mentioned the Coincidence Problem (CP), which concerns the ratio of (ordinary and dark) matter and dark energy. Although the severity of the CP is scale dependent (see e.g. [77]), the question remains: are we experiencing an unique moment of the Universe? Or is there an underlying reason for $r = \Omega_m/\Omega_\Lambda$ to be roughly one today? One could explore alternative cosmologies to solve, or at least alleviate the CP.

In this context, models that consider an additional, non-gravitational coupling in the dark sector, i.e., between dark matter and dark energy, could offer a natural explanation as to why the quantities of DE and DM are similar in the present. Nevertheless, interacting cosmologies can be investigated as an alternative to the ΛCDM, and in some cases it is possible to alleviate the H_0 and σ_8 tension. Along this chapter, we'll review a series of coupled dark sector scenarios, focusing on phenomenological models. We'll present the general equations, some direct physical consequences and how various datasets can favor or disfavor this class of model in comparison to the ΛCDM.

2.1 Phenomenological models: General equations

When dealing with the dark sector, we often assume DE and DM to be independent components for two main reasons: (i) for the sake of mathematical simplicity when solving our equations; and (ii) the unknown nature of these components refrain us from formulating a detailed interaction theory at a particle level without making a series of assumptions. Interestingly enough, the possibility of an interaction in the dark sector has been suggested around 40 years ago [78–80] in the context of an exotic cosmic component such as the cosmological constant coupled to the other constituents of the Universe. As of today, this hypothesis cannot be discarded *a priori* and can be endorsed by theoretical arguments such as the holographic principle [81]. In general, one can explore a coupling

between the dark components, i.e., dark matter plus dark energy, with radiation and/or baryonic matter in a so-called "fifth force" but not only this class of models offer more complexity, they are hard to deal with as they directly affect the growth of structure in a significant manner [82]. For this reason, we opted to limit the discussion of this thesis to models with energy and/or momentum exchange between dark matter and dark energy only. That is, the equations for radiation and baryons remain unaffected and their evolution can be described just as in Chapter 1, by the usual $\rho_r \propto a^{-4}$, $\rho_b \propto a^{-3}$ for the radiation and baryons, respectively. We note that this is a reasonable framework, given that interactions of the DE with baryons, if existent, are constrained by local gravity [83, 84]. Likewise, a dark energy coupled with radiation would imply that photons would not follow a geodesic path, something that is well established through various tests. Lastly, we resort to a phenomenological approach for a coupled dark sector, as to avoid a detailed interacting physical description of the model at a microscopic level.

On this basis, several forms of interaction are present in the literature and we refer the reader to [85–87] and references therein for a general review. Some mainly formulated for mathematical simplicity, e.g., $Q \propto H(\rho_c, \rho_x)$ [29, 88–92], while others are inspired by physical theories, such as vacuum decay [93, 94], or $Q \propto \Gamma(\rho_c, \rho_x)$ [95–97], resembling reheating models [98]. The assumed form of the dark energy, be it a fluid or scalar field [99], for example, will also lead to different classes of coupled models. In the case of a fluid, the choice the equation of state parameter $w(a)$, $w_x = -1$ [29, 100], a constant EoS [88] or time-dependent parameterizations [96, 97], is also be necessary in order to define the interacting kernel Q. Alternatively, from a particle physics standpoint, an interaction in the dark sector can be approached by quantum fields, including a standard scalar description, k-essence and tachyons (see [85] for details). Moreover, one can always expand the possibilities of an interacting model by adding curvature [101], considering neutrinos [102], anisotropic stress [103], a variable adiabatic sound speed for dark energy [104], considering non-linear dependence of (ρ_c, ρ_x) [105], elastic coupling of dark matter and dark energy [106]) and so on. Evidently, the possibilities of describing an interacting dark sector are numerous, and although we cannot easily discard this hypothesis, we can investigate its physical limitations. One important aspect is the stability of the solutions for the model in question: at background level, we must ensure a positive energy density for both dark constituents; at perturbative scales, the biggest problem arises from instabilities growing at linear level.

Moreover, we search for models that can alleviate of solve the coincidence problem. More often than not, this involves finding the so-called attractor solutions for the system, that is, solutions for which the system evolves for a various set of parameters. This approach ultimately avoids the fine-tunning associated to CP in non-interactive frameworks. In general, alleviating the coincidence problem can be achieved by two routes. The first one being that the model reaches a constant value of the DM/DE ratio, $r = \rho_c/\rho_x$ at late

times. Another possibility is that the model provides a ratio that varies slower than in the case for ΛCDM. In either case, the severity of the CP can be quantified through $r \propto a^{-\zeta}$, with $\zeta[0,3]$. The closer $\zeta \to 0$, the more successful the model is to solving the coincidence problem. In what follows, we will derive the equations for a general interacting kernel Q and discuss the general results before studying the particular cases in section 2.2.

2.1.1 Background dynamics

The first thing to change for interacting models are the conservation equations. Now, the dark components, i.e., dark matter and dark energy are no longer conserved individually, but are related to the source term, Q. In the covariant form, this becomes:

$$\nabla_\nu T_i^{\mu\nu} = Q_i^\mu, \tag{2.1}$$

with $i = c, x$ and

$$\sum_i Q_i^\mu = 0. \tag{2.2}$$

From Eq. 2.2, it follows that $Q_c^\mu = -Q_x^\mu$. In general, we can decompose Q_i^μ into parallel and perpendicular velocities components:

$$Q_i^\mu = Q_i u^\mu + F_i^\mu, \tag{2.3}$$

where u^μ the 4-velocity and F_i^μ the energy-momentum transfer, with $F_\mu u_\mu = 0$.

At background level, Eq. 2.1 for DM and DE become respectively:

$$\dot{\rho}_c + 3H\rho_c = Q, \tag{2.4}$$

$$\dot{\rho}_x + 3H(1 + w_x)\rho_x = -Q. \tag{2.5}$$

and $Q = Q_c = -Q_x$. We can notice that for $Q > 0$, CDM is gaining energy while dark energy has a net loss, which translates into dark energy creating dark matter. It follows that the opposite scenario, i.e., $Q < 0$, is equivalent to dark matter decay into dark energy. These statements can be summed up as the following

$$Q \begin{cases} > 0, & \text{dark energy} \to \text{dark matter}, \\ < 0, & \text{dark matter} \to \text{dark energy}. \end{cases} \tag{2.6}$$

We can compare the standard, non-interacting scenario to the interacting in terms of the effective equation of state, w_{eff} [86]:

$$w_{eff,x} = w_x + \frac{Q}{3H\rho_x} \tag{2.7}$$

$$w_{eff,c} = -\frac{Q}{3H\rho_c} \tag{2.8}$$

so that,

$$\dot{\rho}_i + 3H(1 + w_{eff,i})\rho_i = 0. \tag{2.9}$$

With $i = x, c$. Therefore, for $w_{eff,c} < w_c$, we have a dark matter that "dilutes" slower than a^{-3} and for $w_{eff,x} > w_x$, we have a dark energy that accelerates less than its non-interacting counterpart ($Q = 0$). Thus, for $Q > 0$, we'll have the following:

$$Q > 0 \begin{cases} w_{eff,c} < w_c = 0, & \text{DM dilutes slower than } a^{-3}, \\ w_{eff,x} > w_x, & \text{DE dilutes faster.} \end{cases} \tag{2.10}$$

Naturally, the roles are reversed if we change the sign of Q, which is ultimately changing the direction of the flux of energy for the interaction:

$$Q < 0 \begin{cases} w_{eff,c} < w_c = 0, & \text{DM dilutes faster than } a^{-3}, \\ w_{eff,x} > w_x, & \text{DE dilutes slower.} \end{cases} \tag{2.11}$$

From the above conditions, and also from Eqs. 2.15, 2.16, we can predict that Q must be small, if not vanishing. A large Q, i.e., $|Q| \gg 0$, implies a Universe that either never experienced the matter dominated period ($Q < 0$) or the dark energy dominated period ($Q > 0$). Alternatively, we should also expect a low value for Q, due to the great fit of ΛCDM to observational data, such as the ones introduced in the previous chapter.

Finally, it is useful to combine Eqs. 2.15 and 2.16 to form a differential equation for the DM/DE ratio $r = \rho_c/\rho_x$. Let's start by calculating $\dot{r}$:

$$\dot{r} = \frac{d}{dt}\left(\frac{\rho_c}{\rho_x}\right), \tag{2.12}$$

from the chain rule, we have

$$\dot{r} = \frac{\dot{\rho}_c}{\rho_x} - \frac{\rho_c}{\rho_x^2}\dot{\rho}_x, \tag{2.13}$$

and we put r into evidence on the right side

$$\dot{r} = r\left(\frac{\dot{\rho}_c}{\rho_c} - \frac{\dot{\rho}_x}{\rho_x}\right). \tag{2.14}$$

We can also write $\dot{r}$ in terms of Q by dividing 2.15 by ρ_c and 2.16 by ρ_x:

$$\frac{\dot{\rho}_c}{\rho_c} + 3H = \frac{Q}{\rho_c}, \tag{2.15}$$

$$\frac{\dot{\rho}_x}{\rho_x} + 3H(1 + w_x) = -\frac{Q}{\rho_x}, \tag{2.16}$$

and replacing in Eq. 2.14:

$$\dot{r} = -r\left[Q\left(\frac{\rho_c + \rho_x}{\rho_c \rho_x}\right) + 3Hw_x\right]. \tag{2.17}$$

Additionally, if we write $Q = 3HR(\rho_c, \rho_x)$, with $R(\rho_c, \rho_x)$ a function of the densities ρ_c, ρ_x, then we can write Eq. 2.14 in the compact form:

$$\dot{r} + 3Hr[f(r) + 1] = 0, \tag{2.18}$$

with

$$f(r) \equiv R(\rho_c, \rho_x)\left(\frac{\rho_c + \rho_x}{\rho_c \rho_x}\right). \tag{2.19}$$

Equations 2.14, 2.18 and the pair 2.15, 2.16 are similar when describing an interaction in the dark sector. That is, we are able specify a form on interaction by either choosing a Q, $R(\rho_c, \rho_x)$ or $f(r)$. This will be useful when discussing the dark degeneracy in the next chapter.

2.1.2 Perturbations and instabilities

Once we reach perturbative level for coupled dark energy models, we should construct our model with caution in order to avoid instabilities in the structure growth. As argued in [107], two points deserve special attention. The first one being the covariant form of the source function Q. When dealing exclusively with the background equations, one could assume a form of Q and start from Eqs. 2.15 and 2.16. However, we must ensure that the covariant form Q^μ reduces to Q at background level and that is consistent with an inhomogeneous Universe at small scales. In the event that this form is not well defined, instabilities may cause this model to become unrealistic, or worse, it's possible that a form of Q^μ for the *ansatz* Q is simply not possible. The other aspect we must be aware of is the velocity at which these inhomogeneities propagate, more specifically their adiabatic sound speed. The expression for the adiabatic sound speed of a component can be written in terms of its equation of state:

$$c^2_{a,i} = w_i + \frac{w_i'}{p_i'/\rho_i}, \tag{2.20}$$

which for a dark energy with constant EoS, w_0, it would necessarily mean an unphysical value for the sound speed, $c^2_{a,x} < 0$. Therefore, we require $c^2_{a,x} > 0$, usually $c^2_{a,x} = 1$, as in scalar fields [96, 108, 109]. Since this is directly related to the nature of an exotic component as the dark energy, this issue also arises in uncoupled models, but it

gains significance in coupled models, where non-adiabatic perturbations play a big role in instabilities. For a constant w_0, with $w_0 \neq -1$, these instabilities can be quantified by the doom factor, coined in Ref. [87]:

$$d \equiv \frac{Q}{3\mathcal{H}(1+w_0)\rho_x}. \tag{2.21}$$

If this term is positive, perturbations at large-scale will grow exponentially (see Fig. 2.8). As an example, consider $Q = 3\mathcal{H}\xi\rho_x$, with ξ a constant. In this case, the condition for $d < 0$, means that ξ and $(1 + w_0)$ must have opposite signs.

The perturbed (flat) FRLW conservation equations in the newtonian gauge for a general interacting case can be written as the following [30]:

$$\delta\rho_i' + 3\mathcal{H}(\delta\rho_i + \delta p_i) + (\rho_i + p_i)(3\Phi' + \theta_i) = aQ_i\Psi + a\delta Q_i, \tag{2.22}$$

$$[(\rho_i + p_i)\theta_i]' + (\rho_i + p_i)(4\mathcal{H}\theta_i - k^2\Psi) - k^2\delta p_i + (\rho_i + p_i)k^2\sigma_i = aQ_i\theta + ak^2\mathcal{F}, \tag{2.23}$$

where $\partial^i\mathcal{F} = aF^i$. Following [30], we consider the case $w_x = w_0 = -1$, assuming vanishing isotropic anisotropic stress and pressure perturbation for the dark matter component, that is, $\delta p_c = \sigma_c = 0$. Additionally, as the dark sector as a whole is conserved, $\delta Q = \delta Q_c = -\delta Q_x$, $\mathcal{F} = \mathcal{F}_c = -\mathcal{F}_x$. Taking the aforementioned considerations, the equations for θ_i, δ_i for $i = c, x$ are reduced to

$$\delta\rho_c' + 3\mathcal{H}\delta\rho_c + \rho_c(3\Phi' + \theta_c) = -aQ\Psi - a\delta Q, \tag{2.24}$$

$$\theta_c' + \mathcal{H}\theta_c - k^2\Psi = -\frac{a}{\rho_c}(Q\theta + k^2\mathcal{F}), \tag{2.25}$$

$$\delta\rho_x' + 3\mathcal{H}(\delta\rho_x + \delta p_x) = aQ\Psi + a\delta Q, \tag{2.26}$$

and

$$\theta_x' = 0. \tag{2.27}$$

2.2 Specific cases

Now that we've established the equations for a general interacting model, our next step is to define the form of the interaction term, Q. As mentioned in the previous section, various forms of the source term have been proposed along the years. Among them, two groups in particular are the most common, and will be discussed in this section. The first class of interacting phenomenological models is $Q = 3H[\xi_c\rho_c + \xi_x\rho_x]$, with ξ_c, ξ_x constants. The motivation behind this source term comes from assuming that the interaction must be a function of the density of the interacting fluid, and expanding it to the first order of a Taylor expansion. Furthermore, since we expect the interaction to be time-dependent,

a factor of H is often used in coupling models.

The second class of coupled models discussed here are interactions in the form $Q = 3(\Gamma_c\rho_c + \Gamma_x\rho_x)$, where Γ_c, Γ_x are the interaction rates. On contrast to the previous case, this form of interaction comes from particle physics, more specifically, some reheating models. Bellow, we'll review some particular cases that fit into these aforementioned categories.

2.2.1 $Q = 3H\xi\rho_c$

Let's consider an interaction between a dark energy with constant $w_x = w_0$ and pressureless dark matter for the interaction kernel $Q = 3H\xi\rho_c$. This model has been studied in [29, 86, 110–112]. In this case, the solutions for ρ_c, ρ_x can be easily calculated. The conservation equations become [86]:

$$\dot{\rho}_c + 3H\rho_c = 3H\xi\rho_c, \tag{2.28}$$

$$\dot{\rho}_x + 3H(1 + w_0)\rho_x = -3H\xi\rho_c. \tag{2.29}$$

The solution for the above set of equations leads to

$$\rho_c = \rho_{c,0}a^{-3(1+\xi)}, \tag{2.30}$$

$$\rho_x = \rho_{x,0}a^{-3(1+w_0)} + \frac{\xi}{(\xi + w_0)}\rho_{c,0}(a^{-3(1+w_0)} - a^{-3(1-\xi)}). \tag{2.31}$$

Notice how the solutions Eq. 2.30 and 2.31 reduce to $\rho_c = \rho_{c,0}a^{-3}$ and $\rho_x = \rho_{x,0}$ for $\xi = 0$ (equivalent of null interaction). Additionally, we have that $\xi \neq 1$, since Eq. 2.28 would imply ρ_c to be constant in time. While the solution for ρ_c is positive at all times for any value of ξ, that is not the case for ρ_x in equation 2.31. More specifically, we must require $\xi > 0$, as a negative energy density violates the weak energy condition (WEC). This can be verified through the asymptotic forms for ρ_x. Let's take the case of a cosmological constant, $w_0 = -1$ as an example. At late times ($a \approx 1$), $\rho_{x,0}$ is the dominant term, which again is expected as the solution must not deviate much from ΛCDM. On the other hand, at early times, i.e., $a \to 0$, the solution can be approximated to the following

$$\rho_x(a \to 0) = \rho_{x,0} + \frac{\xi a^{-3(1-\xi)}}{(1 - \xi)}. \tag{2.32}$$

From what we can see, for ρ_x to be always positive we must have $\xi/(1 - \xi)$ strictly positive, thus ξ cannot take negative values. In practice, this means that in the context of interaction of the form $Q = 3H\xi\rho_c$, the flow of energy necessarily manifests as dark energy forming dark matter. Furthermore, we also arrive to the conclusion that $0 < \xi < 1$. Figure 2.1 presents the DE/DM ratio for $\xi = 0.1$ in comparison to ΛCDM for this model.

The sign of the interaction parameter, γ is switched, because the conservation equations are written with the opposite sign in the paper [29]. A similar image is presented in the right panel of Fig. 2.6, but now for $w_0 = -1.1$, and $3\xi = 0.001, 0.01, 0.1$. In both cases ($w_0 = -1$ and -1.1), the progression of r in noticeably different than for ΛCDM, even for smaller values of ξ. In this sense, even if $r_0 = \rho_{c,0}/\rho_{x,0}$ is similar in both cosmological scenarios, i.e., $Q = 3H\xi\rho_c$ and the non-interacting case ΛCDM, and since the evolution rate of r is smaller for the coupled case, this softens the fine-tuning of the coincidence problem. In other words, the fact that $\Omega_{c,0}$ and $\Omega_{x,0}$ are similar now is not much of a coincidence as in the uncoupled case, where the variation of r is greater. This is sometimes called "soft coincidence" [111]. This simple case is effective to illustrate how the CP can be approached by interacting dark energy models.

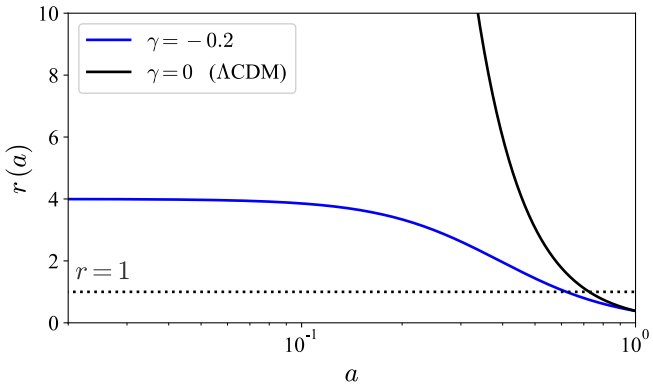

Figure 2.1: DE/DM ratio for $Q = 3H\xi\rho_c$, with $w_0 = -1$ for the dark energy. Our ξ is equivalent to $-\gamma$ in the figure. The curves indicate $\xi = \gamma = 0.1$ (blue) and the non-interactive case $\xi = \gamma = 0$ (black). Taken from Ref. [29].

2.2.2 $Q = 3H\xi\rho_x$

This model has been extensively studied in the literature [23, 29, 88, 90–92, 101, 112–115], and has some interesting features. As in the previous case, we'll consider a interacting dark energy with constant EoS w_0. The solutions for ρ_c and ρ_x become, respectively [86]:

$$\rho_c = \frac{-\xi}{(w_0+\xi)}\rho_{x,0}a^{-3(1+w_0+\xi)} + \left(\rho_{c,0} + \frac{\xi}{(w_0+\xi)}\rho_{x,0}\right)a^{-3}, \tag{2.33}$$

$$\rho_x = \rho_{x,0}a^{-3(1+w_0+\xi)}. \tag{2.34}$$

Once again, we must establish where an energy violation occurs for these solutions. In contrast with $Q = 3H\xi\rho_c$, now ρ_x is unproblematic, while ρ_c needs to be looked into. In

particular, ρ_c will be zero for [116]

$$a = \left[\frac{\xi\rho_{x,0}}{(\xi + w_0)C}\right]^{\frac{1}{3(\xi+w_0)}}, \tag{2.35}$$

with

$$C = 3H_0^2\left(\frac{\xi + w_0\Omega_{c,0}}{\xi + w_0}\right), \tag{2.36}$$

where we used $\rho_{x,0} + \rho_{c,0} = 3H_0^2$, $\Omega_{x,0} = \rho_{x,0}/3H_0^2$, $\Omega_{c,0} = 1 - \Omega_{x,0}$. At early times, $a \to 0$, the relevant term is C, therefore, in order for ρ_c to remain positive, we must have that $\xi + w_0\Omega_{c,0}$ is positive, so that

$$\xi > \|w_0\|\Omega_{c,0}. \tag{2.37}$$

On the other hand, at late times, the second term must remain positive in order to respect the WEC. This leads to

$$\frac{\xi\rho_{c,0}}{\xi + w_0} < 0, \tag{2.38}$$

which can only be satisfied for $\xi \geqslant 0$. This statement can be visualized in figure 2.2, which illustrates the curves for the WEC violation for past $(0 > a > 1)$ and future $a > 1$ for $w_0 = -0.8$ (quintessence) and $w_0 = -1.2$ (phantom). It is important to notice that the case $w_0 = -1$ lies in between the curves for $w_0 = -1.2$ and $w_0 = -0.8$, meaning a negative dark matter density is unavoidable in this model. As we can see, negative values of ξ imply in a future WEC violation, and $\xi > 0$ in WEC violation at early times. For the particular case of $w_0 = -1$, Fig. 2.3 showcases the background solutions, for which we can notice ρ_m, the total (pressureless) matter content becomes negative in the future at $a \sim 1.8$. This should be expected, since the dark matter largely dominated the matter content of the Universe. Alternatively, Fig. 2.4 displays the DM/DE ratio for this model for the cases $\xi = -\gamma = -0.2$ and $\xi = -\gamma = 0.2$ and as can be seen, negative values of ξ (positive values of γ) alleviate the coincidence problem in a similar fashion as it was discussed for $Q = 3H\xi\rho_c$.

2.2.3 $Q = 3H(\xi_c\rho_x + \xi_x\rho_c)$

Another form of linear dependence with the energy densities is $Q = 3H\xi(\rho_c + \rho_x)$, studied in [85, 97, 117]. This model constitutes a generalization of the two previous cases discussed. The differential equations for the background can be written as the following:

$$\dot{\rho}_x + 3H(1 + w_x + \xi_x)\rho_x = -3H\xi_c\rho_c, \tag{2.39}$$

$$\dot{\rho}_c + 3H(1 - \xi_c)\rho_c = 3H\xi_x\rho_x. \tag{2.40}$$

This case does not have simple analytical solutions (these can be found in [97]). Therefore, instead of directly discussing the dynamics and the complexity of the solutions for

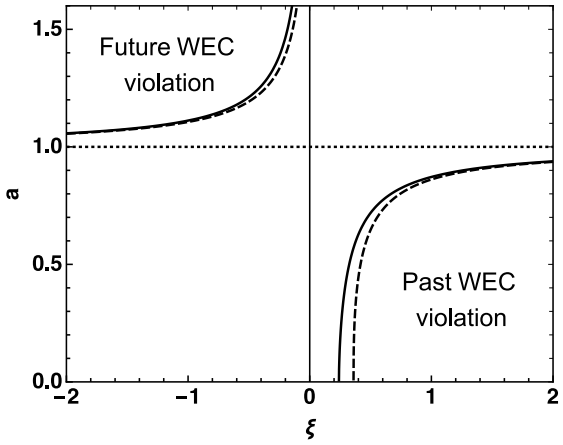

Figure 2.2: WEC violation curves for ρ_x in $Q = 3H\xi\rho_x$. The scale factor is presented in the y axis in terms of ξ, for two values of w_0: $w_0 = -0.8$ (solid line) and $w_0 = -1.2$ (dashed line). The value $\Omega_{x,0} = 0.7$ was used in order to make the plot. $\xi < 0$ leads to future $\rho_c < 0$ in the future, while $\xi > 0$ leads to $\rho_c < 0$ in the past. From Ref. [116].

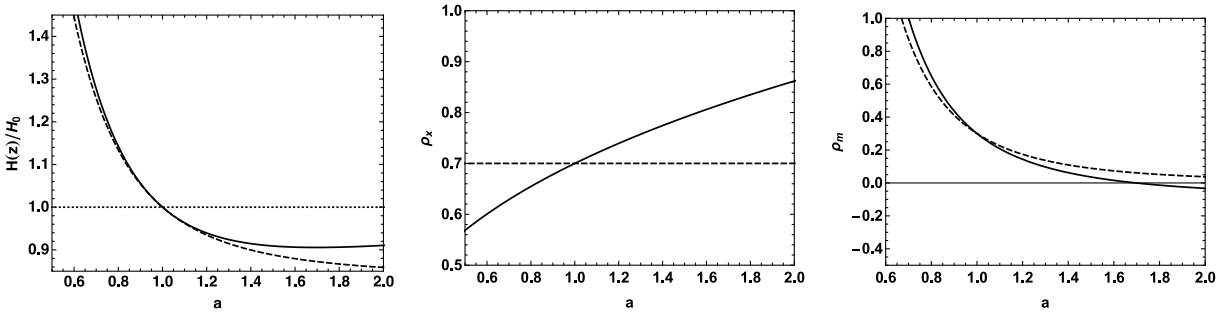

Figure 2.3: Background solutions for $Q = 3H\xi\rho_x$ in terms of the scale factor (solid lines) and for ΛCDM (dashed). The values chosen for the parameters were $w_0 = -1$, $\Omega_{0,x} = 0.7$ and $\xi = -0.1$. The figures show the Hubble parameter $H(z)/H_0$ (left), the dark energy density ρ_x (center) and the total matter content ρ_m (right). The dotted line in the left panel, and the solid line at $\rho_m = 0$ in the right panel are only for visual guidance. Taken from Ref. [116]

DM/DE ratio, we'll focus on highlighting some interesting constrains imposed on the parameters (ξ_c, ξ_x) by the weak energy condition. Following the discussion in [97], we define the following parameter:

$$\tilde{\alpha}_i = -\xi_i/w_0, \tag{2.41}$$

for $i = c, x$. Imposing that the dark matter and dark energy must be positive at all times, i.e., for the asymptotic solutions in the past and present leads to the conclusion that ξ_c and ξ_x must have the same sign, in the case if they are both non-zero. Furthermore, we have that

$$(\tilde{\alpha}_x - \tilde{\alpha}_c)^2 \leqslant 2(\tilde{\alpha}_x + \tilde{\alpha}_c) - 1. \tag{2.42}$$

Which determines that the acceptable values for $(\tilde{\alpha}_c, \tilde{\alpha}_x)$ must be below the parabola defined in Eq. 2.42, which can be visualized in Fig. 2.5. Applying further conditions, e.g., the fact that ρ_x is relevant only at later times, and ρ_c is less significant at late

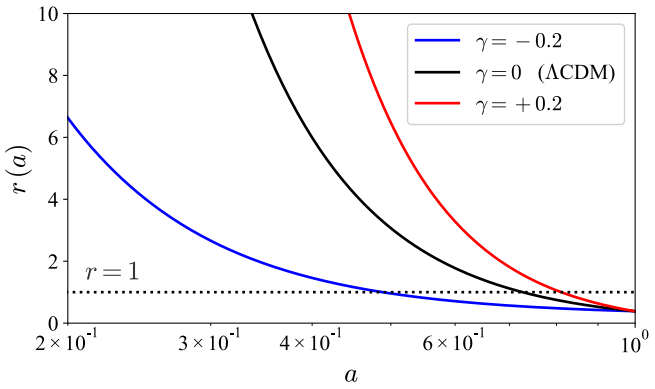

Figure 2.4: Evolution of the ratio r for $Q = 3H\xi\rho_x$ for different ξ. Here, γ is equivalent to $-\xi$. Thus, in blue we have $\xi = -0.2$, and $\xi = +0.2$ in red. The black line ($\xi = 0$) is the case for null interaction, ΛCDM. The curves indicate how a small variation can already change the evolution of r. As stated, this model softens the coincidence problem for $\xi = -0.2$. From Ref. [29]

times (displayed by the colored lines in the image), severely restricts the possibilities for parameter values to the region limited by the black lines.

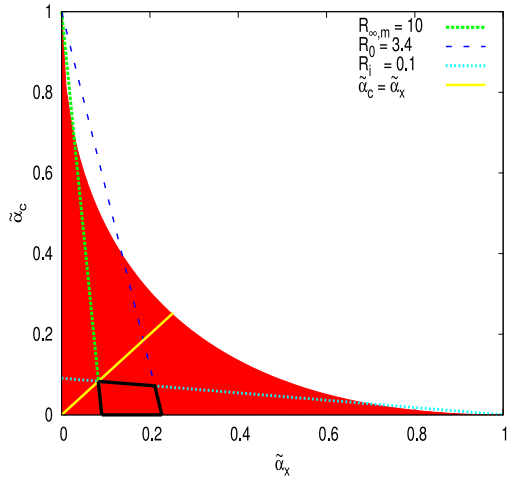

Figure 2.5: Allowed values of (ξ_c, ξ_x) for $Q = 3H(\xi_c\rho_c + \xi_x\rho_x)$ for the necessary conditions established in Ref. [97]. Here, $\tilde{\alpha}_i = -\xi_i/w_0$, with $i = c, x$, as per the original paper. R is the DM/DE ratio[1]. $R_i = 0.1$ (cyan), $R_0 = 3.4$ (blue) and $R_{\mathrm{inf},m} = 10$ (green) represent constrains for the dark energy to not be relevant at early times and dark matter to have little contribution at late times. See [97] for more details. The yellow curve indicates the case for $\tilde{\alpha}_c = \tilde{\alpha}_x$. The final region that obeys the aforementioned conditions is limited by the black lines of the parallelogram.

Likewise, the special case $\xi_c = \xi_x = \xi$ has also been investigated in the literature (see [85, 117, 118] and references therein). This particular scenario offers an attractor solution with constant DM/DE ratio [118], which could solve the coincidence problem if this ratio reaches in accordance to r_0 from observational data. As previously mentioned, this form of solutions for r constitute a road to solving the coincidence problem, since

they naturally offer a constant ratio at late times without having to rely on circumstantial arguments to explain why we observe $\Omega_c/\Omega_x \sim 1$ today. The evolution of the dark matter/dark energy ratio is presented on the left panel of Fig. 2.6 for the case $w_0 = -1.1$ for $3\xi = 0.0001, 0.01, 0.1$. As we can see, this model remarkably alleviates the CP, not only when compared to ΛCDM, but also in comparison to $Q = 3H\xi\rho_c$ (right panel), reaching lower values of ρ_c/ρ_x at earlier times, and driving r close to unity at late times. Nevertheless, Fig. 2.7 pictures the constituents of the Universe at background level for $w_0 = -1.1$ for $\xi = 0.1$ (left) and $\xi = 0.01$ (right). In the case that $\xi = 0.1$, we notice that the Universe undergoes a period of baryonic matter domination around $(1 + z) \sim 10^{-3}$ and $(1 + z) \sim 10^{-2}$. We consider this case to be unrealistic, as a baryon dominated epoch would directly affect the structure formation of our Universe, and although we expect some differences in the history and evolution of the Universe in a coupled scenario, the case for $\xi = 0.1$ would overall be inconsistent with current data, specially matter distribution probes like the ones mentioned in the previous chapter. In general terms, although this model could in theory provide a satisfactory answer for the coincidence problem, this would be the case for higher values of ξ, which ultimately poses an obstacle for this particular model.

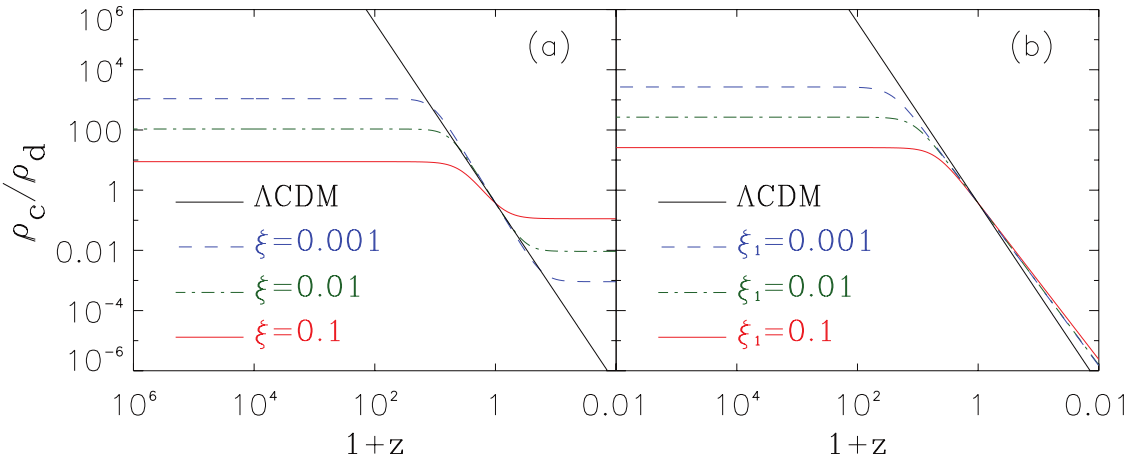

Figure 2.6: DM/DE evolution for the kernels $Q = H\xi(\rho_c + \rho_x)$ ($Q = 3H\xi(\rho_c + \rho_x)$) (a) and $Q = H\xi_1\rho_c$ ($Q = 3H\xi\rho_c$) (b), taken from [85]. In this work, rather than a cosmological constant interacting with CDM, we have that $w_0 = -1.1$. Notice that our ξ is actually 3 times smaller the one in this image, $3\xi \to \xi$ (and $3\xi \to \xi_1$ for figure (b)) for this reference, but qualitative results are the same. Once again we have ΛCDM in black, while $\xi = 0.001, 0.01, 0.1$ is represented in blue, green and red, respectively. In either situation, the ratio evolves differently than in ΛCDM, even for smaller values of ξ. In particular, for $Q = 3H\xi\rho_c$ ($Q = H\xi\rho_c$), the coincidence problem can be alleviated. In comparison, $Q = H\xi(\rho_c + \rho_x)$ ($Q = 3H\xi(\rho_c + \rho_x)$) the ratio varies less and even reaches values of r close to 1 naturally at late times for $\xi = 0.1$

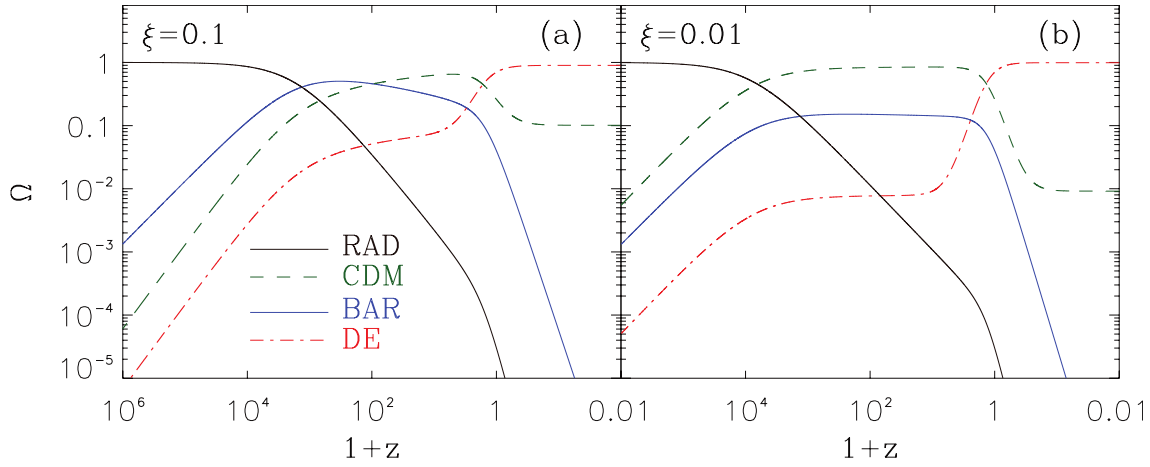

Figure 2.7: Energy density parameter for $Q = H\xi(\rho_c + \rho_x)$ (or $Q = 3H\xi(\rho_c + \rho_x)$), with $w_0 = -1.1$, for $\xi = 0.1$ (a) and $\xi = 0.01$ (b). Taken from Ref. [85]. As we can see, distinct values of the interaction parameter will change the history of the Universe, such as the time for equality between components. For $\xi = 0.1$, the Universe is dominated by baryons between $(1+z) \sim 10^{-3}$ and $(1+z) \sim 10^{-2}$, which is unrealistic according to current data.

2.2.4 $Q = 3(\Gamma_c\rho_c + \Gamma_x\rho_x)$

Lastly, let's explore another set of interaction kernels, in the form $Q = 3(\Gamma_c\rho_c + \Gamma_x\rho_x)$, where Γ_c, Γ_x are constant decay rates [85, 86, 95, 96]. This class of models is present in the physics of curvaton fields [119], dark matter decaying into radiation [120, 121] and also reheating models [98]. In practice, it could be seen as a generalization of the previous case, $Q \propto H(\xi_c\rho_c + \xi_x\rho_x)$, where instead of the Hubble rate, a global property of the Universe, we have a more generic form Γ, which could be a local decay rate. The conservation equations are no longer simplified as in the previous cases due to the dependency of H, and we have

$$\dot{\rho}_c + 3\rho_c(H - \Gamma_c) = 3\Gamma_x\rho_x, \tag{2.43}$$

$$\dot{\rho}_x + 3\rho_x(1 + w_0 + \Gamma_x) = -3\Gamma_c\rho_c, \tag{2.44}$$

with w_0 constant. The asymptotic solutions can be found in a simpler manner through auxiliary variables (see [97]). The DM/DE ratio at late times becomes:

$$r = -\frac{\Gamma_c}{\Gamma_x}. \tag{2.45}$$

Given that r must be positive as to obey the WEC, Eq. 2.45 requires Γ_c, Γ_x to have opposite signs: (i) $\Gamma_c \geqslant 0$ and $\Gamma_x \leqslant 0$ or (ii) $\Gamma_c \leqslant 0$ and $\Gamma_x \geqslant 0$. On the other hand, a careful analysis of the stability points in [97] states that it is not possible to find non-vanishing values for both Γ_i $(i = c, x)$ so that the energy densities remains positive at all times. Therefore, the case $\Gamma_c = \Gamma_x$ is automatically discarded. In the particular case

$Q = 3\Gamma_c\rho_c$, equivalent to $\Gamma_x = 0$, the solution for ρ_c is simply:

$$\rho_c = \rho_{c,0}a^{-3}\exp[3\Gamma_c(t - t_0)], \tag{2.46}$$

and is always positive regardless of Γ_c. Instabilities for ρ_x, however, appear on ρ_x at earlier times, such as the radiation dominated period [107][2], for which is valid:

$$3a\Gamma_c\frac{\rho_c}{\rho_x} = (3w_0 + 2)\tau^{-1}, \tag{2.47}$$

for $w_x < -2/3$. As the right side of Eq. 2.47 is positive, one finds that $\Gamma_c > 0$ in order to have $\rho_x > 0$. A positive value of Γ_c corresponds to dark energy forming dark matter. Furthermore, Eq. 2.46 with $\Gamma_c > 0$ translates to a fluid that becomes relevant with time, so a low interaction rate is expected in order for this model to be consistent with observational data. The top panel of figure 2.8 showcases two different cases for the evolution of ρ_x: first, for a fixed $\Gamma_c/H_0 = 5\text{e} - 7$ and varying w_0; for a fixed $w_0 = -0.87$, now varying Γ_c/H_0. In both cases it is evident that ρ_x is well behaved at background level. Nevertheless, large-scale curvature perturbation grow rapidly in the radiation dominated period, causing troublesome instabilities (bottom panel of Fig. 2.8). This behavior appears regardless of w_0, although it can be attenuated for higher values of w_0. As argued in [97], this occurs due to the limitation of assuming w_0 to be a constant.

Alternatively, if $Q = 3\Gamma_x\rho_x$, we have find the exact solution for ρ_x to be

$$\rho_x = \rho_{x,0}a^{-3(1+w_0)}\exp[-3\Gamma_x(t - t_0)]. \tag{2.48}$$

In this case, it is clear that ρ_x is positive for either $\Gamma_x > 0$ or $\Gamma_c < 0$. At later times, however, complications arise for a positive Γ_x, as it would lead to a Universe in which the dark energy becomes negligible in the future and dark matter would once again be the dominating energetic component. This hypothetical scenario violates thermodynamics.

Overall, this model can only be applied to certain eras of the Universe, depending on the specific choices of Γ_c and Γ_x.

2.3 Tests for IDE

From an observational perspective, various forms of phenomenological interactions have been investigated throughout the years, including the ones discussed in the previous section. In general, probes such as SNIa, BAO and CMB are crucial for accurately analyzing these models, as these types of dataset are able to extract significant information of dark energy, while providing the best constrains either alone or in a joint analysis. They

[2]Reference [107] defines opposite signs for Γ_c and Γ_x in their conservation equations.

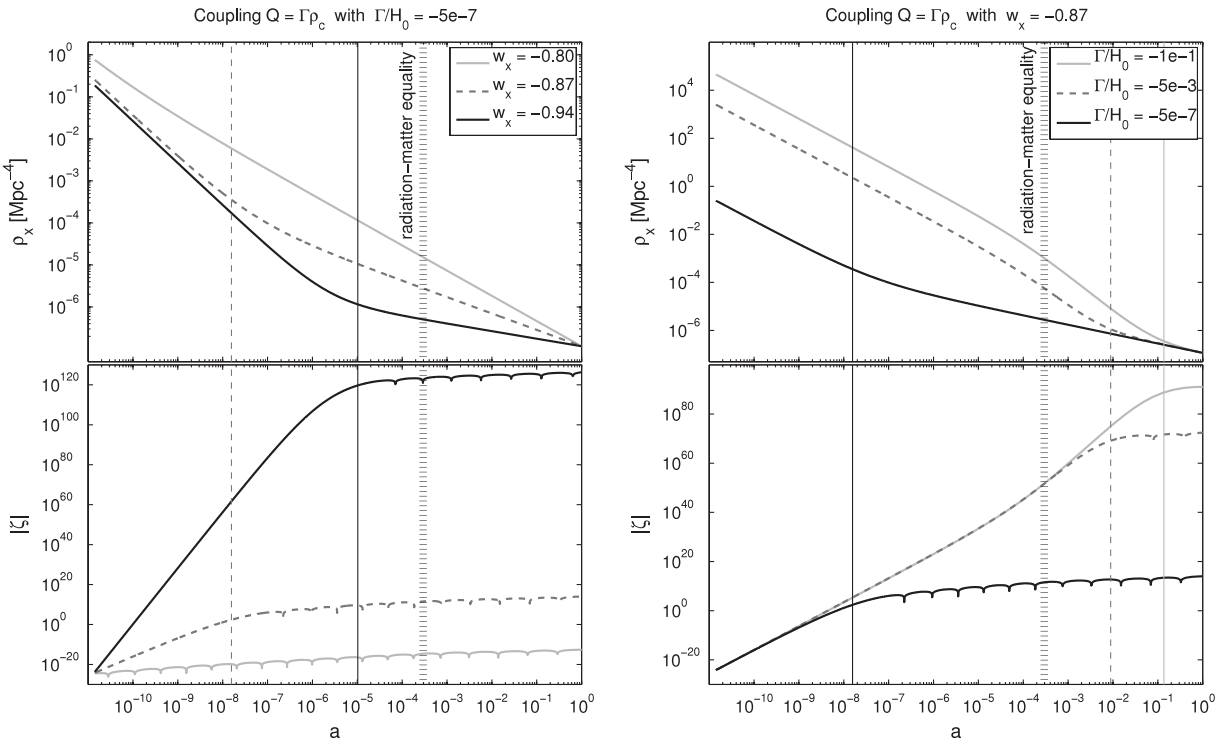

Figure 2.8: Evolution of ρ_x (top panels) and the gauge-invariant curvature perturbation ζ for $k = 7e-5$ Mpc(bottom panels) for the interaction kernel $Q = \Gamma_c\rho_c$ ($Q = 3\Gamma_c\rho_c$), taken from Ref. [107]. The left panel displays different curves for a fixed $\Gamma_c/H_0 = 5e-7$ (our Γ_c and the Γ on the paper have opposite signs) and different EoS: $w_0 = -0.80, -0.87$ and $w_0 = -0.94$. The right panel shows $w_0 = -0.87$ fixed, and $\Gamma_c/H_0 = 1e-1, 5e-3, 5e-7$. The radiation-matter equality is represented as a dashed vertical line. Vertical lines in black, dashed and in gray correspond to $|3\mathcal{H}(1+w_0)\rho_x| = |a\Gamma_c\rho_c|$ for each matching parameter. In the right panel, for $w_0 = -0.80$, this condition is met in the past and cannot be visualized in the image.

are also specially interesting if one also intends to explore the H_0 tension (or, in the case of other datasets, e.g., weak lensing for σ_8 tension).

In this context, the model $Q = 3H\xi\rho_x$ has gained a substantial amount of attention over the years [23, 29, 88–91, 112, 116, 122, 123]. In particular, Ref. [89] finds that $H_0 = 72.8^{+3.0}_{-1.5}$ km/s/Mpc at 1 C.L., and a non-vanishing interaction at about 3 C.L., for $\xi < 0$ and $w_0 = -0.999$ using PlanckTTTEEE+lowE [15] and H_0 from Riess (R19) [124]. The σ_8 tension is also reduced. This trend is maintained, though less significantly, even when including SNIa [125] and BAO measurements, or considering the lensing corrections for CMB. Similar qualitative results are found when considering a free w_0 in the quintessence limit ($w_0 > -1$), while in the case for a phantom dark energy, there is no preference for an interaction. Refs. [91, 122] also reports these results, with [122] taking into account Ω_k as a free parameter. More recently, results published by the DESI team corroborated these findings, with $H_0 = 70.0 \pm 0.59$ km/s/Mpc and $\xi = -0.191 \pm 0.068$ at 1 C.L. for a combined analysis using Planck (temperature, polarization and lensing)+ DESI BAO (galaxies, quasars and Lyα) + SNIa and cosmic chronometers data [90]. On the other

hand, as pointed out in Ref. [116], $\xi < 0$ is troublesome as it violates the weak energy condition in the future ($a > 1$). Furthermore, imposing a WEC prior on ξ qualitatively changes the results. No evidence favoring interaction is found when applying a WEC prior, i.e., requiring $\xi > 0$ for Planck+Pantheon in [116], this analysis gives $H_0 = 67.35^{+0.01}_{-0.02}$, recovering the usual value for ΛCDM.

Other works, including [29, 110, 112] place constrains on $Q = 3H\xi\rho_c$. Ref. [112] presents the results including perturbations in the Hubble rate. The constrains for PlanckTTTEEE+lensing in combination with various BAO measurements, the latest SNIa catalog Pantheon+, RSD and H_0 provide a vanishing interaction at 1 C.L., and found no substantial difference for H_0 when compared to ΛCDM. In [29], the model was discarded for BAO and CMB temperature data. Previous works, such as [110], reports the results for this kernel with a time-dependent equation of state, $w_x = w_0 + w_1 z$, indicating that this coupling favors smaller values of Ω_c. Additional kernels, including non-linear combinations of ρ_c, ρ_x, have also been analyzed, and we refer the reader to [29, 115]. Interacting models can be further extended to include the sum of neutrino masses, as in [102]. This work results suggest a non-vanishing coupling scenario for $Q = H\xi\rho_x$ above 3 C.L. when utilizing Planck+BAO+SNIa (JLA). More precisely, they find $\xi = -0.064^{+0.110}_{-0.083}$ for this dataset combination for an interacting vacuum and neutrinos, and $\xi = 0.087 \pm 0.068$ for an interacting vacuum and sterile neutrinos. Interacting models can also be studied in the context of primordial black holes as in [92]. H_0 and σ_8 tensions were evaluated as well, but no remarkable result was found.

Aside from parameter estimations, tests with observational data are present in the literature, such as non-parametric reconstructions [126], $Om(z)$ diagnostics [127], and statefinder parameters [128]. N-body simulations have examined these scenarios as well [129, 130]. Finally, while the current data is unable to provide strong evidence favoring or disfavoring most of the coupled models proposed, we should expect future experiments to provide powerful constrains on interacting models in the era of precision cosmology. In particular, Ref. [106] forecasts the constrains of scattering in the dark sector for Stage-IV experiments such as Euclid, while predictions in [126] indicate that next-generation LSS surveys such as Euclid and SKA will be able to discriminate interacting models with 4% uncertainty at $z \approx 1$.

Chapter 3

Dark degeneracy

3.1 A degeneracy in the dark sector

As previously stated, the set of equations that defines how gravity responds to the presence of the constituents of the Universe is the Einstein's field equations. When excluding the possibility of baryons and radiation interacting with dark matter and dark energy, i.e., the dark sector, one may rewrite Eq. 1.15 as

$$T^{d}_{\mu\nu} = \frac{G_{\mu\nu}}{\kappa} - \sum_{i=1}^{n} T^{i}_{\mu\nu}, \tag{3.1}$$

with $i = r, b$ for radiation and baryons, respectively. $T^{(d)}_{\mu\nu}$ is the total energy-momentum tensor for the dark sector:

$$T^{d}_{\mu\nu} = T^{c}_{\mu\nu} + T^{x}_{\mu\nu}, \tag{3.2}$$

with c the (cold) dark matter and x the dark energy constituents as usual. Their actual form, however, is undetermined by equation 3.2. In other words, since the composition of this constituent is arbitrary, there is an infinite number of possibilities that we could subdivide the dark sector. This fact poses the following problem: for a given $T^{d}_{\mu\nu}$, how can one infer the physical properties of the dark sector constituents, or rather, determine the cosmological model that accurately describes the Universe? In general, we can't. As a result, models that posses the same net contribution for the energy-momentum tensor of the dark sector, $T^{d}_{\mu\nu}$, will be degenerated, constituting the so-called *dark degeneracy* [24–29]. To illustrate our point, let's take a look at Eq. 1.21. In Chapter 1, we learned that the background evolution of the Universe is dependent on the total energy density ρ:

$$H^2(a) = \frac{8\pi G}{3}\rho. \tag{3.3}$$

The above equation is valid for the case of a flat FRLW metric, i.e., $\Omega_k = 0$. However, Ω_k is a cosmological quantity that can be directly probed via observations such as weak

lensing and BAO data [131, 132]. Thus, without loss of generality, we can center our discussion around a flat metric, simplifying our equations. Therefore, from Eq. 3.3, as long as the (total) resulting contribution of the energy density is the same, the expansion rate of the Universe, i.e., Hubble rate, will be the same. As an example, suppose we have two different splits of the dark sector:

$$\rho_d = \rho_c + \rho_x = \rho'_c + \rho'_x, \tag{3.4}$$

with $\rho_c \neq \rho'_c, \rho_x \neq \rho'_x$[1]. As we have assumed baryons and radiation to be $\rho_r \propto a^{-4}$, $\rho_b \propto a^{-3}$ regardless of the cosmological description, it is evident from Eq. 3.4, the Hubble rate will be the same for either (ρ_c, ρ_x) or (ρ'_c, ρ'_x):

$$\begin{aligned} H^2(a) &= \frac{8G\pi}{3}(\rho_r + \rho_b + \rho_c + \rho_x), \\ &= \frac{8G\pi}{3}(\rho_r + \rho_b + \rho'_c + \rho'_x). \end{aligned} \tag{3.5}$$

A direct consequence of this is in the distance measurements:

$$d_L(z) = \frac{1}{(1+z)^2}\int_0^{z'} \frac{dz}{H(z)}, \; d_A = \frac{d_L}{(1+z)^2}. \tag{3.6}$$

Clearly, this is applicable not only for the luminosity distances but to all distance measurements, including SNIa, BAO and cosmic chronometers. As a matter of fact, cosmological models with the same total value of energy momentum tensor for the dark sector will not be distinguished by any data that depends solely on $\propto H(z)$, which will be evident further in this chapter. This degeneracy is unavoidable at background level, but it can be overcome at perturbative scales, as we shall discuss in Sec. 3.2.2. If we consider a Universe containing only matter and dark energy, a valid approximation for low z, the dark degeneracy can also be expressed in the following way in terms of $w(z)$ [26]:

$$w(z) = \frac{H(z)^2 - \frac{2}{3}H(z)H'(z)(1+z)}{H_0^2\Omega_{m,0}(1+z)^3 - H(z)^2}, \tag{3.7}$$

which demonstrates how $w(z)$ cannot be determined unless we provide the value of $\Omega_{m,0}$ in advance. This can be visualized in Fig. 3.1. In general, the dark degeneracy doesn't have to be limited to the context of ΛCDM. As long as we specify a cosmological model, it is always possible to find a degenerated family of cosmologies with a different cosmological description. A degeneracy of similar fashion can be found in the context of modified gravity theories [133–136], although constraints from gravitational waves are capable of eliminating it [137].

As argued before, observations place $\Omega_{m,0} \simeq 0.3$ for ΛCDM, and we should expect

[1]Here, the prime simply denotes a different value of ρ, not a derivative in respect to the proper time.

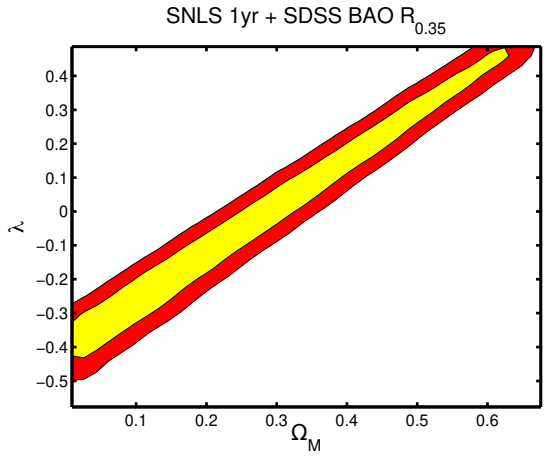

Figure 3.1: Dark degeneracy using background data from SNIa (SNLSS) [138] and BAO (SDSS BAO) measurements [44]. Taken from Ref. [26]. Here, the degeneracy is represented though $\Omega_{m,0}$ (Ω_M in the figure) and λ, where $w(z) = -1/(1-\lambda(1+z)^3)$. The filled areas in yellow and red indicate 1σ and 2σ confidence levels, respectively. Notice that this degeneration implies that unless we know $\Omega_{m,0}$ beforehand, we are unable to determine the value of λ. Consequently, a single form of $w(z)$ cannot be found as well.

to find small deviations from this result for other cosmological models, given the overall success of the standard cosmological scenario. Either way, a single value of $\Omega_{m,0}$ cannot be directly determined by astronomical observations alone, and with the era of precision cosmology, small differences between models become more relevant. For models degenerated though the dark degeneracy, although the background evolution is the same, parameters associated with the individual components of the dark sector differ: just as $\rho_c \neq \rho_c'$, $\rho_x \neq \rho_x'$, we'll find that $\Omega_{c,0} \neq \Omega_{c,0}'$, $\Omega_{x,0} \neq \Omega_{x,0}'$ (or equivalently $w(z) \neq w(z)'$ for the latter). Naturally, this is expected. Despite the fact that degenerated models could be said to "mirror" each other in some ways, their cosmological description is fundamentally distinct.

In this context, even if we find $(\Omega_{c,0}, \Omega_{x,0})$ for a given model, how could we identify that we are indeed observing this specific model, instead of the properties of its degenerated counterpart that manifest through the dark degeneracy? Likewise, assuming a form of $w(z)$ could also lead to incorrect interpretations of the cosmological model.

At its core, the dark degeneracy occurs due to our lack of knowledge of the dark sector of the Universe. It is an intrinsic consequence of the indirect measurements of the dark components, as observations provide constraints on dark matter plus dark energy based on gravitational interactions from the dark sector rather than the individual constituents. For that reason, the degeneracy is independent of the quality of our data. Even though we are able to conclude some of its properties through observational aspects, we cannot uniquely determine the physical nature of the individual constituents, thus allowing for a number of interpretations of the dark sector, such as the ones explored in Chapter 2.

It is important to emphasize that the existence of the dark degeneracy does not in-

validate studies on constraining cosmological models, such as performing parameter estimation, because testing the viability of several cosmological scenarios contributes on narrowing down the possibilities of the physical description of the dark sector as well. Nevertheless, investigating the dark degeneracy is relevant to improve our understanding of the components of the Universe.

The dark degeneracy can be explored in the following sense: (i) by understanding its impact on the information that can be extracted from cosmological data and (ii) studying possibilities of breaking the degeneracy, by either combining with background data that is not dependent on $H(z)$ or providing external information on the dark matter component of the Universe. Some of these aspects have been studied in the literature from different perspectives. In particular, [24] demonstrates through analytical and numerical calculations that a unique solution for the scalar field potential $V(\phi)$ from observations alone is unattainable. References [25, 139] construct a similar argument for $w(z)$ for scalar fields. On the other hand, [26–28] have also discussed few of its properties for a fluid description, while considering a vanishing sound speed for the total dark fluid [27], and discussing interacting models degenerated with ΛCDM [28]. More recently, [30] established a mapping from dynamical dark energy models degenerated with interacting vacuum cosmologies. This mapping allows us to directly investigate features of the dark degeneracy such as the ones mentioned above. Throughout this chapter we'll establish this degeneracy relations, and look into some particular cases that were studied in Ref. [30].

3.1.1 Unified dark fluid

Before we properly introduce the aforementioned mapping, it is useful to rewrite the dark sector in terms of the unified (dark) fluid. In this thesis, we have seen instances where the dark sector is constituted with independent fluids: dark matter and dark energy. In Chapter 2, we have also looked into the possibility of such components having energy and/or momentum exchange. Whichever the case, i.e., interacting or non-interacting scenarios, by assuming that interactions with baryons and radiation are nonexistent (or insignificant), one can always express the dark sector as a unified fluid, ρ_d:

$$\rho_d = \rho_c + \rho_x. \tag{3.8}$$

By considering the dark matter to be pressureless, that is, $p_c = 0$, we have that the pressure of the fluid will be equal to the pressure of the dark energy component

$$p_d = p_x, \tag{3.9}$$

and the equation of state of this dark fluid will be given by the usual definition

$$w_d = p_d/\rho_d, \tag{3.10}$$

which can be rewritten as

$$w_d = \frac{w_x}{(1 + r(a))}, \tag{3.11}$$

where $r(a) = \rho_c/\rho_x$ the DM/DE ratio, just as in the previous chapter. One advantage of the dark fluid description is that this fluid is conserved regardless of the existence of coupling between the components. The conservation equation for the fluid is the same as in Eq. 1.18:

$$\dot{\rho}_d + 3H(1 + w_d)\rho_d = 0. \tag{3.12}$$

The general solution for the energy density is

$$\rho_d(a) = \frac{3H_0^2}{8\pi G}\Omega_{d,0} \exp\left[-3 \int \frac{1 + w_d(a')}{a'} da' \right]. \tag{3.13}$$

And we can see it depends on the total dark sector $\Omega_{d,0} = \frac{\rho_d}{\rho_{crit}} = \frac{\rho_x}{\rho_{crit}} + \frac{\rho_c}{\rho_{crit}} = \Omega_{c,0} + \Omega_{x,0}$, rather than the separate contributions of its components.

3.2 Mapping degenerated models

We adopt the mapping derived from Ref. [29], which assigns dynamical dark energy models to interacting vacuum models. In each case, we consider the dark sector to be described by a perfect fluid, one that is independent of baryons and radiation, and assume dark matter as a pressureless constituent. Furthermore, for the dynamical approach, the DE equation of state is defined by a time-varying function, $w(a)$, whereas in the interacting approach the dark energy takes a vacuum EoS parameter, i.e., $w_0 = -1$, but it is coupled to the dark matter. In order to obtain a degenerated pair, we must specify the dynamical dark energy cosmology considered. The mapping will yield a (degenerated) interacting model whose form of Q (or $r(a)$,$f(r)$) is determined thought $w(a)$ of the dynamical approach. This mapping is also a bijective function, i.e., just as we are able to ascertain a coupled model from a time-varying dark energy, we can also determine a dynamical model starting from an interactive model (see Chapter 4). Although we will base the discussion of this thesis from this specific mapping, the general procedure to establish such relations remains valid: for two given dark sector descriptions, one must impose that the total energy-momentum tensor for the dark sector is equal on both cases. Then, by specifying a model for one of the approaches, we are able to find its degenerated correspondent.

From now on, we'll adopt the following notation for the quantities related to each

dark sector approach: quantities of the dynamic approach will be denoted with a bar overline ($-$), while quantities related to the interacting approach will be denoted with a tilde overline ($\sim$). In the event that these quantities are the same in both approaches and in the case for the quantities that belong exclusively to the interacting scenario, e.g., Q, no superscript is used.

3.2.1 Degeneracy at background level

Let's take a look at the background equations for each approach. For the dynamical approach, we have pressureless CDM and and dark energy with time-varying EoS:

$$\bar{w}_x = \bar{w}_x(a),\ \bar{w}_c = 0, \tag{3.14}$$

$$\Rightarrow \bar{p}_x = \bar{w}_x(a)\bar{\rho}_x,\ \bar{p}_c = 0. \tag{3.15}$$

Since each constituent is conserved individually, the conservation equations are the same as Eq. 1.18

$$\begin{cases} \dot{\bar{\rho}}_c + 3H\bar{\rho}_c = 0, \\ \dot{\bar{\rho}}_x + 3H(1+\bar{w}_x)\bar{\rho}_x = 0. \end{cases} \tag{3.16}$$

Here, H has no tilde or bar since it is equal regardless of the approach. The equations for the unified dark fluid provide the following relations

$$\bar{p}_d = \bar{w}_x(a)\bar{\rho}_x, \tag{3.17}$$

$$\bar{\rho}_d = \bar{\rho}_c + \bar{\rho}_x, \tag{3.18}$$

$$\bar{w}_d = \frac{\bar{w}_x(a)\bar{\rho}_x}{(\bar{\rho}_c + \bar{\rho}_x)}. \tag{3.19}$$

For the interacting approach, we consider scenarios where a cosmological constant interacts with pressureless CDM. Thus, for the interacting case, we have

$$\widetilde{w}_c = 0,\ \widetilde{w}_x = -1, \tag{3.20}$$

$$\Rightarrow \tilde{p}_c = 0,\ \tilde{p}_x = -\tilde{\rho}_x. \tag{3.21}$$

Likewise, the unified fluid equations become

$$\tilde{p}_d = -\tilde{\rho}_x, \tag{3.22}$$

$$\tilde{\rho}_d = \tilde{\rho}_c + \tilde{\rho}_x, \tag{3.23}$$

$$\widetilde{w}_d = -\frac{\tilde{\rho}_x}{\tilde{\rho}_c + \tilde{\rho}_x}, \tag{3.24}$$

and the conservation equations can be written as Eqs. 2.15, 2.16:

$$\begin{cases} \dot{\tilde{\rho}}_c + 3H\tilde{\rho}_c = Q, \\ \dot{\tilde{\rho}}_x = -Q. \end{cases} \tag{3.25}$$

Where Q is the interaction parameter, as described in Chapter 2, and is a function of the energy densities of dark matter and dark energy: $Q = 3HR(\tilde{\rho}_c, \tilde{\rho}_x)$(see 2.1.1). Since Q, R and $f(\tilde{r})$ are exclusive to the coupled approach, we omit the tilde notation for this quantities. It is assumed that there is no momentum transfer the between the components, only energy is exchanged. The direction of the energy flux is dark energy loosing energy to form dark matter for $Q > 0$ and vice-versa. By imposing the quantities that must be the same in both approaches, one is able to find a mapping from one approach to the other. At the background level, through our unified fluid description, this translates as the fluid being the same for the interacting and dynamical case, as pointed out in Eq. 3.4:

$$\bar{\rho}_d = \tilde{\rho}_d, \tag{3.26}$$

$$\bar{p}_d = \tilde{p}_d, \tag{3.27}$$

Combining equations 3.26 and 3.27, we also find that

$$\bar{w}_d = \tilde{w}_d. \tag{3.28}$$

From the above relations we obtain

$$\bar{w}_x(a)\bar{\rho}_x = \tilde{w}_x\tilde{\rho}_x, \tag{3.29}$$

$$\Rightarrow \bar{w}_x(a)\bar{\rho}_x = -\tilde{\rho}_x, \tag{3.30}$$

and

$$\bar{\rho}_c + \bar{\rho}_x = \tilde{\rho}_c + \tilde{\rho}_x. \tag{3.31}$$

Assume that for a given dark energy parameterization, we want to find the interacting correspondent degenerated model. In this case, we rewrite the equations in the following form

$$\tilde{\rho}_x = -\bar{w}_x\bar{\rho}_x, \tag{3.32}$$

$$\tilde{\rho}_c = \bar{\rho}_c + \bar{\rho}_x(1 + \bar{w}_x). \tag{3.33}$$

and for the density parameters

$$\tilde{\Omega}_{c,0} = \bar{\Omega}_{c,0} + \bar{\Omega}_{x,0}(1 + \bar{w}_x). \tag{3.34}$$

Now we have the cosmological parameters of the interacting model ($\sim$) in terms of the component of the dynamical approach ($-$). Thus, Eqs. 3.32 and 3.33 constitute the mapping of degenerated models for the background. Equivalently, the condition in Eq. 3.28 can also be expressed in terms of the DM/DE ratio, which will be convenient when discussing the behavior of the models in Section 3.3. The general solution for the DM/DE ratio of the dynamical approach:

$$\bar{r}(a) = \bar{r}_0 a^{-3} \exp\left[3\int \frac{1+\bar{w}_x(a')}{a'} da'\right]. \tag{3.35}$$

Using Eq. 3.11 and Eq. 3.28 the expression for $\tilde{r}(a)$ becomes

$$\tilde{r}(a) = \frac{\bar{w}_x(a)}{1+\bar{r}_0 a^{-3}\exp\left[3\int \frac{1+\bar{w}_x(a')}{a'} da'\right]} - 1. \tag{3.36}$$

We stress that Eq. 3.28 is valid not only for this case of interacting vacuum/dynamical DE but for any two approaches that can be viewed as a unified fluid. That is to say that we are free to choose $\tilde{w}_x(a)$ (or $\tilde{w}_d(a)$, for a broader case). For the interaction parameter Q, even though we need an *ansatz*, the exact function will only be determined through the mapping.

3.2.2 Degeneracy at perturbative linear level

As in the previous chapters, our discussion of the cosmological perturbations will be based on the linear regime for the first order. The degeneracy on perturbed scales follows the same procedure as the background: we impose that the total energy-momentum tensor for the dark sector is identical for the two approaches. We analyze the case for the cosmically relevant perturbations, i.e., scalar and tensor modes, separately.

- **Scalar perturbations**

  In the Newtonian gauge, for any dark sector approach, the Einstein field equations are described by Eqs. 1.37-1.40. Forcing the left side of this set of equations to be equal will result in the following relations:

$$-k^2\bar{\Phi} + 3\mathcal{H}(-\bar{\Phi}) = -k^2\tilde{\Phi} + 3\mathcal{H}(-\tilde{\Phi}), \tag{3.37}$$

$$k^2(-\bar{\Phi}' + \mathcal{H}(\bar{\Psi}) = k^2(-\tilde{\Phi}' + \mathcal{H}(\tilde{\Psi}), \tag{3.38}$$

$$\begin{aligned} &-3\bar{\Phi}'' + 3\mathcal{H}(\bar{\Psi}' - 2\bar{\Phi}') + 3\Big(2\frac{a''}{a} - \mathcal{H}^2\Big)\bar{\Psi} - k^2(\bar{\Phi}+\bar{\Psi}) \\ &= -3\tilde{\Phi}'' + 3\mathcal{H}(\tilde{\Psi}' - 2\tilde{\Phi}') + 3\Big(2\frac{a''}{a} - \mathcal{H}^2\Big)\tilde{\Psi} - k^2(\tilde{\Phi}+\tilde{\Psi}), \end{aligned} \tag{3.39}$$

$$-k^2(\bar{\Phi}+\bar{\Psi}) = -k^2(\tilde{\Phi}+\tilde{\Psi}). \tag{3.40}$$

Where on the left side we have the dynamical approach, and the right side constitutes the coupled approach. The conditions established by Eqs. 3.37-3.40 require the gauge-invariant potentials to be identical in both scenarios:

$$\bar{\Psi} = \tilde{\Psi}; \quad \bar{\Phi} = \tilde{\Phi}. \tag{3.41}$$

The degenerated mapping now connects $\left\{\delta\bar{\rho}_c, \delta\bar{\rho}_x, \delta\bar{p}_c, \delta\bar{p}_x, \bar{\theta}_c, \bar{\theta}_x, \bar{\sigma}_c, \bar{\sigma}_x\right\} \rightarrow \left\{\delta\tilde{\rho}_c, \delta\tilde{\rho}_x, \delta\tilde{p}_c, \delta\tilde{p}_x, \tilde{\theta}_c, \tilde{\theta}_x, \tilde{\sigma}_c, \tilde{\sigma}_x\right\}$. However, we assume CDM to be a pressureless component, which implies $\delta\bar{\rho}_c = \delta\tilde{\rho}_c = \bar{\sigma}_c = \tilde{\sigma}_c = 0$. On the other hand, from the right side of the Einstein's equations in the Newtonian gauge, we find the relations for the dark degeneracy for scalar perturbations as follow [30]:

$$\delta\bar{\rho}_c + \delta\bar{\rho}_x = \delta\tilde{\rho}_c + \delta\tilde{\rho}_x, \tag{3.42}$$

$$\bar{\rho}_c\bar{\theta}_c + \bar{\rho}_x(1+\bar{w}_x)\bar{\theta}_x = \tilde{\rho}_c\tilde{\theta}_c, \tag{3.43}$$

$$\delta\bar{\rho}_x = \delta\tilde{\rho}_x, \tag{3.44}$$

$$\bar{\rho}_x(1+\bar{w}_x)\bar{\sigma}_x = 0. \tag{3.45}$$

Where we have used $\tilde{w}_x = -1$. Notice how all the equations must be valid in order to obey Eq. 3.41. We'll discuss each of them individually. First, Eq. 3.42 reproduces the conservation equation for the interacting approach. This can be verified by combining Eq. 3.42 with the conservation equation from the dynamical approach (Eqs. 1.46, 1.47, 1.48 1.49), and using the relations from the background degeneracy. Furthermore, Equations 3.43 and 3.45 lack the velocity of the DE fluid, $\tilde{\theta}_x$, as well as the anisotropic stress $\tilde{\sigma}_x$ for the interactive model, which suggests that these quantities are not relevant for the degeneracy at scalar perturbations and can be set to zero. In fact, Eq. 3.45 only holds true for $\bar{\sigma}_x = 0$ at all times. Lastly, one can find that Eq. 3.44 is equivalent to the momentum conservation for the cold dark matter of the interactive model, by applying the same strategy used for Eq. 3.42. Overall, one can argue that the relations described in Eqs. 3.42-3.45 are, in a way, redundant. In fact, they do not contain new physics that would be interesting to investigate. Moreover, as mentioned, we must force $\bar{\omega}_x = 0$ in order for the degeneracy to be satisfied at all times. Bearing this in mind, we can choose to avoid the conditions established by the degeneracy at perturbative level with certain parameter choices. From now on, we'll opt to do this by fixing the sound speed for the DE frame to unity: $\bar{c}^2_{s,x} = \tilde{c}^2_{s,x} = 1$. This can be visualized rewriting the perturbed conservation

equations in terms of the comoving sound speed [30]:

$$\delta_i' + 3\mathcal{H}(c_{s,i}^2 - w_i)\delta_i + (1+w_i)(\theta_i + 3\Phi') + 3\mathcal{H}\Big[3\mathcal{H}(1+w_i)(c_{s,i}^2 - w_i) + w_i'\Big]\frac{\theta_i}{k^2} = \frac{aQ_i}{\rho_i}\Big[\Psi - \delta_i + 3\mathcal{H}(c_{s,i}^2 - w_i)\frac{\theta_i}{k^2} + \frac{\delta Q_i}{Q_i}\Big], \tag{3.46}$$

and

$$\theta_i' + \mathcal{H}(1 - 3c_{s,i}^2)\theta_i - \frac{c_{s,i}^2}{1+w_i}k^2\delta_i + k^2\sigma_i - k^2\Psi = \frac{aQ}{\rho_i(1+w_i)}\Big[\theta - (1+c_{s,i}^2)\theta_i - \frac{k^2\mathcal{F}_i}{Q_i}\Big]. \tag{3.47}$$

With

$$\delta_i \equiv \frac{\delta\rho_i}{\rho_i}, \tag{3.48}$$

$$c_{s,i}^2 \equiv \frac{\delta p_i^{(com)}}{\delta\rho_i^{(com)}}. \tag{3.49}$$

- **Tensor perturbations**

  We repeat the same process for the tensor perturbations (Eq. 1.50) and find that

  $$16\pi G a^2\bar{\Pi}_{ij} = 16\pi G a^2\tilde{\Pi}_{ij}, \tag{3.50}$$

  thus $\bar{\Pi}_{ij} = \tilde{\Pi}_{ij}$. However, since we are dealing with perfect fluids, the value of the anisotropic stress is already set to zero, which implies that the degeneracy for this type of perturbation leads to a trivial equation, i.e., there are no physical consequences for the degeneracy in this case.

3.3 Special cases of dark energy parameterization degenerated models

In this section we'll review the theoretical predictions and statistical analysis of the cases analyzed in Ref. [30], based on three $w(a)$ parameterizations mentioned for the dark energy: wCDM, Chavelier-Polarski-Linder (CPL) and Barboza-Alcaniz (BA). With the purpose of studying the differences between degenerated pairs at smaller scales, the DE comoving sound speed is set to unity on both scenarios ($\bar{c}_{s,x} = \tilde{c}_{s,x} = 1$), hence avoiding the degeneracy at perturbative level. In order to obtain the curves for the models, the software CLASS [39] was employed, where the cosmological quantities for the dynamical scenarios were fixed as follow:

$$H_0 = 70\,\mathrm{km/s/Mpc}, \quad \bar{w}_0 = -0.9, \quad \bar{w}_a = -0.1, \quad \bar{\Omega}_{c,0} = 0.25, \quad , \tag{3.51}$$

while $\tilde{\Omega}_{c,0} = 0.32$, as per Eq. 3.34. The baryon energy density was set to $\Omega_{b,0} = 0.05$, regardless of the approach.

3.3.1 wCDM

The first case to be considered is the simplest parameterization for the equation of state. This is an interesting model to further discuss few specifics of the dark degeneracy. For the wCDM, $\bar{w}_x(a) = \bar{w}_0$, where $\bar{w}_0$ is a constant with $\bar{w}_0 < -1/3$. The solutions for the energy densities of the dark sector in the dynamical approach, hereafter $\bar{w}$CDM, are (from Eq. 1.18):

$$\begin{cases} \bar{\rho}_c = \frac{3H_0^2}{8\pi G}\bar{\Omega}_{c,0}a^{-3}, \\ \bar{\rho}_x = \frac{3H_0^2}{8\pi G}\bar{\Omega}_{x,0}a^{-3(1+\bar{w}_0)}. \end{cases} \tag{3.52}$$

Thus, from Eqs. 3.32 and 3.33, the equivalent solutions for the interacting scenario, $\tilde{w}$CDM, become:

$$\tilde{\rho}_c = \frac{3H_0^2}{8\pi G}[\bar{\Omega}_{c,0} + \bar{\Omega}_{x,0}(1+\bar{w}_0)a^{-3\bar{w}_0}]a^3, \tag{3.53}$$

$$\tilde{\rho}_x = -\frac{3H_0^2}{8\pi G}\bar{\Omega}_{x,0}\bar{w}_0 a^{-3(1+\bar{w}_0)}. \tag{3.54}$$

We notice that $\tilde{\rho}_x$ will be positive, since $\bar{w}_0 < 0$. Now is an appropriate moment to highlight the distinction between $\bar{w}_0$ and $\tilde{w}_0$. On the right side side of Eq. 3.29, we have that $\tilde{w}_x\tilde{\rho}_x = \tilde{w}_0\tilde{\rho}_x = -\tilde{\rho}_x$ as per our choice for the interacting fluid. On the left side, for $\bar{w}$CDM, we have $\bar{w}_0\bar{\rho}_x$. Therefore, although $\tilde{w}_x$ is fixed to $\tilde{w}_0 = -1$, $\bar{w}_0 \neq \tilde{w}_0$, as long as $\bar{\rho}_x \neq \tilde{\rho}_x$. In point of fact, the only instance where $\bar{w}_0 = \tilde{w}_0$ is for $\bar{w}_0 = -1$, for which both interacting and dynamical models are reduced to ΛCDM (Eqs. 3.52 - 3.54). In other words, the $\bar{w}_0$ parameter can be associated to the interaction, in the sense that the more $\bar{w}_0$ deviates from -1, the stronger the coupling in the interactive scenario. As $\bar{w}_0$ is the only EoS related parameter to appear in both approaches, we'll chose to drop the bar notation for this quantity for the sake of simplicity, while keeping in mind that the closer w_0 is to -1, the similar the models are. The exact relation between the interaction and $\bar{w}_0$ is given by $f(\tilde{r})$:

$$f(\tilde{r}) = -1 - \frac{\bar{r}_0 w_0 a^{3w_0}}{1 + w_0 + \bar{r}_0 a^{3w_0}}. \tag{3.55}$$

With $\bar{r}(a)$:

$$\bar{r}(a) = \bar{r}_0 a^{3w_0}, \tag{3.56}$$

and $\tilde{r}(a)$:

$$\tilde{r}(a) = -1 - \frac{1 + \bar{r}_0 a^{3w_0}}{w_0}. \tag{3.57}$$

From Eq. 3.55, it is evident that $f(\tilde{r})$ will be zero for $w_0 = -1$, equivalent to a non-existing interaction. Furthermore, $f(\tilde{r})$ is associated to the interaction parameter Q through

Equation 2.19

$$f(\tilde{r}) = \frac{Q}{3H}\Big(\frac{\tilde{\rho}_c + \tilde{\rho}_x}{\tilde{\rho}_c\,\tilde{\rho}_x}\Big), \tag{3.58}$$

thus, if we assume that the interacting model obeys the weak energy condition, the term $\left(\frac{\tilde{\rho}_c+\tilde{\rho}_x}{\tilde{\rho}_c\,\tilde{\rho}_x}\right)$ will always be positive, and $f(\tilde{r})$ and Q will have the same signs (since $H > 0$ at all times). Moreover, we can rewrite $f(\tilde{r})$ from Eq. 3.55 as $f(\tilde{r}) = -(1 + X)$, with $X = -\frac{\bar{r}_0 w_0 a^{3w_0}}{1+w_0+\bar{r}_0 a^{3w_0}}$, so that for $(1+X) < 0$, $f(\tilde{r}) > 0$, $Q > 0$ and the flux of the interaction will be from DE→ DM, whereas if $(1 + X) > 0$, results in an energy flux from DM→DE.

Bellow, we present the background and perturbative quantities at linear regime for the ($\bar{w}$CDM, $\tilde{w}$CDM) pair. The left panel of Figure 3.2 illustrates the evolution of matter, radiation and dark energy for each model in terms of the cosmological redshift z. The panel on the top evidences that the evolution of Ω_i, with $i = c, x$ is identical for the degenerated models for $z \leqslant 10$, while the radiation component remains unaffected by the interaction considered, as anticipated. The difference between the approaches only gets significant at later times, reaching around 20% (bottom panel), when dark energy plays a bigger role in the evolution of the background, something already anticipated for the $\bar{w}$CDM model. The ratio $\bar{\Omega}_x/\tilde{\Omega}_x$ is simply $-1/w_0$, given the relation in Eq. 3.32. Since $\bar{w}_x$ is a constant, this ratio is stagnant as well. Nevertheless, if we were to extract the $\Omega_{i,0}$ from $H(z)$ data, we would not be able to correctly identify which model we are observing: if we assume we are observing $\bar{w}$CDM, the data will provide $\bar{\Omega}_{c,0} = 0.25$. Otherwise, if the cosmology of the Universe is accurately described by $\tilde{w}$CDM, then the correct value for the density parameter will be $\tilde{\Omega}_{c,0}$. The right side of Figure 3.2 presents the interaction function, $f(\tilde{r})$. A change in behavior for $f(\tilde{r})$ happens around $z \simeq 10$, where the second term in Eq. 3.55 becomes relevant. The line at $f(\tilde{r}) = 0$ corresponds to null interaction, for which the model reduces to ΛCDM, the same for $\bar{r}(z)/\tilde{r}(z) = 1$.

Even when the models are no longer bounded by the dark degeneracy, they are almost identical at the time for last scattering, $z \sim 1100$, therefore, we should expect these similarities to be reflected on the perturbative scales of the CMB power spectra as well. This can be visualized in Figure 3.3. More specifically, on the right panel, we can verify that the location of the peaks and the amplitude of the first peak coincide for the cosmological models in both temperature and polarization lensed power spectra. Differences between the models are displayed at $\bar{C}_\ell^{TT}/\tilde{C}_\ell^{TT}$, $\bar{C}_\ell^{EE}/\tilde{C}_\ell^{EE}$. At low ℓ, they arise due to integrated Sachs-Wolfe (ISW), however, since this region corresponds to great areas of the sky, the cosmic variance comes into play and therefore we do not expect CMB data constraints to give us information about the cosmological model. On the other side of the spectrum, the lensing effects gain more significance and may be able to differentiate the models, considering that the CMB power spectrum is measured with great precision for the high multipole range. Likewise, the differences for the gauge-invariant potentials Ψ and Φ at $k = 0.1\,\mathrm{h/Mpc}$ are manifested at late-times, in similar way to Fig. 3.2. We remind the

reader that by our construction for circumventing the degeneracy at linear level, Ψ and Φ are not equal. As for the lensing potential power spectrum is dependent on the cosmic history for each model, therefore, divergences between the approaches are foreseen, although they are minimal (subplot in the top right corner of Fig. 3.3).

Finally, the curves related to the matter at perturbative regime are displayed in Figure 3.4. On the right side, the density contrast for the baryons (dotted lines) behave equally for both models, since this constituent evolves independently whichever the scenario. The models departure for the CDM (solid lines) occurs at late-times, this once again can be attributed to the fact that the interaction is pronounced after the DE is the dominant component. On the right panel, the total matter power spectrum is presented for $z = 0$. The quantities fixed as Equation 3.51 lead to a $\bar{\sigma}_8 = 0.83$ and $\tilde{\sigma}_8 = 0.70$ for the $\bar{w}$CDM and $\tilde{w}$CDM, respectively. One can observe the qualitative similarities for $P(k)$ of both approaches. Considering that the sound speed for the DE component is fixed to $c^2_{s,x} = 1$ for $\bar{w}$CDM, $\tilde{w}$CDM, the DE is not able to cluster inside the horizon, and does not contributes with the matter power spectrum. Therefore, the difference in amplitude for $P(k)$ in Figure 3.4 originates from the difference in values for $\bar{\Omega}_{c,0}$, $\tilde{\Omega}_{c,0}$.

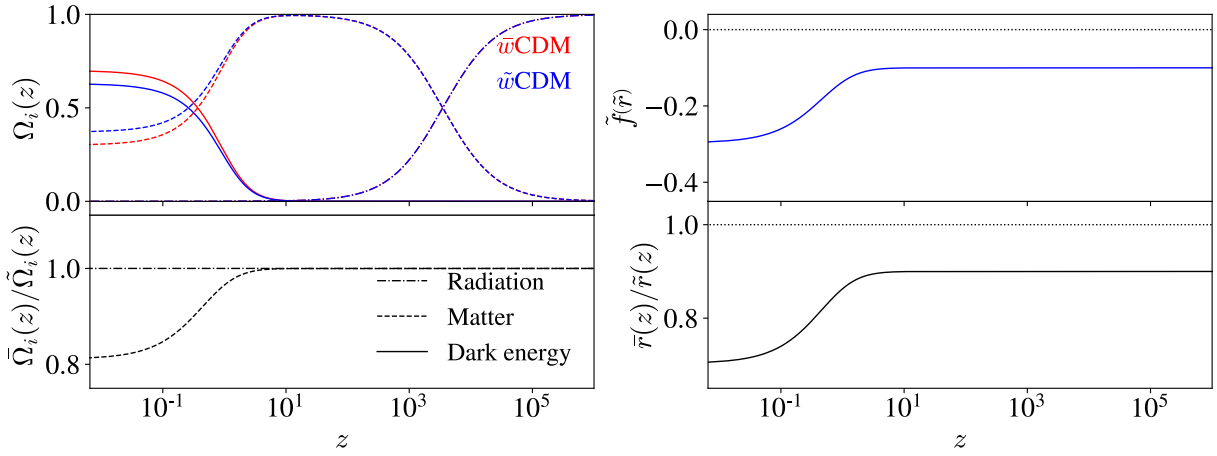

Figure 3.2: Background quantities for $\bar{w}$CDM (in red) and $\tilde{w}$CDM (in blue). The cosmological parameters were set following Eq. 3.51. **Top left:** Evolution of $\Omega_i(z)$, $i = r, c, x$ represented in dashed, point and dash, and solid lines, respectively. Differences between the approaches become apparent only around $z = 10$, where DE is the dominant energy component. Radiation follows its usual $\propto a^{-4}$, since it's not included in the interaction for the dark fluid. **Bottom left:** Ratio of the dynamical and interacting density parameters. **Top right:** Interaction function $f(\tilde{r})$ ($\tilde{f}(\tilde{r})$ in the figure), the function decreases as the second term in Eq. 3.55 gains significance. A dashed line at zero represents the case for null interaction. **Bottom right:** ratio between $\bar{r}(z)$, from the dynamical model and $\tilde{r}(z)$ from the $\tilde{w}$CDM. The dotted line at $\bar{r}(z)/\tilde{r}(z) = 1$ represents the case where this models coincide, ΛCDM.

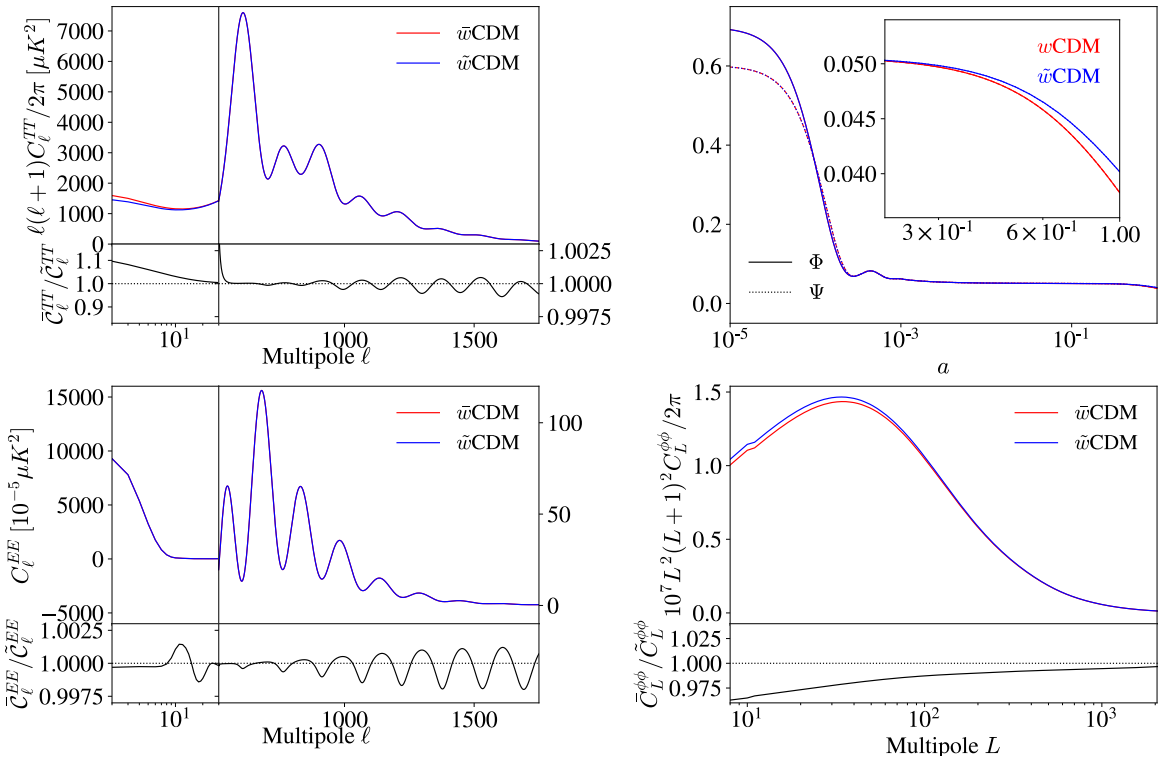

Figure 3.3: Quantities related to CMB power spectra for the $\bar{w}$CDM (in red) and $\tilde{w}$CDM (in blue). **Top left:** lensed CMB power spectrum for temperature auto-correlation. **Bottom left:** lensed CMB power spectrum for polarization auto-correlation. **Top right:** gauge-invariant potentials Φ,Ψ at $k = 0.1$h/Mpc. Since we chose to avoid the degeneracy for perturbative linear level, these potentials are not identical in both approaches. . **Bottom right:** lensing potential power spectrum.

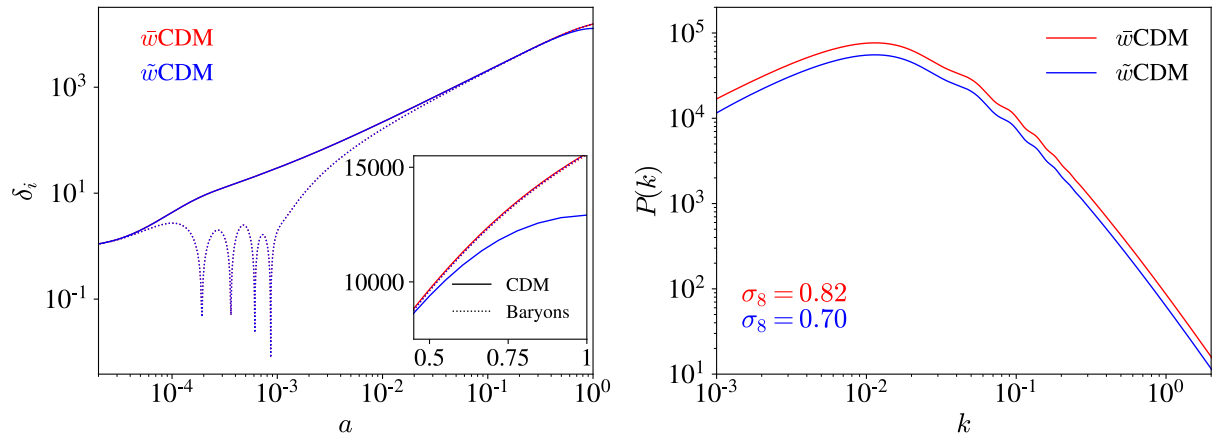

Figure 3.4: Behavior at perturbative scales for matter quantities in wCDM parameterization. Quantities for the dynamical model are represented in red ($\bar{w}$CDM), while the interacting model ($\tilde{w}$CDM) is in blue. The cosmological parameters were set following Eq. 3.51. **Left:** density contrast for baryons (dotted lines) and CDM (solid lines) for $k = 0.1\,$h/Mpc. **Right:** Total matter power spectrum for $z = 0$.

3.3.2 Chavelier-Polarski-Linder (CPL)

The second pair of degenerated models comes from the parameterization Chavelier-Polarski-Linder (CPL) [73, 74], briefly mentioned in Chapter 1. The CPL contains two parameters for the equation of state: w_0 and w_a, where the latter is associated to a time-dependent term:

$$w_x(a) = w_0 + w_a(1-a). \tag{3.59}$$

Therefore, as $a \to 1$, i.e., today, $w_x(a) \to w_0$. Following the same procedure for the first example of degenerated models, we find the relations for $\widetilde{\text{CPL}}$ from $\overline{\text{CPL}}$. The solutions for the dynamical approach become:

$$\begin{cases} \bar{\rho}_c = \frac{3H_0^2}{8\pi G}\bar{\Omega}_{c,0}a^{-3}, \\ \bar{\rho}_x = \frac{3H_0^2}{8\pi G}\bar{\Omega}_{x,0}a^{-3(1+w_0+w_a)}\exp[3w_a(a-1)]. \end{cases} \tag{3.60}$$

Which leads to the following equations for the interacting counterpart:

$$\tilde{\rho}_c = \frac{3H_0^2}{8\pi G}\Big\{\bar{\Omega}_{c,0} + \bar{\Omega}_{x,0}[1 + w_0 + w_a(1-a)]\exp[-3w_a(1-a)]a^{-3(w_0+w_a)}\Big\}a^{-3}, \tag{3.61}$$

$$\tilde{\rho}_x = -\frac{3H_0^2}{8\pi G}\bar{\Omega}_{x,0}[w_0 + w_a(1-a)]\exp[-3w_a(1-a)]a^{-3(1+w_0+w_a)}. \tag{3.62}$$

And the equation for the dark matter/dark energy ratio

$$\bar{r}(a) = \bar{r}_0\exp[3w_a(1-a)]a^{3(w_0+w_a)}, \tag{3.63}$$

$$\tilde{r}(a) = -\frac{1 + w_0 + w_a(1-a) + \bar{r}_0\exp[3w_a(1-a)]a^{3(w_0+w_a)}}{w_0 + w_a(1-a)}, \tag{3.64}$$

for the $\overline{\text{CPL}}$ and $\widetilde{\text{CPL}}$, respectively. $f(\tilde{r})$ becomes

$$\begin{aligned} f(\tilde{r}) = {} & \frac{3w_0(1+w_0) + w_a[3 + 6w_0 - 2a(1+3w_0)] + 3w_a^2(1-a)^2}{3[w_0 + w_a(1-a)\Big\{\bar{r}_0a^{3(w_0+w_a)} + [1 + w_0 + w_a(1-a)]\exp[-3w_a(1-a)]} \\ & \times \Big\{\bar{r}_0a^{3(w_0+w_a)} + \exp[-3w_a(1-a)]\Big\}. \end{aligned} \tag{3.65}$$

Now, the condition for which the coupled pair is identical to ΛCDM happens for $w_0 = -1$; $w_a = 0$. The relation that connects w_0, w_a to the interaction parameter is Eq. 3.65. Likewise, the closer $(w_0; w_a)$ is to $(-1; 0)$, the weakest the interaction for this model. The images for the same quantities as in Sec. 3.3.1 are presented bellow.

Figure 3.5 shows the background evolution for $\overline{\text{CPL}}$ and $\widetilde{\text{CPL}}$. In contrast to the former case, now $\bar{\Omega}_x/\tilde{\Omega}_x$ evolves with time, which can be visualized in the bottom panel on the left. On the top right, the evolution for $f(\tilde{r})$ starts off almost identical to ΛCDM,

and rapidly reaches around -0.4 at $z \leqslant 10$. Equivalently, the ratio $\bar{r}(z)/\tilde{r}(z)$ begins near unity, where the models are equal to $(w_0 = -1;\, w_a = 0)$ but decreases to bellow 0.8, reaching the fixed values established in Equation 3.51. Furthermore, we can observe from Eq. 3.65 that $f(\tilde{r})$ can have a sign change for certain combinations of $(w_0;\, w_a)$, implying that this coupled model, $\widetilde{\text{CPL}}$, allows for a switch in energy flux, an aspect that was absent in $\tilde{w}$CDM. Figs. 3.6 and 3.7 exhibit the differences for CMB and quantities related to the matter power spectrum, where $\bar{\sigma}_8 = 0.83$ for $\overline{\text{CPL}}$ and $\tilde{\sigma}_8 = 0.70$ for $\widetilde{\text{CPL}}$. We arrive to similar conclusions to the ($\bar{w}$CDM, $\tilde{w}$CDM) pair, except the fact that the models are in close proximity of $w_0 = -1$ at the time of the last scattering, the differences in the CMB are even more imperceptible as opposed to the previous example.

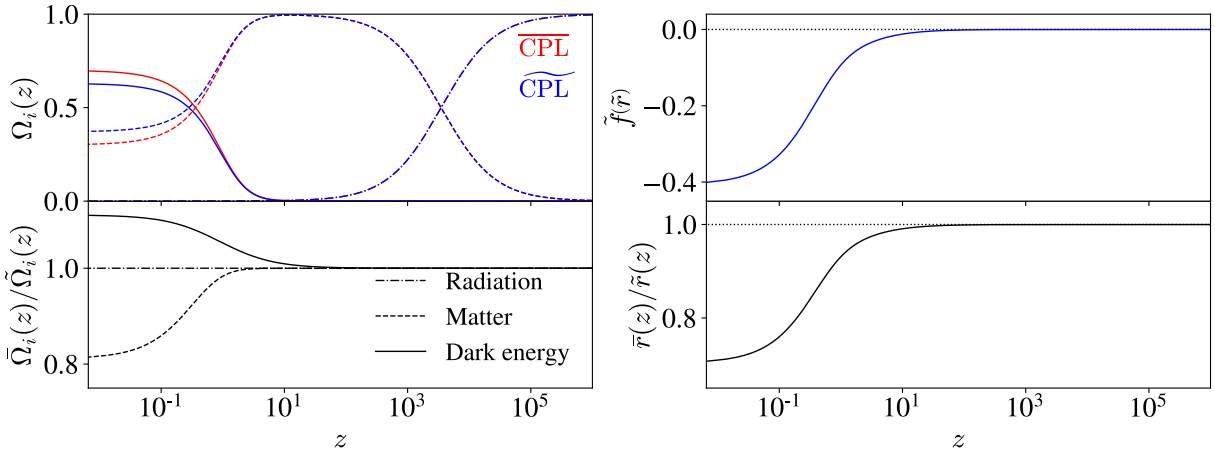

Figure 3.5: Background quantities for $\overline{\text{CPL}}$ (in red) and $\widetilde{\text{CPL}}$ (in blue). The cosmological parameters were set following Eq. 3.51. **Top left:** Evolution of $\Omega_i(z)$, $i = r, c, x$ represented in dashed, point and dash, and solid lines, respectively. Differences between the approaches become apparent only around $z = 10$, where DE is the dominant energy component. Radiation follows its usual $\propto a^{-4}$, since it's not included in the interaction for the dark fluid. **Bottom left:** Ratio of the dynamical and interacting density parameters. **Top right:** Interaction function $f(\tilde{r})$ ($\tilde{f}(\tilde{r})$ in the figure), the function decreases as DE gains significance. A dashed line at zero represents the case for null interaction. **Bottom right:** ratio between $\bar{r}(z)$, from the dynamical model and $\tilde{r}(z)$ from the $\widetilde{\text{CPL}}$. The dotted line at $\bar{r}(z)/\tilde{r}(z) = 1$ represents the case where this models coincide, ΛCDM.

3.3.3 Barboza-Alcaniz (BA)

The last dark energy parameterization we'll be discussing is the Barboza-Alcaniz. This parameterization was first proposed in Ref. [72], as a dynamical dark energy that avoids divergence at $a \to \infty$. For this case, the equation of state evolves as the following:

$$w_x(a) = w_0 + w_a \frac{(1-a)}{1 + 2a(a-1)}. \tag{3.66}$$

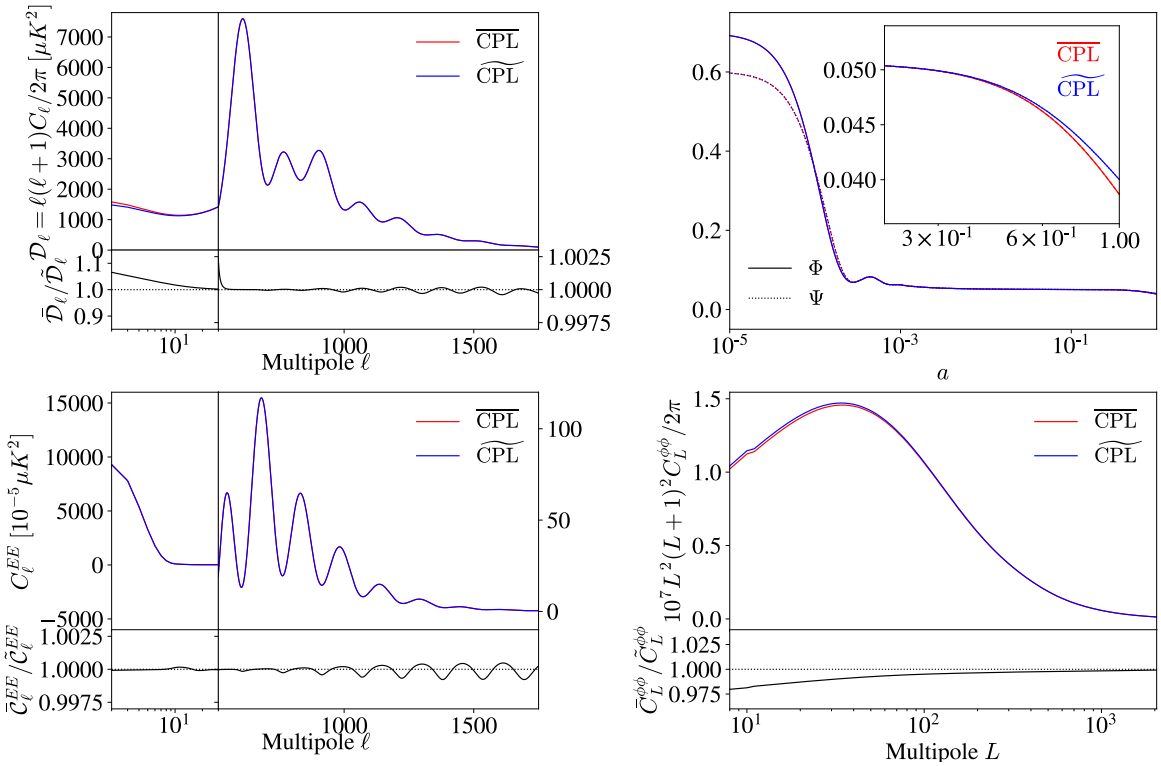

Figure 3.6: Quantities related to CMB power spectra for the $\overline{\text{CPL}}$ (in red) and $\widetilde{\text{CPL}}$ (in blue). **Top left:** lensed CMB power spectrum for temperature auto-correlation. **Bottom left:** lensed CMB power spectrum for polarization auto-correlation. **Top right:** gauge-invariant potentials Φ,Ψ at $k = 0.1\text{h/Mpc}$. Since we chose to avoid the degeneracy for perturbative linear level, these potentials are not identical in both approaches. . **Bottom right:** lensing potential power spectrum.

Hence, the dynamical solutions for Barboza-Alcaniz are given by:

$$\begin{cases} \bar{\rho}_c = \frac{3H_0^2}{8\pi G}\bar{\Omega}_{c,0}a^{-3}, \\ \bar{\rho}_x = \frac{3H_0^2}{8\pi G}\bar{\Omega}_{x,0}a^{-3(1+w_0)}\left[1+\left(\frac{1-a}{a}\right)^2\right]^{3w_a/2}, \end{cases} \tag{3.67}$$

while the relations for the interacting approach for the BA parameterization take a more complex form in comparison with the previous examples:

$$\tilde{\rho}_c = \frac{3H_0^2}{8\pi G}\left\{\bar{\Omega}_{c,0}+\bar{\Omega}_{x,0}a^{-3w_0}\left[1+w_0+w_a\frac{(1-a)}{1+2a(a-1)}\right]\left[1+\left(\frac{1-a}{a}\right)^2\right]^{3w_a/2}\right\}a^{-3}, \tag{3.68}$$

$$\tilde{\rho}_x = -\frac{3H_0^2}{8\pi G}\bar{\Omega}_{x,0}a^{-3(1+w_0)}\left[w_0+w_a\frac{(1-2a)}{1+2a(a-1)}\right]\left[1+\left(\frac{1-a}{a}\right)^2\right]^{3w_a/2}. \tag{3.69}$$

$$\bar{r}(a) = \bar{r}_0 a^{3w_0}\left[1+\left(\frac{1-a}{a}\right)^2\right]^{-3w_a/2}, \tag{3.70}$$

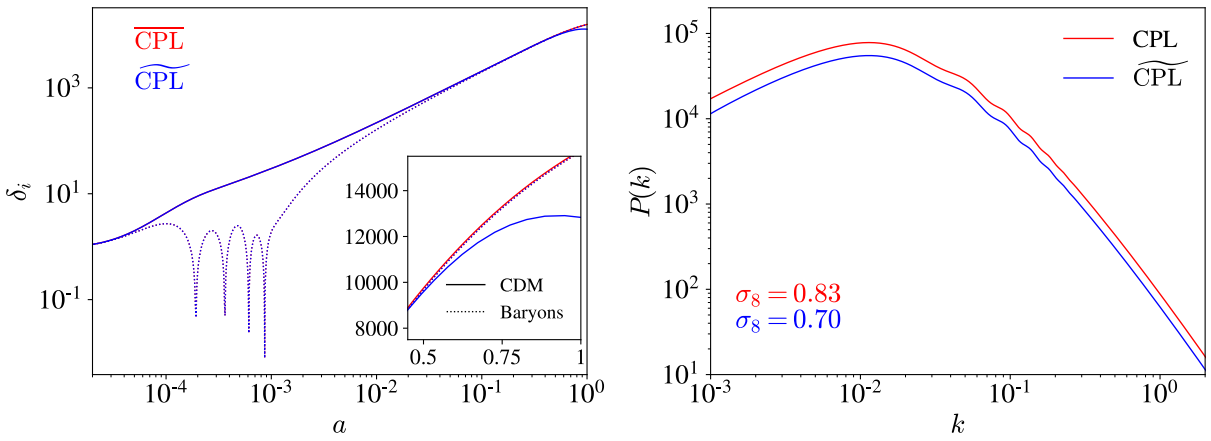

Figure 3.7: Behavior at perturbative scales for matter quantities in CPL parameterization. Quantities for the dynamical model are represented in red ($\overline{\text{CPL}}$), while the interacting model ($\widetilde{\text{CPL}}$) is in blue. The cosmological parameters were set following Eq. 3.51. **Left:** density contrast for baryons (dotted lines) and CDM (solid lines) for $k = 0.1\,\text{h/Mpc}$. **Right:** Total matter power spectrum for $z = 0$.

$$\tilde{r}(a) = -\frac{1 + w_0 + w_a\frac{(1-a)}{1+2a(a-1)} + \bar{r}_0 a^{3w_0}\left[1 + \left(\frac{1-a}{a}\right)^2\right]^{-3w_a/2}}{w_0 + w_a\frac{(1-a)}{1+2a(a-1)}}. \tag{3.71}$$

Finally, the interaction function for the $\widetilde{\text{BA}}$ is:

$$\begin{aligned} f(\tilde{r}) = &-1 + \Big\{w_a[1+2a(a-2)]\left(2 - \frac{2}{a} + \frac{1}{a^2}\right)^{3w_a/2} a^{1-3w_0} + \bar{r}_0\Big[-3\Big(w_0 + 2w_0a(a-1)\Big)^2 \\ &- 6w_0w_a + w_a a\Big(1 + 18w_0 + 2a(a-2)(1+6w_0)\Big) - 3w_a^2(a-1)^2\Big]\Big\} \\ &\Big\{3[w_0 + 2w_0a(a-1) + w_a(1-a)]\Big[\Big(1 + 2a(a-1)\Big)\bar{r}_0 \\ &+ \Big(1 + w_0 + 2a(a-1)(1+w_0) + w_a(1-a)\Big)\left(2 - \frac{2}{a} + \frac{1}{a^2}\right)^{3w_a/2} a^{-3w_0}\Big]\Big\}^{-1}. \end{aligned} \tag{3.72}$$

We present the plots of cosmological interest for these models bellow. We notice that for this occasion, $f(\tilde{r})$ undergoes a change in signal for the chosen values of ($w_0 = -0.9$; $w_a = -0.1$). This is pictured in Figure 3.8. More specifically, we observe $f(\tilde{r}) \simeq 0$, i.e., near ΛCDM, for the early Universe. At $z \leqslant 10$, $f(\tilde{r}) \geqslant 0$, but decreases to negative values not long after. The ratio $\bar{\Omega}_x/\tilde{\Omega}_x$ now evolves more abruptly, which can be visualized in the bottom left panel. This implies that there is a period where $\tilde{\Omega}_x > \bar{\Omega}_x$, but $\tilde{\Omega}_x$ later reaches lower values than $\bar{\Omega}_x$.

The quantities associated to the CMB follow an analogous behavior as the ones for wCDM and CPL (Fig. 3.9). In particular, for the BA pair, we notice that the lensing potencial power spectrum (bottom right) is essentially indistinguishable between the two

scenarios. Therefore, we do not expect CMB related data to contribute with significant information in differentiating these models, given that they are almost identical to ΛCDM at high redshift. Finally, Figure 3.10 displays the density contrast δ_i for matter constituents, and the total matter power spectrum $P(k)$ at $z = 0$. In this case, $\bar{\sigma}_8 = 0.84$ for $\overline{\text{BA}}$ and $\tilde{\sigma}_8 = 0.70$ for $\widetilde{\text{BA}}$. We find no qualitatively distinction in comparison with the previous examples.

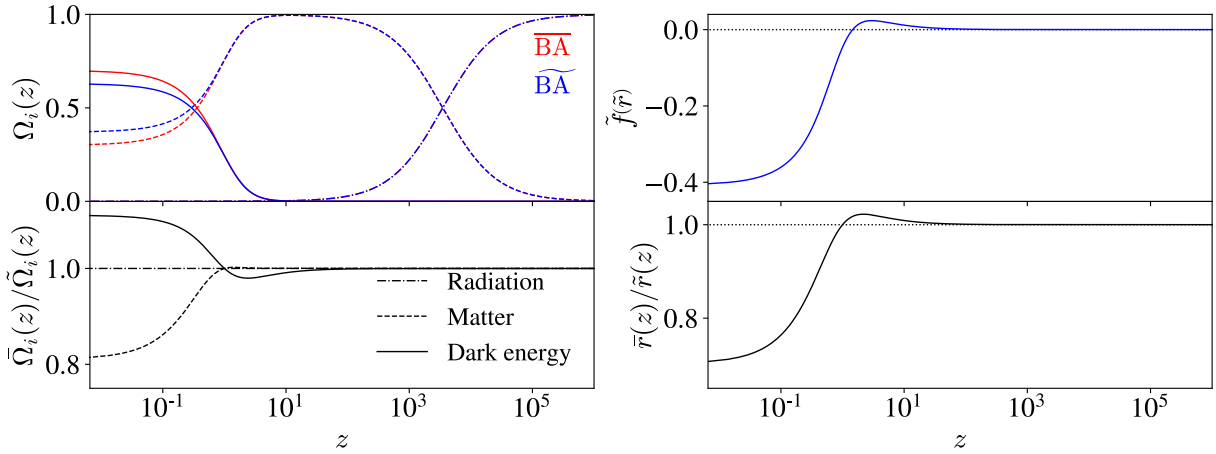

Figure 3.8: Background quantities for $\overline{\text{BA}}$ (in red) and $\widetilde{\text{BA}}$ (in blue). The cosmological parameters were set following Eq. 3.51. **Top left:** Evolution of $\Omega_i(z)$, $i = r, c, x$ represented in dashed, point and dash, and solid lines, respectively. Differences between the approaches become apparent only around $z = 10$, where DE is the dominant energy component. Radiation follows its usual $\propto a^{-4}$, since it's not included in the interaction for the dark fluid. **Bottom left:** Ratio of the dynamical and interacting density parameters. **Top right:** Interaction function $f(\tilde{r})$ ($\tilde{f}(\tilde{r})$ in the figure), the function decreases as DE gains significance. A dashed line at zero represents the case for null interaction. **Bottom right:** ratio between $\bar{r}(z)$, from the dynamical model and $\tilde{r}(z)$ from the $\widetilde{\text{BA}}$. The dotted line at $\bar{r}(z)/\tilde{r}(z) = 1$ represents the case where this models coincide, ΛCDM. Taken from Ref. [30].

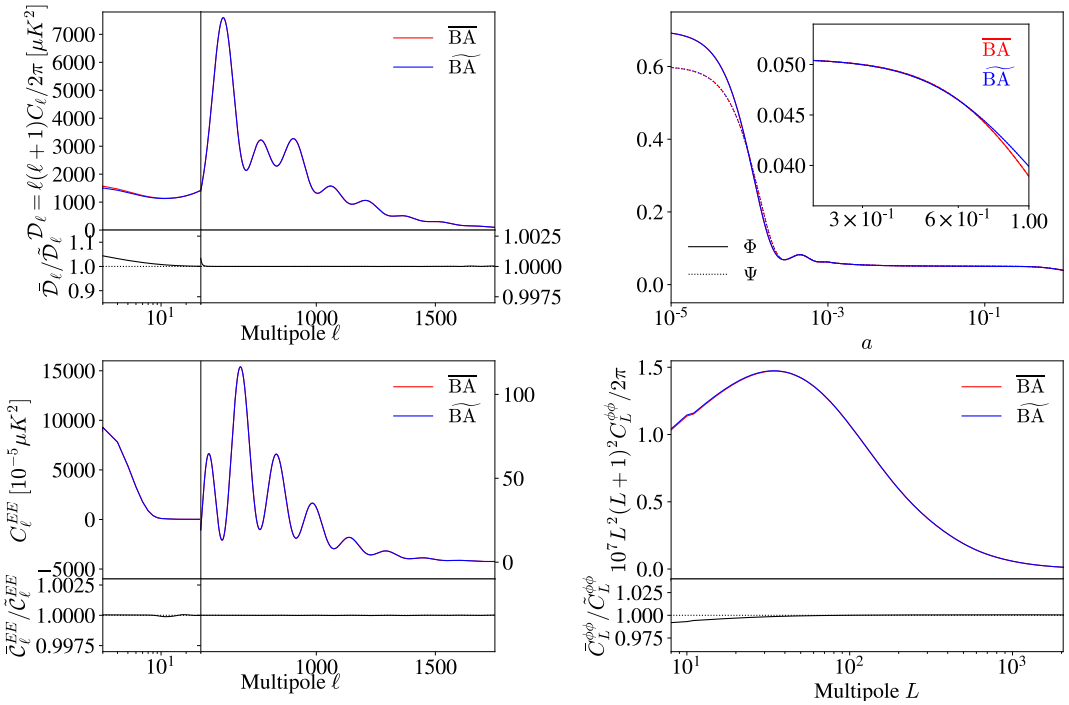

Figure 3.9: Quantities related to CMB power spectra for the $\overline{\text{BA}}$ (in red) and $\widetilde{\text{BA}}$ (in blue). **Top left:** lensed CMB power spectrum for temperature auto-correlation. **Bottom left:** lensed CMB power spectrum for polarization auto-correlation. **Top right:** gauge-invariant potentials Φ,Ψ at $k = 0.1$h/Mpc. Since we chose to avoid the degeneracy for perturbative linear level, these potentials are not identical in both approaches. . **Bottom right:** lensing potential power spectrum. Taken from Ref. [30].

3.3.4 Statistical Analysis

We present the results of the statistical analysis conducted in Ref. [30] using the particular cases addressed in Sec. 3.3. The results are split into two categories: background only and background + CMB data. This partition was made with the aim of separating the instance where the models are degenerated in contrast to the perturbative level, when including CMB. The datasets used for the background analysis were Pantheon (SN Ia) [125]; a compilation of 30 data points from cosmic chronometers (CC), from Ref. [140]; BAO measurements from 6dF [141] and BOSS DR12 [142]. The CMB measurements employed in this work come from Planck 2018 (TT,TE,EE,low E and lensing) [15]. In order to perform the Monte Carlo analysis, the programs CLASS [39], to compute the physics, and the software Monte Python [143], to perform the parameter estimation, were employed. For the background analysis, the set of free parameters were $\{\Omega_{c,0},\ H_0,\ w_0,\ w_a\}$ whereas for the CMB the standard base of Planck parameters, $\{\omega_b,\ \omega_c,\ H_0,\ \tau_{reio},\ \ln 10^{10} A_s\}$ was utilized. Additionally, for the latter, σ_8 was included as a derived parameter.

As we argued, we anticipate that $H(z)$ based observations provide the same results for both approximations, saved for $\Omega_{c,0}$. The findings of this analysis are reported in Table 3.1, where the ΛCDM was included for the sake of comparison. From this table, it

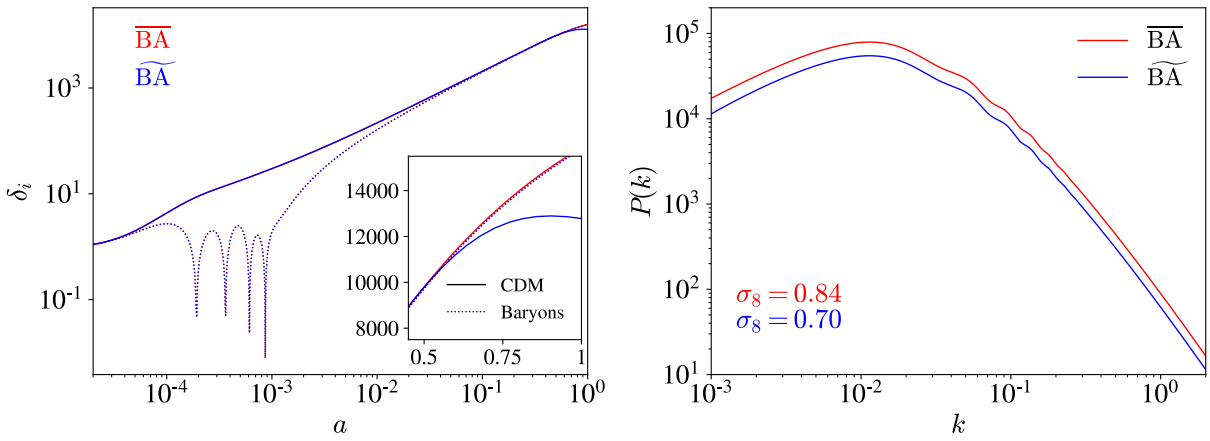

Figure 3.10: Behavior at perturbative scales for matter quantities in BA parameterization. Quantities for the dynamical model are represented in red ($\overline{\text{BA}}$), while the interacting model ($\widetilde{\text{BA}}$) is in blue. The cosmological parameters were set following Eq. 3.51. **Left:** density contrast for baryons (dotted lines) and CDM (solid lines) for $k = 0.1\,\text{h/Mpc}$. **Right:** Total matter power spectrum for $z = 0$. Taken from Ref. [30].

is possible to verify that $\tilde{\Omega}_{c,0} = \bar{\Omega}_{c,0} + \bar{\Omega}_{x,0}(1 + \bar{w}_x)$ holds true for all interacting cases. An image with the posterior distribution from Tab. 3.1 for $\Omega_{c,0}$ is shown in Fig. 3.11. Furthermore, since w_0, w_a for the coupled models are parameters related to the interaction, one can presume that their errors will be carried out to the $\Omega_c, 0$ and overall parameters affiliated to the CDM energy density. This widening of the error bars can be observed in Table 3.1, and is illustrated in Fig. 3.11 for the background data. Likewise, the dependence of CDM with (w_0, w_a) for the interactive scenario also implies that a correlation between quantities of CDM and the aforementioned EoS parameters is to expected. This correlation can be observed in the plots for the contours of the background statistical analysis, in Figures 3.12, 3.13 and 3.14.

Alternatively, when combining the background probes, SN Ia and BAO, with CMB, the degeneracy is broken. Even though the models are no longer degenerated, given our parameterization choices for perturbative scales, the differences in the CMB spectrum are not sufficient to distinguish the approaches from CMB data constrains. On the other hand, CMB measurements provide tight constrains for cosmological models, and will serve the purpose of studying the peculiarities of the interacting models. Table 3.2 summarizes the results for this dataset combination. The full table can be found in Table 2 of Ref. [30]. Figures 3.15, 3.16, 3.17 displays the contour plots for $\Omega_{c,0} - \sigma_8$, at 1σ and 2σ confidence level using CMB + SN Ia + BAO data. The error propagation originated by a dependency on (w_0, w_a) for the coupled models gains relevancy for this dataset combination. For all 3 cases studied, the constrains for the interactive approach are considerably larger than the 2σ region covered by their respective dynamical counterparts, which occurs due to error propagation from parameters such as w_0 on other cosmological quantities. Moreover, Fig. 3.18 presents a color coding plot for (w_0, w_a) correlation for the CPL and BA pairs.

We can notice that w_0 and w_a are visibly correlated to $\Omega_{c,0}$ for $\widetilde{\text{CPL}}$ and $\widetilde{\text{BA}}$, whereas for $\overline{\text{CPL}}$ and $\overline{\text{BA}}$, no traces of correlation are observed.

Model	$\Omega_{c,0}$	H_0	w_0	w_a
ΛCDM	$0.303^{+0.013}_{-0.012}$	$69.3^{+1.3}_{-1.4}$	–	–
$\bar{w}$CDM	$0.303^{+0.013}_{-0.013}$	$68.8^{+1.7}_{-1.8}$	$-0.999^{+0.045}_{-0.046}$	–
$\tilde{w}$CDM	$0.303^{+0.034}_{-0.029}$	$69.0^{+1.8}_{-1.7}$	$-0.998^{+0.046}_{-0.042}$	–
$\overline{\text{CPL}}$	$0.298^{+0.014}_{-0.016}$	$68.8^{+1.8}_{-1.6}$	$-1.043^{+0.072}_{-0.100}$	$0.39^{+0.69}_{-0.30}$
$\widetilde{\text{CPL}}$	$0.261^{+0.053}_{-0.086}$	$68.8^{+1.7}_{-1.7}$	$-1.055^{+0.069}_{-0.110}$	$0.38^{+0.74}_{-0.25}$
$\overline{\text{BA}}$	$0.298^{+0.014}_{-0.015}$	$68.6^{+1.8}_{-1.8}$	$-1.057^{+0.079}_{-0.088}$	$0.32^{+0.36}_{-0.27}$
$\widetilde{\text{BA}}$	$0.256^{+0.063}_{-0.071}$	$68.7^{+1.8}_{-1.8}$	$-1.058^{+0.079}_{-0.088}$	$0.32^{+0.38}_{-0.27}$

Table 3.1: Best-fit values and 1σ confidence level from statistical analysis for degenerated models with SN Ia, BAO and CC measurements. ΛCDM was included for comparison purposes. From Ref. [30].

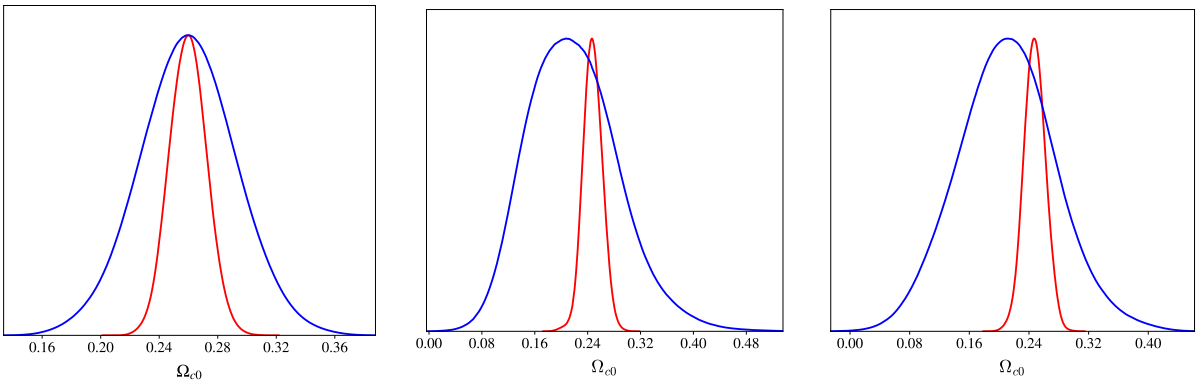

Figure 3.11: Posterior distribution of $\Omega_{c,0}$ (Ω_{c0} in the picture). The dynamical models are presented in red, while the interacting models are in blue. **Left:** wCDM. **Center:** CPL. **Right:** BA. From Ref. [30].

Parameter	ΛCDM	$\bar{w}$CDM	$\tilde{w}$CDM	$\overline{\text{CPL}}$	$\widetilde{\text{CPL}}$	$\overline{\text{BA}}$	$\widetilde{\text{BA}}$
$10^{-2}\omega_b$	$2.243^{+0.014}_{-0.013}$	$2.238^{+0.015}_{-0.015}$	$2.239^{+0.014}_{-0.015}$	$2.236^{+0.013}_{-0.014}$	$2.235^{+0.013}_{-0.015}$	$2.225^{+0.015}_{-0.015}$	$2.228^{+0.015}_{-0.016}$
ω_c	$0.1193^{+0.00094}_{-0.00091}$	$0.1198^{+0.0011}_{-0.0011}$	$0.1126^{+0.0120}_{-0.0090}$	$0.1201^{+0.0011}_{-0.0012}$	$0.1208^{+0.0250}_{-0.0240}$	$0.1194^{+0.0013}_{-0.0014}$	$0.1175^{+0.0215}_{-0.0210}$
H_0	$67.71^{+0.42}_{-0.42}$	$68.39^{+0.78}_{-0.81}$	$68.17^{+0.83}_{-0.90}$	$68.32^{+0.78}_{-0.85}$	$68.17^{+0.86}_{-0.83}$	$68.15^{+0.84}_{-0.83}$	$68.08^{+0.79}_{-0.80}$
w_0	–	$-1.031^{+0.034}_{-0.029}$	$-1.021^{+0.035}_{-0.032}$	$-0.963^{+0.081}_{-0.076}$	$-0.997^{+0.077}_{-0.076}$	$-0.987^{+0.071}_{-0.071}$	$-1.004^{+0.066}_{-0.065}$
w_a	–	–	–	$-0.27^{+0.30}_{-0.27}$	$-0.12^{+0.34}_{-0.26}$	$-0.08^{+0.16}_{-0.15}$	$-0.03^{+0.15}_{-0.14}$
σ_8	$0.8106^{+0.0060}_{-0.0063}$	$0.8197^{+0.0110}_{-0.0120}$	$0.8571^{+0.051}_{-0.079}$	$0.822^{+0.011}_{-0.012}$	$0.832^{+0.095}_{-0.170}$	$0.823^{+0.012}_{-0.012}$	$0.848^{+0.084}_{-0.153}$

Table 3.2: Best-fit values and 1σ confidence level from statistical analysis for degenerated models with CMB + SN Ia + BAO measurements. ΛCDM was included for comparison purposes. Adapted from Ref. [30].

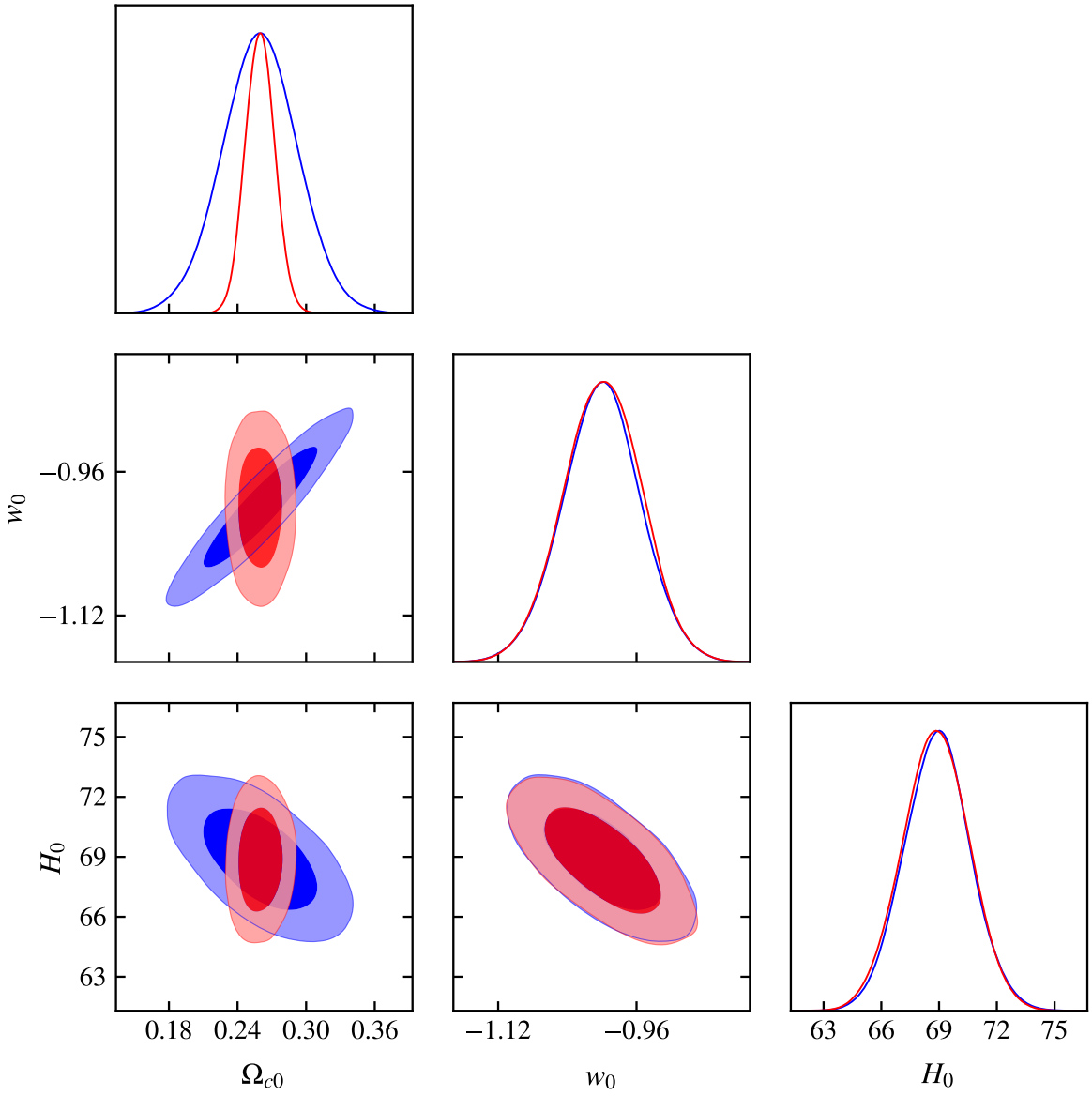

Figure 3.12: Countour plots for the wCDM pair with background data. The dynamical model ($\bar{w}$CDM) is shown in red and the coupled approach ($\tilde{w}$CDM) is in blue. The filled regions indicate 1σ (inner region) and 2σ (outer region) confidence levels. From Ref. [30].

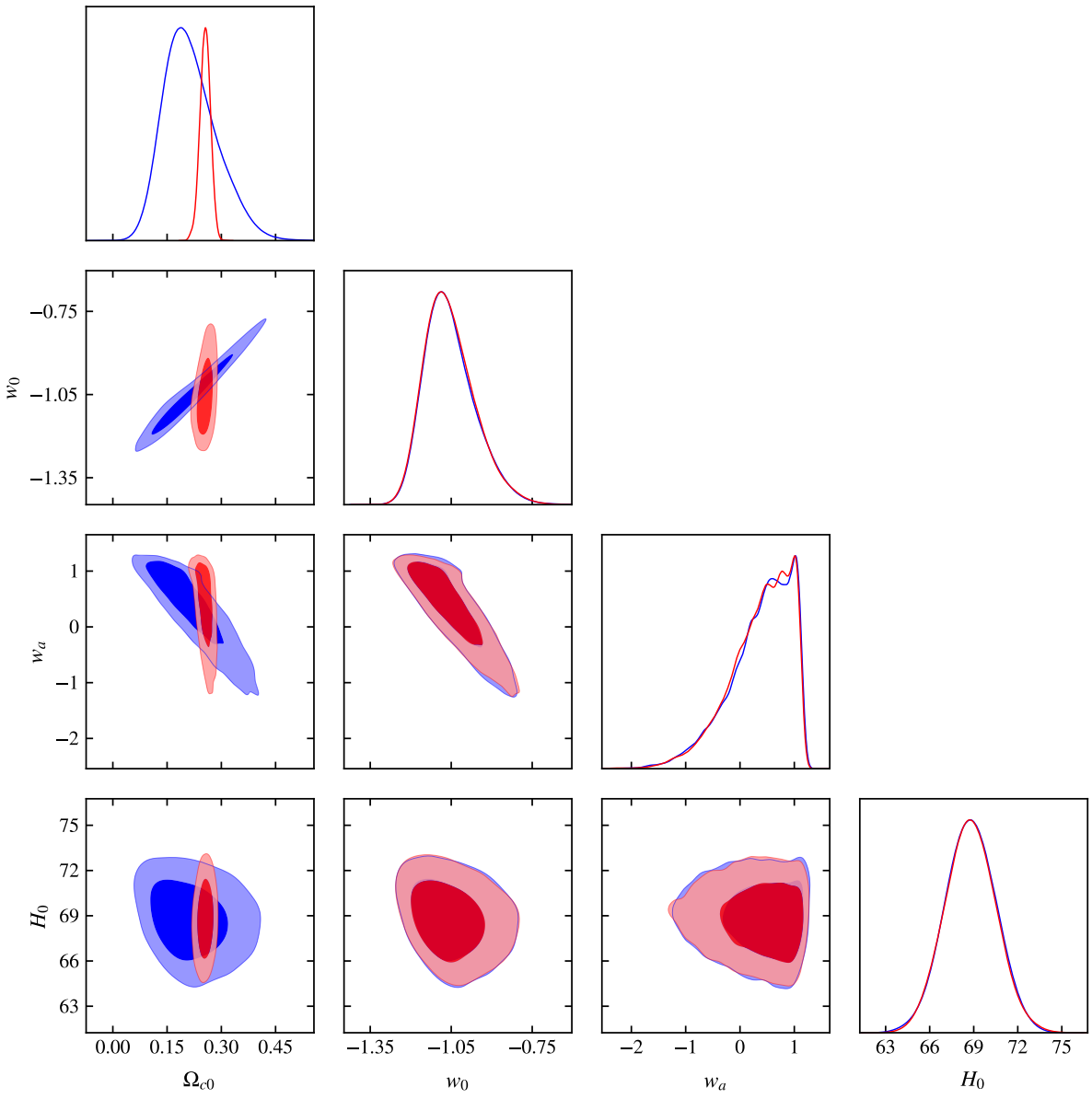

Figure 3.13: Countour plots for the CPL pair with background data. The dynamical model ($\overline{\text{CPL}}$) is shown in red and the coupled approach ($\widetilde{\text{CPL}}$) is in blue. The filled regions indicate 1σ (inner region) and 2σ (outer region) confidence levels. From Ref. [30].

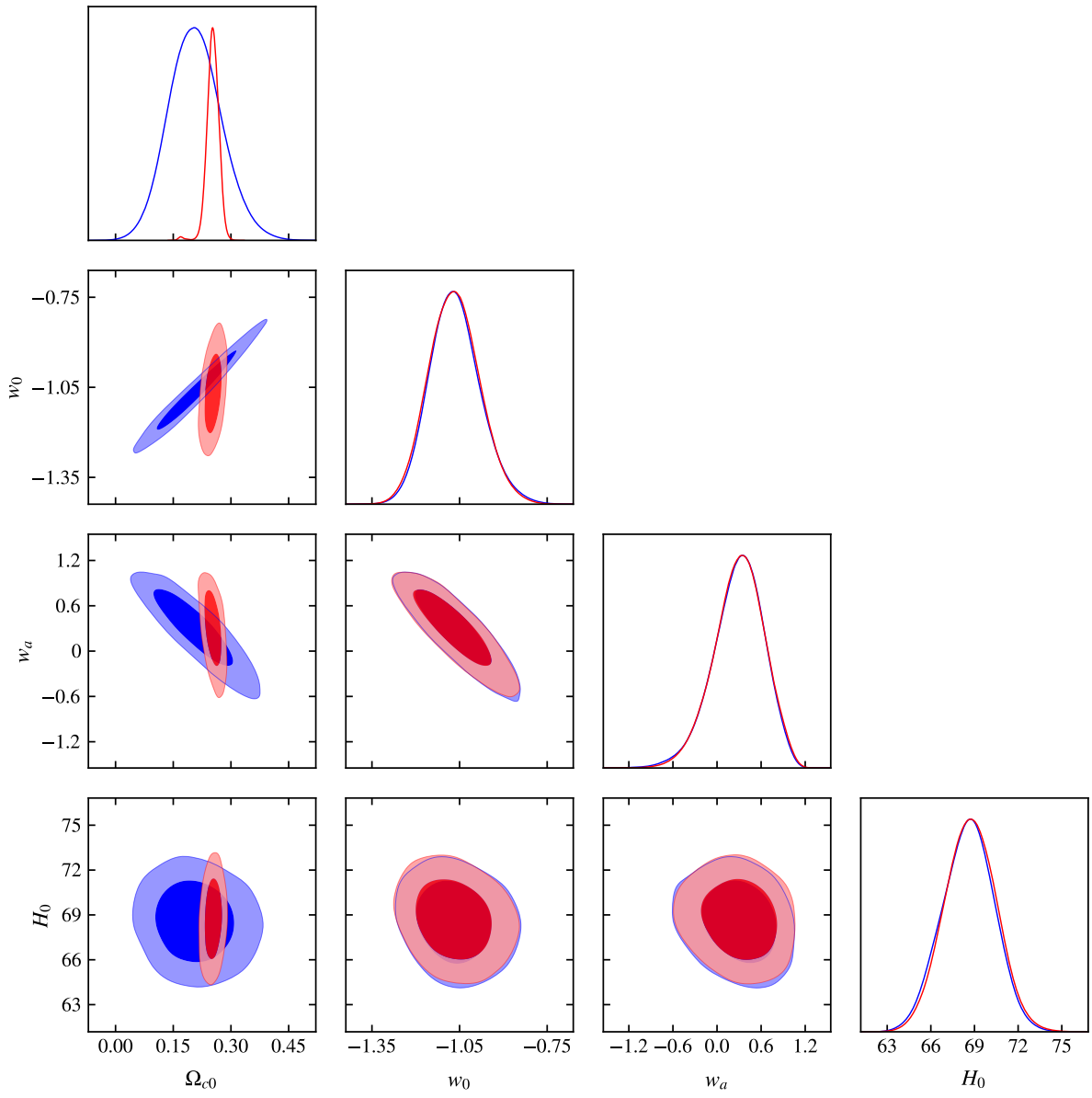

Figure 3.14: Countour plots for the BA pair with background data. The dynamical model ($\overline{\text{BA}}$) is shown in red and the coupled approach ($\widetilde{\text{BA}}$) is in blue. The filled regions indicate 1σ (inner region) and 2σ (outer region) confidence levels. From Ref. [30].

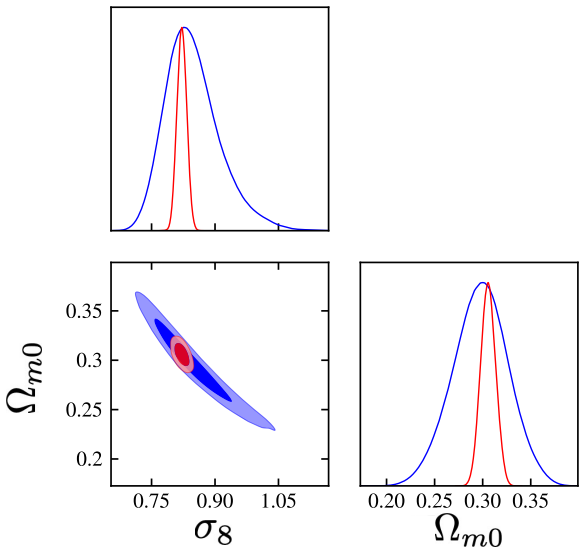

Figure 3.15: $\Omega_{c,0} - \sigma_8$ plane from the statistical analysis using CMB + SN Ia + BAO data for the wCDM parameterization. The dynamical approach, $\bar{w}$CDM, is represented in blue, while the interacting model, $\tilde{w}$CDM is in red. The filled regions indicate 1σ (inner region) and 2σ (outer region) confidence levels. Adapted from Ref. [30].

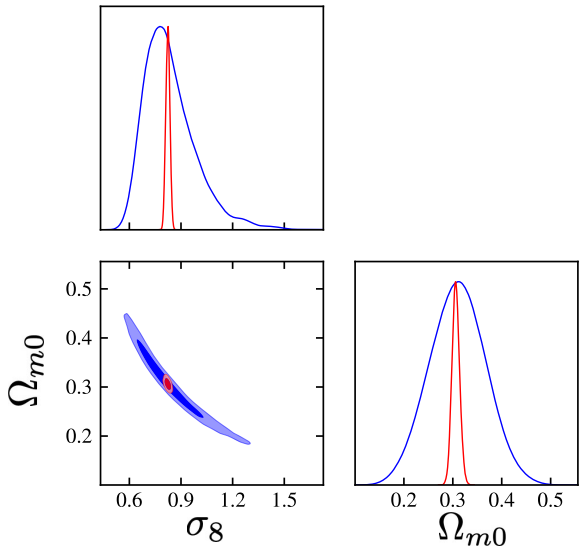

Figure 3.16: $\Omega_{c,0} - \sigma_8$ plane from the statistical analysis using CMB + SN Ia + BAO data for the Chavelier-Polarski-Linder (CPL) parameterization. The dynamical approach, $\overline{\text{CPL}}$, is represented in blue, while the interacting model, $\widetilde{\text{CPL}}$ is in red. The filled regions indicate 1σ (inner region) and 2σ (outer region) confidence levels. Adapted from Ref. [30].

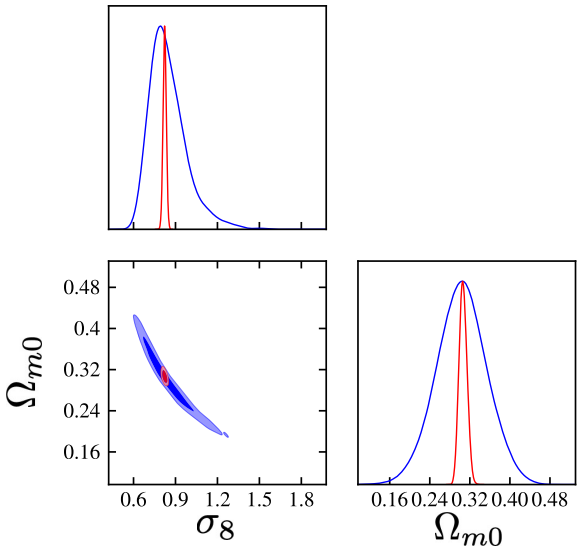

Figure 3.17: $\Omega_{c,0} - \sigma_8$ plane from the statistical analysis using CMB + SN Ia + BAO data for the Barboza-Alcaniz parameterization. The dynamical approach, $\overline{\text{BA}}$, is represented in blue, while the interacting model, $\widetilde{\text{BA}}$ is in red. The filled regions indicate 1σ (inner region) and 2σ (outer region) confidence levels. Adapted from Ref. [30].

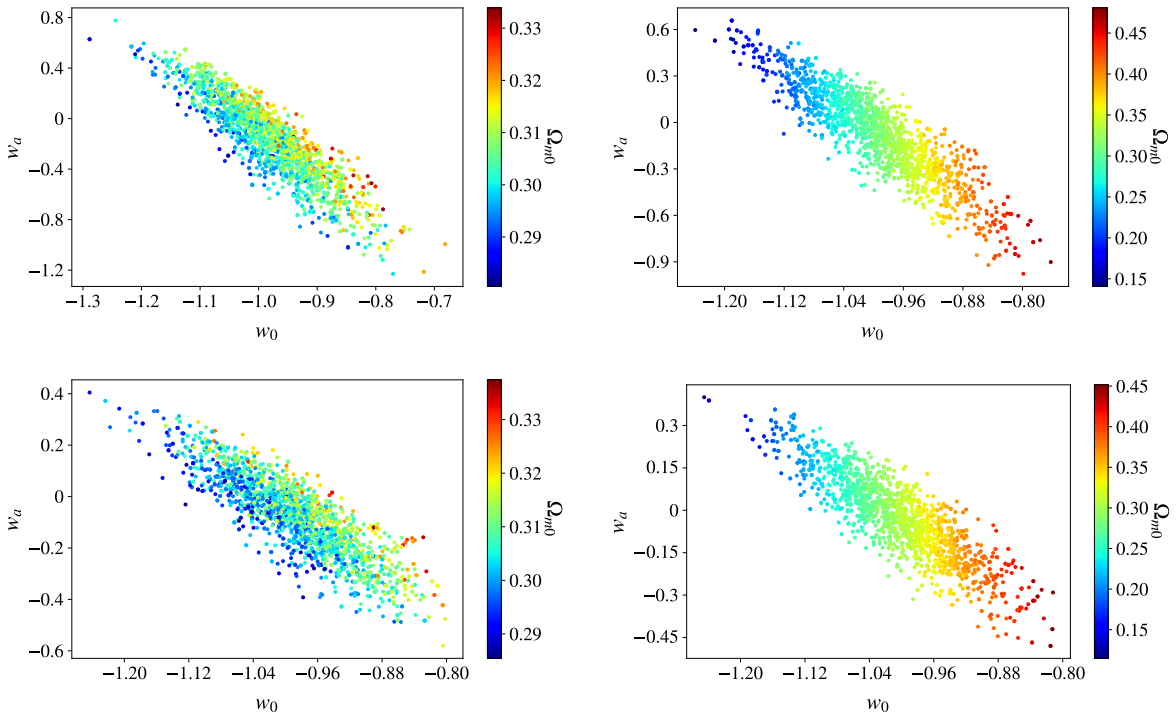

Figure 3.18: Color coded contour plot analysis with CMB + SN Ia + BAO data. **Top left:** $\overline{\text{CPL}}$. **Top right:** $\widetilde{\text{CPL}}$. **Bottom left:** $\overline{\text{BA}}$. **Bottom right:** $\widetilde{\text{BA}}$. Figure from Ref. [30].

Chapter 4

One-parameter dynamical dark energy model from the generalized Chaplygin gas

4.1 The non-adiabatic generalized Chaplygin gas (gCg)

4.2 Introduction

In this chapter, we'll focus on the inverse method as presented in Chapter 3 and Ref. [30]. That is, we seek to obtain the degenerated dynamical model from a given interaction. We study the particular case of a one-parameter dark energy from the well-known generalized Chaplygin gas (gCg) [144–149]. This chapter is organized in the following manner: In Section 4.3 we once more describe the background framework of the dark degeneracy, but now establishing the relations from the interacting approach to the (non-interacting) dynamical DE approach. Section 4.4 applies the obtained equations for the gCg model, which results in the background and perturbative descriptions. Lastly, Section 4.5 presents the observational data used in our analysis as well as the main constrains on the dynamical model parameters. The results of the analyses reported in this Chapter were published in Ref. [31].

4.3 Dark degeneracy

4.3.1 Mapping from interacting to dynamical approach

As aforementioned, the dark degeneracy enables us to determine a mapping from one scenario to the other. In Chapter 3, we considered two approaches in order to construct a mapping: (i) a dynamical non-interacting dark sector, whose EoS is $\bar{w}_x(a)$; (ii) an

interacting dark sector in which a cosmological constant ($\tilde{w}_x = -1$) is coupled to the (pressureless) dark matter. Likewise, we'll adopt these cosmological scenarios in order to obtain our relations for the interacting → dynamical mapping. The procedure to establish the relations for this case is identical to that presented in Sec. 3.2 in Eq. 3.14 to 3.31. The distinction lies in the quantities we aim to derive. While in Ch. 3 our goal was to find $(\tilde{\rho}_c, \tilde{\rho}_x)$ in terms of $(\bar{\rho}_c, \bar{\rho}_x)$, here, we are interested in determining $(\bar{\rho}_c, \bar{\rho}_x)$ from $(\tilde{\rho}_c, \tilde{\rho}_x)$, which is known for a given interaction. As previously discussed, the function of this coupling can be specified by either $f(\tilde{r})$, Q or $R(\tilde{\rho}_c, \tilde{\rho}_x)$. In that sense, Eqs. 3.32 and 3.33 can be rearranged to obtain

$$\bar{\rho}_x = \tilde{\rho}_c - \bar{\rho}_c + \tilde{\rho}_x \,, \tag{4.1}$$

$$\bar{w}_x = -\frac{\tilde{\rho}_x}{\tilde{\rho}_c - \bar{\rho}_c + \tilde{\rho}_x} \,. \tag{4.2}$$

Now, the quantities to be determined are $\bar{\rho}_x$ and $\bar{w}_x$, since CDM energy density evolves with a^{-3} for the dynamical model. On the other hand, the general solution for $\tilde{r}(a)$

$$\tilde{r}(a) = -\frac{1 + \bar{r}_0 a^{-3} \exp\left[3 \int \frac{1+\bar{w}_x(a')}{a'} da'\right]}{\bar{w}_x(a)} - 1, \tag{4.3}$$

is an integral equation, thus, there is one extra degree of freedom that must be fixed. Here, we adopt the following condition

$$\bar{w}_x \left(a = 1\right) = \bar{w}_0 \,. \tag{4.4}$$

Notice how, in contrast to the dynamical to interacting mapping, $\bar{w}_x(a)$ is the quantity that must be fixed, instead of being determined for a particular model, such as $\bar{w}$CDM, $\overline{\text{CPL}}$, $\overline{\text{BA}}$. More specifically when choosing $\bar{w}_x(a)$, we are ultimately fixing an interaction for our coupled model.

4.4 Decomposed generalized Chaplygin gas model

In this chapter, the designated interacting model was the generalized Chaplygin gas (gCg). The gCg was inspired by the Chaplygin equation, a differential equation present in aerodynamical studies. This gas has been applied cosmology as an attempt to unify the dark sector [150–153] and is characterized by the following EoS [144, 145]

$$p_{ch} = -\frac{A}{\rho_{ch}^{\alpha}} \,, \tag{4.5}$$

where the sub index "ch" designates quantities associated to the Chaplygin gas. Here, A is a strictly positive constant and α is a constant free parameter that must satisfy the

condition[1] $\alpha + 1 > 0$. The solution for the energy density is given by

$$\rho_{ch} = \left[A + \frac{B}{a^{3(1+\alpha)}} \right]^{\frac{1}{1+\alpha}} , \tag{4.6}$$

where B is a constant of integration. Although cosmological models based on the gCg have been widely studied in literature [146–149, 154], its adiabatic version presents instabilities in the matter power spectrum, as argued in [155]. Alternatively, when non-adiabatic perturbations are considered, the instabilities are removed [156–158], therefore making them a viable alternative to the dark sector.

On this basis, a viable proposal to introduce non-adiabaticities to the gCg model consists in diving it into interacting dark components, the so-called decomposed generalized Chaplygin gas [159, 160]. In this interacting scenario, the decomposed gCg model has already undergone several observational tests [161–164]. We refer the reader to Refs. [165, 166] for an updated analysis on the parameter selection for the decomposed gCg with the most recent available data.

4.4.1 (Interacting) Decomposed gCg

For our interacting decomposition of the gCg, we consider that the energy density and pressure of the gCg are divided into CDM and DE contributions:

$$\rho_{ch} = \tilde{\rho}_c + \tilde{\rho}_x \quad \text{and} \quad p_{ch} = \tilde{p}_x \, . \tag{4.7}$$

As in the previous chapter, we also impose that the DE component is described by a vacuum EoS, i.e., $\tilde{w}_x(a) = \tilde{p}_x/\tilde{\rho}_x = -1$, and the background energy conservation is given by Eq. 3.25. As already developed in Refs. [159, 160], the decomposed gCg is related to following source function

$$\tilde{Q} = 3H(1 + \tilde{w}_0) \frac{\tilde{\rho}_c \tilde{\rho}_x}{\tilde{\rho}_c + \tilde{\rho}_x} , \tag{4.8}$$

and the background energy densities are given by

$$\tilde{\rho}_c = \frac{8\pi G}{3H_0^2} \tilde{\Omega}_{c0} a^{3\tilde{w}_0} \left(\frac{\tilde{\Omega}_{c0} a^{3\tilde{w}_0} + \tilde{\Omega}_{x0}}{\tilde{\Omega}_{c0} + \tilde{\Omega}_{x0}} \right)^{-1-\frac{1}{\tilde{w}_0}} , \tag{4.9}$$

$$\tilde{\rho}_x = \frac{8\pi G}{3H_0^2} \tilde{\Omega}_{x0} \left(\frac{\tilde{\Omega}_{c0} a^{3\tilde{w}_0} + \tilde{\Omega}_{x0}}{\tilde{\Omega}_{c0} + \tilde{\Omega}_{x0}} \right)^{-1-\frac{1}{\tilde{w}_0}} . \tag{4.10}$$

[1] In the original gCg model (e.g. see Ref. [144]), we have instead the range $0 < \alpha \leqslant 1$. We note, however, that this particular range is motivated for a quartessence model where the gCg fluid acts as dark matter or dark energy at different times. In this work, we consider a decomposed dark sector where an interaction between its components is allowed. Instead, our choice for $\alpha + 1 > 0$ is motivated by the fact that, for our model, the gCg solution can also assume quintessence behavior.

The Eqs. 4.9 and 4.10 fully determine the background dynamics of the Universe in the interacting decomposed gCg scenario.

4.4.2 (Dynamical) Decomposed gCg

From now on, we will denominate the dynamical model obtained from the coupled decomposed gCg the $\bar{w}$gCg model. In practice, the $\bar{w}$gCg can be understood as a different decomposition of the gCg, where the dark components do not mutually interact and where the dark energy component is dynamical.

In order to obtain the background solutions in the dynamical approach, we combine Eqs. 4.1 and 4.2, where the CDM energy density in the dynamical approach is given by the first expression Eq. 3.16, and the interacting solutions are given by Eqs. 4.9 and 4.10, with the condition 4.4. This procedure leads us to the following solutions for the DE energy density and DE EoS parameter:

$$\bar{\rho}_x = \frac{8\pi G}{3H_0^2}a^{-3}\left[\left(\tilde{\Omega}_{c0}+\tilde{\Omega}_{x0}\right)^{\frac{1}{\tilde{w}_0}+1}\left(\tilde{\Omega}_{x0}a^{-3\tilde{w}_0}+\tilde{\Omega}_{c0}\right)^{-\frac{1}{\tilde{w}_0}}-\frac{\tilde{w}_0\left(\tilde{\Omega}_{c0}+\tilde{\Omega}_{x0}\right)+\tilde{\Omega}_{x0}}{\tilde{w}_0}\right], \quad (4.11)$$

$$\bar{w}_x = -\frac{\tilde{w}_0\tilde{\Omega}_{x0}(\tilde{\Omega}_{c0}+\tilde{\Omega}_{x0})^{1+\frac{1}{\tilde{w}_0}}}{(a^{3\tilde{w}_0}\tilde{\Omega}_{c0}+\tilde{\Omega}_{x0})\left(\tilde{w}_0(\tilde{\Omega}_{c0}+\tilde{\Omega}_{x0})^{1+\frac{1}{\tilde{w}_0}}-(\tilde{\Omega}_{c0}+a^{-3\tilde{w}_0}\tilde{\Omega}_{x0})^{\frac{1}{\tilde{w}_0}}(\tilde{\Omega}_{x0}+\tilde{w}_0(\tilde{\Omega}_{c0}+\tilde{\Omega}_{x0}))\right)}. \quad (4.12)$$

The Eqs. 4.11 and 4.12 fully determine the background dynamics of the Universe in the dynamical decomposed gCg scenario.

There are some important aspects of the dynamics of the $\bar{w}$gCg model that can be analyzed from those equations. First, from 4.12, we can conclude that, at $z = 0$, the DE EoS results in $\tilde{w}_0$. This means that the today's value of the DE EoS parameter $\bar{w}_x(z=0) = \bar{w}_0$ is identical to the interaction parameter $\tilde{w}_0$. Thus, in a similar way with what was argued for $\bar{w}_0$ in Section 3.3.1, from now on we also omit the bar/tilde in the w_0 parameter. Likewise, $\tilde{w}_0$ also reflects the deviation from ΛCDM model, independently of the approach. Second, Eqs. 4.11 and 4.12 are written in terms of the "interacting" parameters (with tildes). In reality, this is a mathematical convenience because in the dynamical scenario, only the "dynamical" parameters (with bars) have physical meaning. For example, the density parameters for CDM and DE components in the dynamical approach are given by

$$\bar{\Omega}_{c0} = \frac{w_0\tilde{\Omega}_{c0}+w_0\tilde{\Omega}_{x0}+\tilde{\Omega}_{x0}}{w_0} \quad \text{and} \quad \bar{\Omega}_{x0} = \frac{\tilde{\Omega}_{x0}}{w_0}. \quad (4.13)$$

It is possible to verify that Eq. 4.12 only produces physical solutions for $-1 < w_0 < 0$, and in all cases the EoS parameters is restricted to $w_0 \leqslant \bar{w}_x(z) \leqslant 0$. In practice, this

implies that the $\bar{w}$gCg model does not admit phantom dark energy solutions nor allows the EoS parameter to cross $w_0 = -1$. In this sense, the $\bar{w}$gCg delivers an one-parameter dynamical EoS for the DE component that naturally avoids the phantom regime.

In order to compute the background dynamics of the $\bar{w}$gCg, we utilize a modified version of the Boltzmann solver CLASS [39] with the equations developed in Sec. 4.4.2. The background solutions for $\bar{w}$gCg model considering some specific values for the parameter w_0 can be visualized in Figure 4.1. In the left panel, we show the time evolution of the EoS parameter of the DE component, while in the right panel of Fig. 4.1 we present the time evolution of the density parameter for all species. From this image, it is possible to observe that the DE component has a pressureless phase in the early Universe ($\bar{w}_x \approx 0$), shows a transient evolution to a negative EoS starting from $z = 10$, and reaches the value $\tilde{w}_0$ today, as imposed by the condition 4.4. This pressureless phase creates a "step" in the evolution of the DE component. As will be discussed later, this behavior plays a role in our perturbative analysis. A remarkable feature of this model is that the matter component never reaches unity (i.e., $\bar{\Omega}_m = 1$) in the interval $z = 1$ and $z = 10^3$. At first glance, one could assume that there is no matter dominated epoch for this model. However, during the aforementioned period, the DE is pressureless, therefore it behaves like matter, making a late-time transition to a negative pressure fluid.

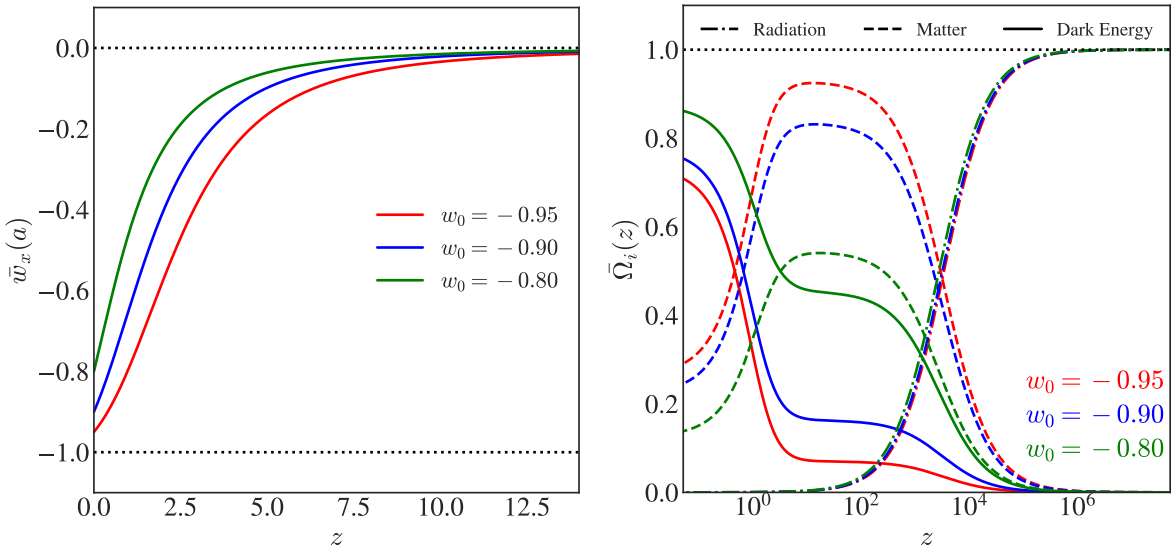

Figure 4.1: Background solutions for the $\bar{w}$gCg model for different values of w_0. Both plots consider $\tilde{\Omega}_{c0} = 0.25$, and the value of $\bar{\Omega}_{c0}$ can be obtained from Eq. 4.13. **Left panel:** EoS parameter in the dynamical approach for different values of w_0. In each case, the dark energy component behaves as matter in the early universe and transits to a negative $\bar{w}_x$ around $z = 10$. Due to physical bounds, $\bar{w}_x$ never reaches values below -1. **Right panel:** Density parameter for all matter species. The radiation component is denoted by the dashed-dotted line: the matter component, which contains CDM and baryons, is denoted by the dashed line; and the DE component is denoted by the solid line.

4.4.3 Perturbations

As argued in Chapter 3, the dark degeneracy at perturbative scales can be evaded for certain circumstances, and we'll adopt analogous conditions for this chapter as well. Nevertheless, in order to assess our model with the latest CMB data from Planck, we need to compute the perturbative cosmology. The perturbative equations for this model are described by equations 3.46, 3.47 (with $Q = 0$), valid for a perturbed FRLW metric at linear order and Newtonian gauge. Furthermore, for the (pressureless) CDM component, we fix, as usual, $w_c = 0$ and $c^2_{s,c} = 0$. On the other hand, for the DE component we use Eq. 4.12 for the EoS parameter, and, motivated by the scalar field sound speed, we set $c^2_{s,x} = 1$, which avoids DE from clustering. We recall that our model is not the conventional gCg, but the decomposed gCg model, therefore we are refrained from considering the standard adiabatic sound speed $c^2_{gcg} = -\alpha w_{gCg}$ for the DE component.

To evaluate the growth of perturbations in the $\bar{w}$gCg, we calculate the temperature anisotropies in the CMB and the matter power spectrum for different values of the parameters w_0 and $\bar{\Omega}_{c0}$. Fig. 4.2 presents the CMB power spectrum for our model for variations in the Eos parameter w_0 (left panel) and for different values for $\bar{\Omega}_{c0}$ (right panel). In the left panel, it is possible to observe that the model is very sensitive to w_0 values, offering changes in the format of the CMB power spectrum, mostly as the overall amplitude. In general, it is well-known that the overall amplitude of the CMB power spectrum depends on the time of the decoupling. Hence, since the parameter w_0 affects the expansion dynamics of the Universe, i.e., it affects the Hubble rate, this strong dependency of the CMB power spectrum in relation to w_0 is expected. For changes in $\bar{\Omega}_{c0}$, in addition to an increase in the amplitude, we can see the that the peak scales are slightly shifted to the left, which is compatible to a similar analysis in the context of the ΛCDM model.

Finally, the linear matter power spectrum for the $\bar{w}$gCg can be visualized in Fig. 4.3. Similarly to Fig. 4.2, the left panel showcases $P(k)$ obtained for different w_0, whereas the right panel presents variations for $\bar{\Omega}_{c0}$. As well as the CMB spectrum, we can notice from the left panel that the matter power spectrum is particularly sensitive to the w_0 parameter. More specifically, the higher the value for w_0, the greater the suppression suffered by the matter power spectrum. In order to understand this behavior, we must remember that despite the fact that the DE component acts like pressureless matter between $10^0 < z < 10^3$, it also has luminal sound speed ($c^2_{s,x} = 1$) at linear level, which prevents it from clustering. Thus, the suppression in $P(k)$ observed in Figure 4.3 occurs due to the fact that only a portion of the cosmic substratum (i.e., the dark matter component) is capable of clustering. In this sense, for the $\bar{w}$gCg, one could interpret the parameter w_0 as a quantity that prevents part of the matter from clustering. In right panel of Fig. 4.3, the effect of varying $\bar{\Omega}_{c0}$ in the linear matter power spectrum can be visualized. In this case, it is evident that the amplitude and the slope of the curve for large values of k

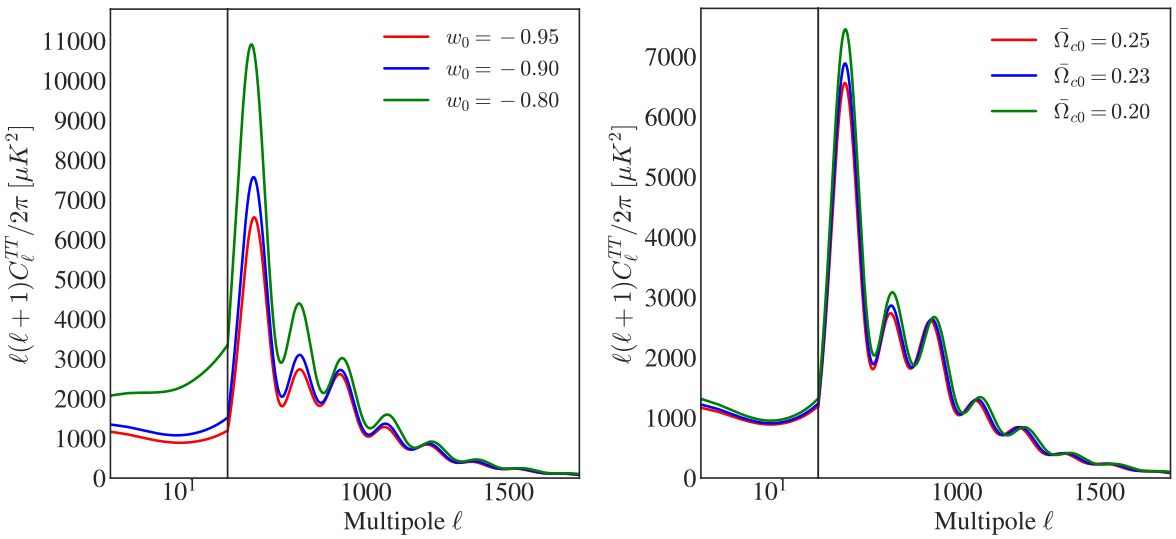

Figure 4.2: CMB temperature anisotropies power spectrum for the $\bar{w}$gCg model. **Left panel:** Results obtained with different values of w_0, fixing $\tilde{\Omega}_{c0} = 0.25$ (the value of $\bar{\Omega}_{c0}$ can be obtained from Eq. 4.13). **Right panel:** Results obtained with different values of $\bar{\Omega}_{c0}$, fixing $w_0 = -0.95$.

are slightly affected. Both of these well-known aspects can be are related to the matter density parameter: while the amplitude is associated to the DE density parameter, given by $\bar{\Omega}_{x0} \approx 1 - \bar{\Omega}_{c0} - \bar{\Omega}_{b0}$; the slope of power spectrum depends on the ratio $\bar{\Omega}_{b0}/\bar{\Omega}_{c0}$.

4.5 Statistical analysis

4.5.1 Cosmological data

The next step after analyzing the $\bar{w}$gCg model from the theoretical perspective is to validate it under observational constrains. In this context, combined with the Boltzmann solver CLASS, we make use of the statistical code `MontePython` [167] in order to perform a parameter selection with the recent data publicly available. In what follows we present the data used in this analysis:

- **SNe Ia:** For the supernovae Ia (SNIa) data, we use the Pantheon compilation [125]. This sample contains 1048 measurements of the apparent magnitude m for SNIa in the redshift range $0.01 \leqslant z \leqslant 2.3$. In this analysis, the absolute magnitude is considered as a nuisance parameter. The theoretical model enters in the luminosity distance.

- **BAO/RSD:** For the Baryon Acoustic Oscilation and Redshift Space Distortion, we consider the data from SDSS-DR7 Main Galaxy Sample [168], BOSS-DR12 (LRG) [169], eBOSS-DR16 (LRG, QSO and Lyα auto- and cross-correlation with

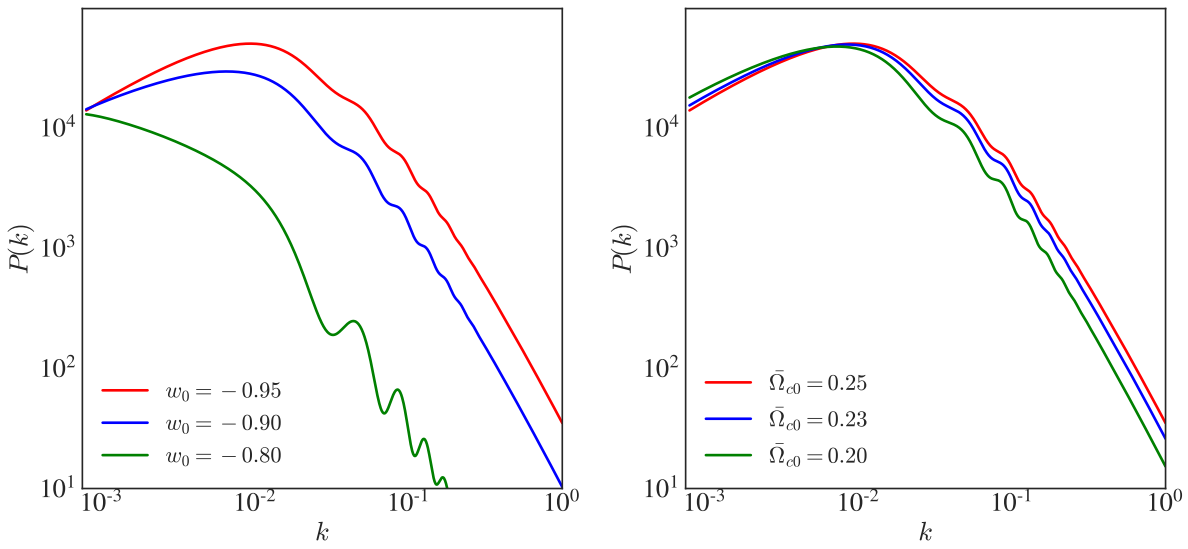

Figure 4.3: Linear matter power spectrum for the $\bar{w}$gCg model. **Left panel:** Results obtained with different values of w_0, fixing $\tilde{\Omega}_{c0} = 0.25$ (the value of $\bar{\Omega}_{c0}$ can be obtained from Eq. 4.13). **Right panel:** Results obtained with different values of $\bar{\Omega}_{c0}$, fixing $w_0 = -0.95$.

QSO) [170]. All these data have been obtained from galaxy/quasar clustering, however, rather than considering the full power spectrum, we employ the compressed information contained in: (i) the angular BAO feature from D_M/r_d; (ii) the BAO radial feature from D_H/r_d; and the anisotropic features in galaxy clustering from $f\sigma_8$. For the BAO angular quantity, the characteristic distance is related to the angular diameter distance (d_A) as $D_M \equiv (1+z)\, d_A$, and in the radial quantity, the characteristic distance is related to the Hubble rate via $D_H \equiv c/H$. Moreover, r_d is the sound-horizon distance evaluated out to the baryon drag epoch, f is the linear growth rate and σ_8 is the amplitude of mass fluctuations on scales on scale $8h^{-1}$Mpc. Although we consider these datasets to be independent, a covariance matrix is accounted for in different measurements inside each catalog. Additional information about this data combination, including a table with the specific quantities, measurements, mean redshifts and errors can be found in [171].

- **CMB:** In this analysis, we use the Planck 2018 data with information from temperature, polarization and temperature polarization cross-correlation spectra (TT, EE, TE), as well as the lensing maps reconstruction [15]. We considered the likelihood codes as follow:(i) the `COMANDER` likelihood version for low-ℓ TT spectrum, which contains data of the spectrum with $2 \leqslant \ell < 30$; (ii) the `SimAll` likelihood version for low-ℓ EE spectrum in the same interval of ℓ; (iii) the Plick TTTEEE likelihood version for the TT spectrum with $30 \leqslant \ell < 2500$ as well as the TE and EE spectra with $30 \leqslant \ell < 2000$; and (iv) the standard likelihood obtained from the lensing power spectrum reconstruction with $8 \leqslant L \leqslant 400$. A detailed description of the

likelihood codes can be found in Ref. [172].

- **Weak Lensing:** We utilize the weak lensing measurements from the KiDS-1000 [17, 173]. In this case, the relevant cosmological observable is the weak lensing power spectrum $\xi_{\pm}(\theta)$ for the auto- and cross-correlations across four tomographic redshift bins. Following the KiDS-1000 orientation, we make use of the COSEBIs (Complete Orthogonal Sets of E/B-Integrals [174]) as our summary statistic, and we employ the code HMCODE to perform our non-linear power spectrum calculations. Based on the fact that the HMCODE is able to compute the non-linear power spectrum for dynamical DE models [175], we assume that it provides the correct prediction for our model.[2]

4.5.2 Results

We combine the contributions for the background data, i.e., SN Ia and BAO/RSD in blue, while maintaining the CMB and weak lensing separated in order to study the impact of each dataset on this model. The results from our statistical analyses can be visualized in Figures 4.4 and 4.5, as well as Table 4.1. Aside from weak lensing, we find that w_0 is tightly constrained by the data. Notice that, since $\bar{w}_x(z) \geqslant -1$ for all z, our parameter selection only provides an upper-bound for w_0, with -1 being the lower bound. Furthermore, as we can see in Tab. 4.1, the constrains provided by SNIa+BAO and CMB allow for deviations from ΛCDM less than 1%. Such strong constrains indicate that our model affects considerably the CDM component at early times, which affects both the CMB and BAO physics. The joint analysis is not shown because it is fully dominated by the CMB data. We report that our results are in agreement with Ref. [176], where a study for different cases of interacting models, including the gCg, is performed. Finally, it is worth emphasizing that small deviations from ΛCDM are not sufficient to exclude the model here explored [177].

In order to assess how the model responds to the current observational tensions of the standard cosmology, we also compare the values obtained for H_0 with the H_0 value obtained by [178], $H_0 = 73.2 \pm 1.3$ km/s/Mpc. In what concerns the joint analysis with CMB, we find that the tension remains almost identical, due to the weight of the CMB data on the estimate of H_0. On the other hand, regarding the S_8 tension, when we compare the results for the plane $\Omega_m - S_8$ from Planck 2018 and KiDS-1000, we find that our model delivers predictions compatible with higher values of S_8 from weak lensing, causing both analyses, from CMB and weak lensing, to agree at $\simeq 1\sigma$ confidence level. We also notice that the uncertainties for S_8 have increased in relation to the ΛCDM scenario.

[2]The HMCODE has already been validated with numerical simulations for the Chevallier-Polarski-Linder (CPL) dynamical DE description [175]. We recognize the need of future N-body simulations that take into account the specifics of our model in order to validate our results.

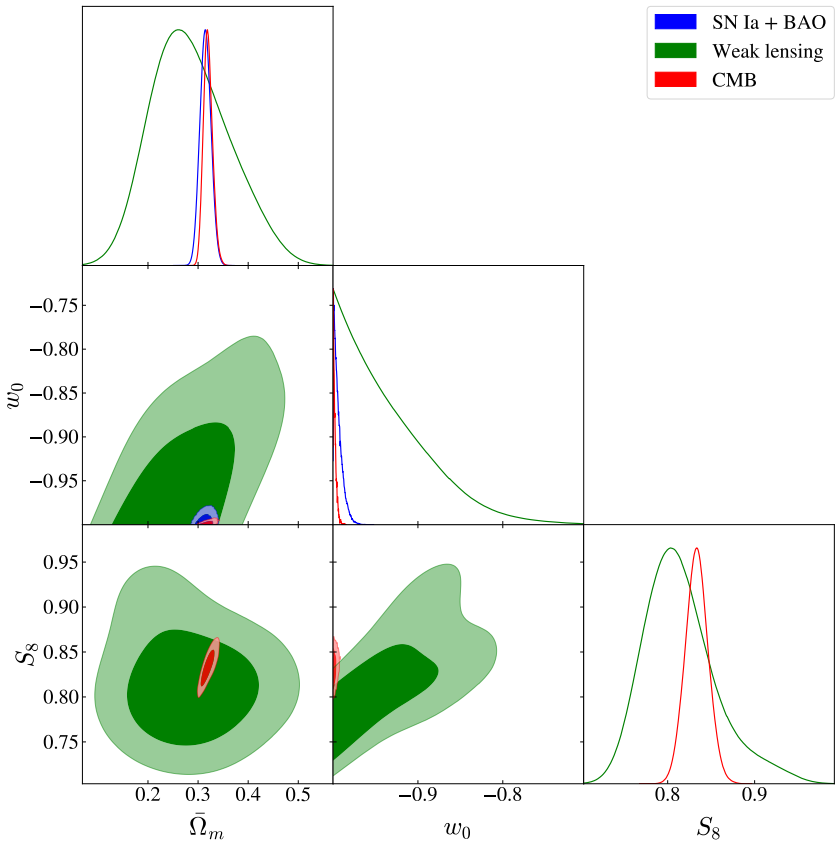

Figure 4.4: Corner plot of $\bar{\Omega}_m$, w_0 and S_8 for the statistical analysis for the $\bar{w}$gCg model. Each dataset is used in a different color: Weak lensing (green), SN Ia + BAO/RSD (blue) and CMB (red). The inner and outer regions represent 1σ and 2σ CL, respectively. We only find lower and upper limits for values of w_0, for which we find that the best constrains are offered by CMB and SN Ia + BAO/RSD, whereas weak lensing provides weak constraining power. For S_8, we find 1σ compatibility between datasets for $w_0 \simeq -1$, for which our model tends to ΛCDM.

This is expected, since the inclusion of a parameter for a model tends to propagate its uncertainties to the derived parameters, such as S_8. On the other hand, Fig. 4.4 shows that the wgCg can reach high values of S_8 compatible with weak lensing measurements, but only in the case $w_0 > -1$. However, CMB data constrains w_0 to be very close to -1, and brings back S_8 to its usual ΛCDM value. In other words, the S_8 tension could be resolved only at the expense of introducing a new w_0 tension.

$\bar{w}$gCg				
	w_0	$\bar{\Omega}_m$	H_0	S_8
SN Ia + BAO/RSD	< -0.992	0.315 ± 0.011	$70.5^{+1.4}_{-1.8}$	-
Weak Lensing	< -0.902	$0.282^{+0.071}_{-0.090}$	72.9 ± 5.0	$0.828^{+0.042}_{-0.073}$
CMB	< -0.997	$0.320^{+0.008}_{-0.010}$	$66.90^{+0.72}_{-0.60}$	0.833 ± 0.013

Table 4.1: Best fit and 1σ confidence level obtained for each sample used. Current constrains for our model only offer upper limits for w_0, which is also evident in Fig. 4.4. Aside from weak lensing we find tight constrains for the other parameters. We also find that the CMB data shows preference for higher values of H_0 when in comparison to ΛCDM scenario. As mentioned in Fig. 4.4, compatibility in 1σ between datasets is reached when our model tends to ΛCDM.

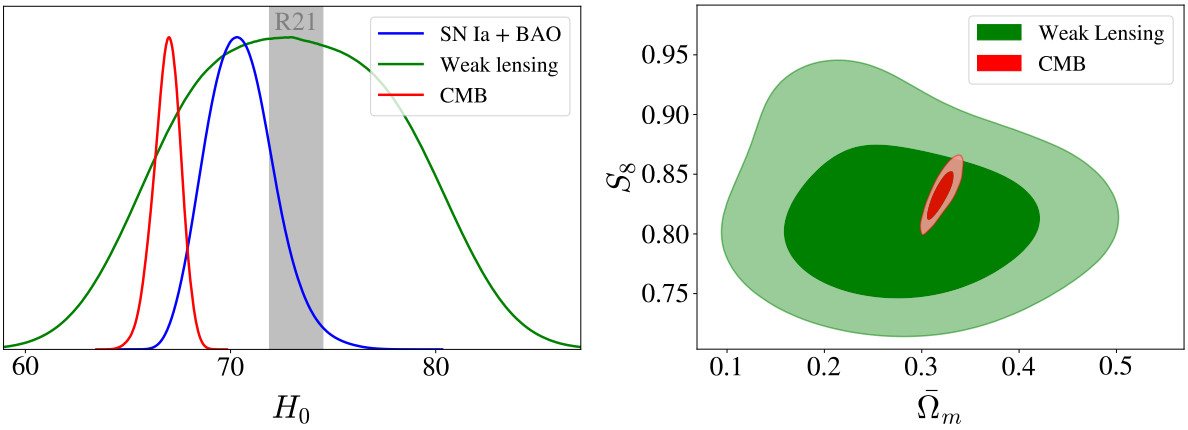

Figure 4.5: H_0 and S_8 distributions for $\bar{w}$CDM model. **Left panel:** H_0 posteriors for each dataset is presented in a different color: SN Ia + BAO/RSD (blue), weak lensing (green), CMB (red) for 1σ. The grey region represents the bounds for the value found in Ref. [178]. As seen in Tab. 4.1, the CMB possesses the highest constraining power for H_0, followed by SN Ia + BAO/RSD, while weak lensing provides the worst constraining power for the same parameter. **Right panel:** $S_8 - \bar{\Omega}_m$ plane obtained from weak lensing and CMB analysis. Once again, the inner and outer regions represent 1σ and 2σ CL.

Chapter 5

Assessing the dark degeneracy through gas mass fraction data

5.1 Introduction

In this chapter, we make use of the gas mass fraction from galaxy clusters, $f_{gas}(z)$, to perform a test for breaking this degeneracy at the background level. As mentioned in Section 1.2.1, this dataset provides measurements on Ω_c/Ω_m rather then $H(z)$ only, thus, it could in theory be able to distinguish the values of cosmological parameter on both approaches. We perform a statistical analysis for the degenerated pair (wCDM,$\tilde{w}$CDM) described in Section 3.3.1. The analysis is split for using $f_{gas}(z)$ alone, and its combination with SNIa, BAO and CMB. Furthermore, we obtain a model-independent $\Omega_{c,0}$ estimate from the reconstruction of $\rho_c(z)$ using f_{gas} in order to determine which approach is favored by the gas mass fraction data. We describe the observational data and the methodology applied for our statistical analyses in Sec 5.2. In Sec. 5.3, we report and discuss our main findings. The results reported in Sec. 5.3 of this chapter were published in Ref. [32].

5.2 Methodology

5.2.1 Observational data

We use datasets of complementary observational samples with the purpose of discussing a possible breaking of dark energy at background level. For the SN Ia, BAO and CMB, the cosmological data employed in this work is similar to the ones utilized in the analyses performed in Chapter 4. More specifically, we employ the Pantheon catalog [125] for the supernovae data; the BAO/RSD data compilation described in Sec. 4.5.1; as well as the Planck 2018 data for the lensed temperature, polarization auto- and cross power spectra, i.e., Planck 2018 TT,TE,EE+lensing.

Moreover, we utilize 40 measurements of gas mass fraction, $f_{gas}(z)$, calculated in

a spherical shell of $0.8 < r/r_{2500}^{ref} < 1.2$ from the center of the cluster, obtained from Mantz et al. [55] (hereafter M14). For this catalog, the fiducial cosmology assumed in the observations is the flat ΛCDM with $\Omega_{m,0} = 0.30$ and $H_0 = 70$ km/s/Mpc.

5.2.2 Statistical Analysis

We use modified versions of the Boltzmann solver CLASS [39] to compute the background evolution for our models and perform a Monte Carlo analysis with the `MontePython` code [179]. A likelihood code for `MontePython` was created in order to use the $f_{gas}(z)$ data from M14. Our algorithm does not perform the calibration between X-ray data and weak lensing, but rather follows the simplified analysis reported in [57], by using an external prior on K_0 from the Weighting the Giants project (WtG) [53]. This approach disconsiders a correlation between the cosmology used in the calibration and the cluster related parameters, but as stated in [53], this dependency is weak. Additionally, for the sake of simplicity, we chose not to include the intrinsic scatter at $f_{gas}(r_{2500})$, which is reportedly low ($\sim 7\%$) [55], and the mass dependency M_{2500} of the gas mass fraction.

With the intention of evaluating the effect of adding gas mass fraction data to break the degeneracy, we conduct three separate analyses for each model, separating the background data from CMB: $f_{gas}(z)$, $f_{gas}(z)$ + SNIa + BAO and $f_{gas}(z)$ + CMB. The priors adopted for each parameter in our $f_{gas}(z)$ analysis are presented in Table 5.1, while the external priors used for $100\,\omega_{b,0}$ and h are from Cooke et al.(2014) [180] and Riess 2021a [178], hereafter R21. Finally, we used the program `GetDist` [143], to analyze the MCMC chains generated by `MontePython`.

	Parameter	Prior
	Cosmological	
⋆	$100\,\omega_{b,0}$	$\mathcal{N}[2.202; 0.046]$
⋆	h	$\mathcal{N}[0.732; 0.013]$
	$\Omega_{c,0}$	$\mathcal{U}[0; 1]$
	w_0	-
	Astrophysical	
⋆	K_0	$\mathcal{N}[0.96; 0.09]$
	K_1	$\mathcal{U}[-0.05; 0.05]$
	Υ_0	$\mathcal{U}[0.763; 0.932]$
	Υ_1	$\mathcal{U}[-0.05; 0.05]$
⋆	η	$\mathcal{N}[0.442; 0.035]$

Table 5.1: Priors used for statistical analysis with f_{gas}. The Gaussian priors are represented with $\mathcal{N}$[Mean; Standard deviation], while uniform priors are noted as $\mathcal{U}$[Min; Max]. We used a star symbol (⋆) alongside the parameter name to indicate that the prior was external. For the EoS parameter w_0, for both the dynamical and interacting models, we used a wide (uninformative) prior.

5.3 Results

5.3.1 Gas mass fraction

Figure 5.1 presents our results for the statistical analysis and Table 5.2 for the gas mass fraction. A full triangle plot, including the nuisance parameters can be visualized in Figure 5.6. From Tab. 5.2, for $f_{gas}(z)$, we find $\Omega_{c,0}$ does not vary considerably in both models, however w_0 is significantly different in $\bar{w}$CDM to $\widetilde{w}$CDM, although both models are in agreement with ΛCDM at 2σ confidence level. We obtain a phantom dark energy at 1σ for $\bar{w}$CDM, which is in agreement with previous results for this particular model from this dataset [55, 57]. Additionally, when using gas mass fraction only, one can notice that the error bars are smaller for the interacting model, $\widetilde{w}$CDM, than for the dynamical case, $\bar{w}$CDM. This result can be explained by the fact that in the dynamical model the parameter w_0 only appears inside $H(z)$ in $d_A(z)$ and $A(z)$ and therefore constraints on this parameter are weak. In contrast, for $\widetilde{w}$CDM, w_0 appears in the expressions for $\tilde{\Omega}_c$, resulting in tighter constraints from f_{gas}. Furthermore, we find w_0 to be close to $w_0 = -1$, compatible with a weak interaction for this model. Likewise, in the same way that w_0 is poorly constrained for $\bar{w}$CDM by $f_{gas}(z)$, H_0 is also. Therefore, the analysis for H_0 essentially reproduces the adopted prior for this parameter. We find that the degeneracy was not broken at a background level for this dataset, given the small differences between the statistical analyses for $f_{gas}(z)$.

5.3.2 Combination with other probes

When including $f_{gas}(z)$ to SNIa+BAO, differences between w_0 shift notably in regards to the previous case (Figs. 5.2 and 5.3). This data combination provides more distinct values for $\Omega_{c,0}$, whereas w_0 substantially overlaps. We conducted the same analysis, but for $f_{gas}(z)$ + SNIa and $f_{gas}(z)$ + BAO, and found similar results. Furthermore, while the constrains for w_0 remain smaller for $\widetilde{w}$CDM, the error propagations for this model now play a bigger role constraining the other parameters. This can be visualized by the enlargement of the error bars for $\widetilde{w}$CDM in Fig. 5.2. See Figs. 5.7 and 5.8 for the full plots.

Lastly, we find comparable values for $\Omega_{c,0}$ for the $f_{gas}(z)$+CMB, but w_0 diverges. Such differences were anticipated, as per our choice for breaking the degeneracy at linear level. Moreover, we again find a phantom value for w_0 at more than 1σ for $\bar{w}$CDM. Just as in the case for $f_{gas}(z)$ alone, CMB results find a phantom value for $w_0 = -1.57^{+0.50}_{-0.40}$ (Table 4 in Ref. [15]) when using the same data from Planck. Since both f_{gas} and CMB datasets show a preference for phantom DE for this model, the net effect also results in a lower w_0. When analyzing $\widetilde{w}$CDM, we find that for either f_{gas} + SNIa + BAO or $f_{gas}(z)$ + CMB, w_0 is consistent with a vanishing interaction ($w_0 = -1$) at 2σ. Similarly to the analyses

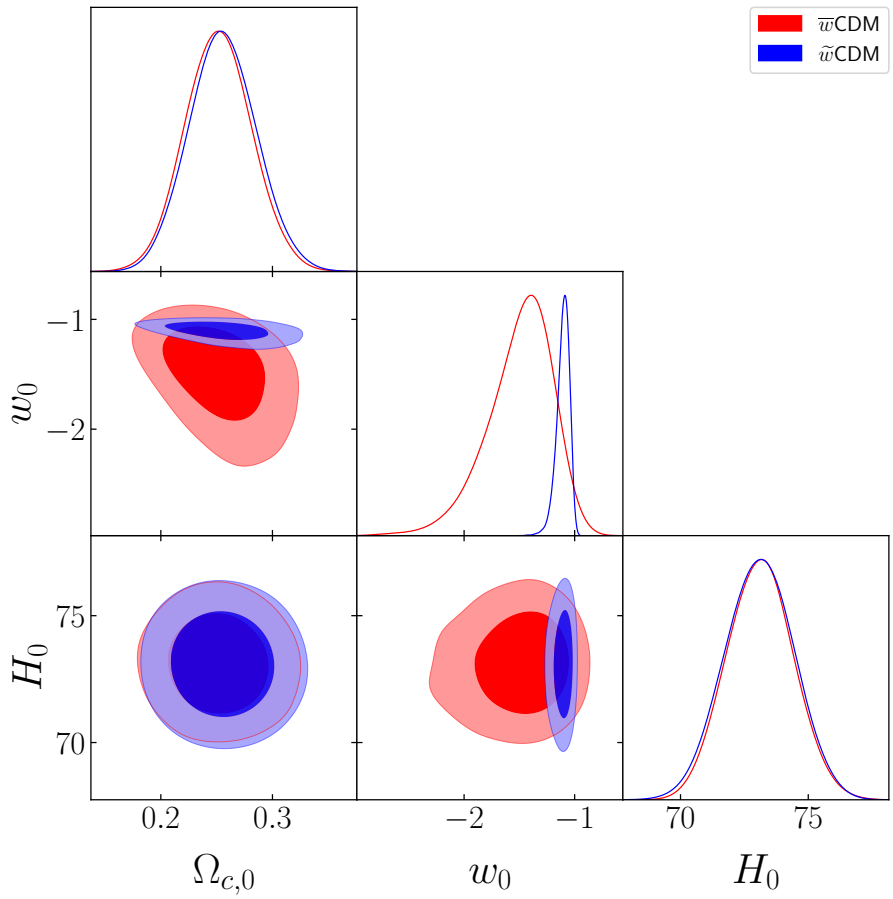

Figure 5.1: Triangle plot for $f_{gas}(z)$ data for $\bar{w}$CDM (red) and $\tilde{w}$CDM (blue). $\Omega_{c,0}$ is essentially the same in both approaches, while w_0 do not agree at 1σ. A phantom dark energy for $\bar{w}$CDM is in agreement with [55] [57]. For $\tilde{w}$CDM, the tight constraints for w_0 are due to the fact that this parameter appears directly in the expression for $\tilde{\Omega}_{c,0}$, as opposed to the dynamical case. On the other hand, the posterior distribution for H_0 is essentially a reproduction of the prior, as $f_{gas}(z)$ data imposes weak constraints on this quantity. We find the statistical differences between the two models to be insufficient to break the dark degeneracy in this analysis.

with only gas mass fraction, we find that combinations of $f_{gas}(z)$ with supernovae, BAO and CMB probes do no have an impact in breaking the dark degeneracy.

	Analysis	$\Omega_{c,0}$	w_0
$\bar{w}$CDM	$f_{gas}(z)$	0.252 ± 0.030	$-1.50^{+0.34}_{-0.22}$
	$f_{gas}(z)$ + SNIa + BAO	0.261 ± 0.011	-1.043 ± 0.038
	$f_{gas}(z)$ + CMB	$0.221^{+0.016}_{-0.021}$	$-1.209^{+0.088}_{-0.10}$
$\tilde{w}$CDM	$f_{gas}(z)$	0.256 ± 0.030	$-1.106^{+0.068}_{-0.042}$
	$f_{gas}(z)$ + SNIa + BAO	0.232 ± 0.017	-1.050 ± 0.024
	$f_{gas}(z)$ + CMB	0.228 ± 0.020	$-1.040^{+0.020}_{-0.023}$

Table 5.2: Mean and 1σ values found for the analysis performed for $\bar{w}$CDM and $\tilde{w}$CDM. When analyzing $f_{gas}(z)$ only, the models do not agree for the EoS parameter w_0 at 1σ C.L.. For $f_{gas}(z)$ + CMB, the variation in w_0 between the two approaches is expected, as we opted to break the degeneracy at linear scales.

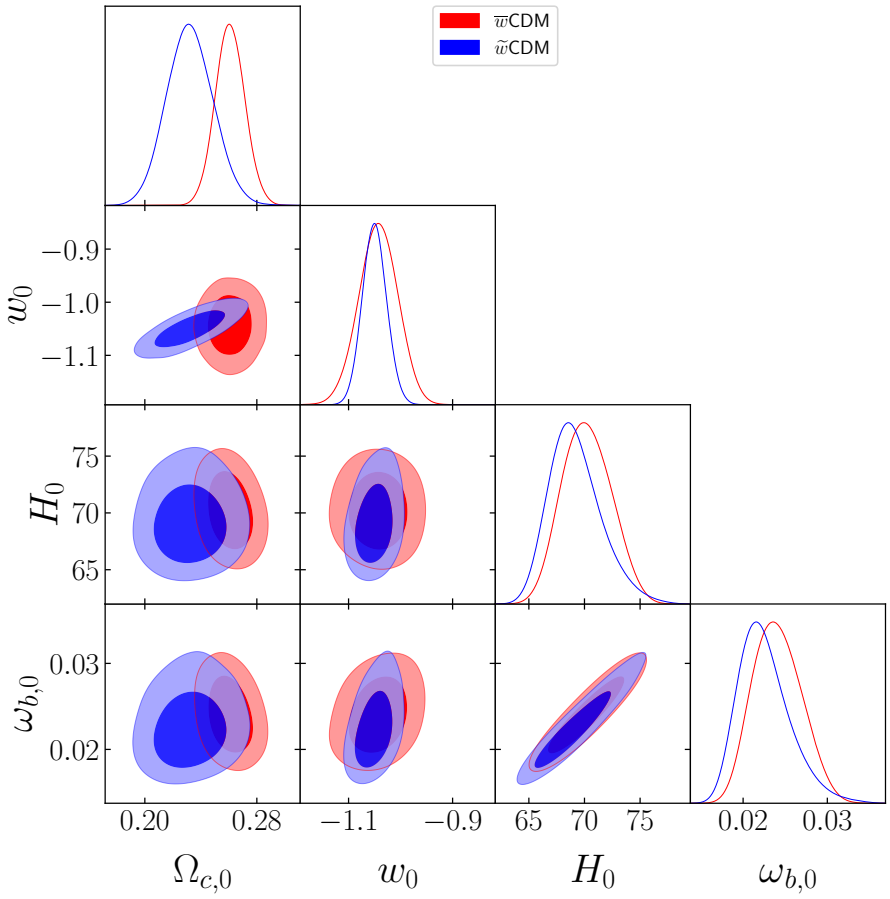

Figure 5.2: Triangle plot for $f_{gas}(z)$ + SNIa + BAO data. $\bar{w}$CDM is shown in red, whereas $\tilde{w}$CDM is shown in blue. Now, w_0 substantially overlaps, while differences in $\Omega_{c,0}$ for the two approaches become more apparent. Although the error bars for w_0 in $\tilde{w}$CDM remain tight, the error bars for the other parameters increase due to error propagation, in regards to $f_{gas}(z)$ only. Just as in the previous analysis, we find no substantial evidence for breaking the dark degeneracy with f_{gas} + SNIa + BAO.

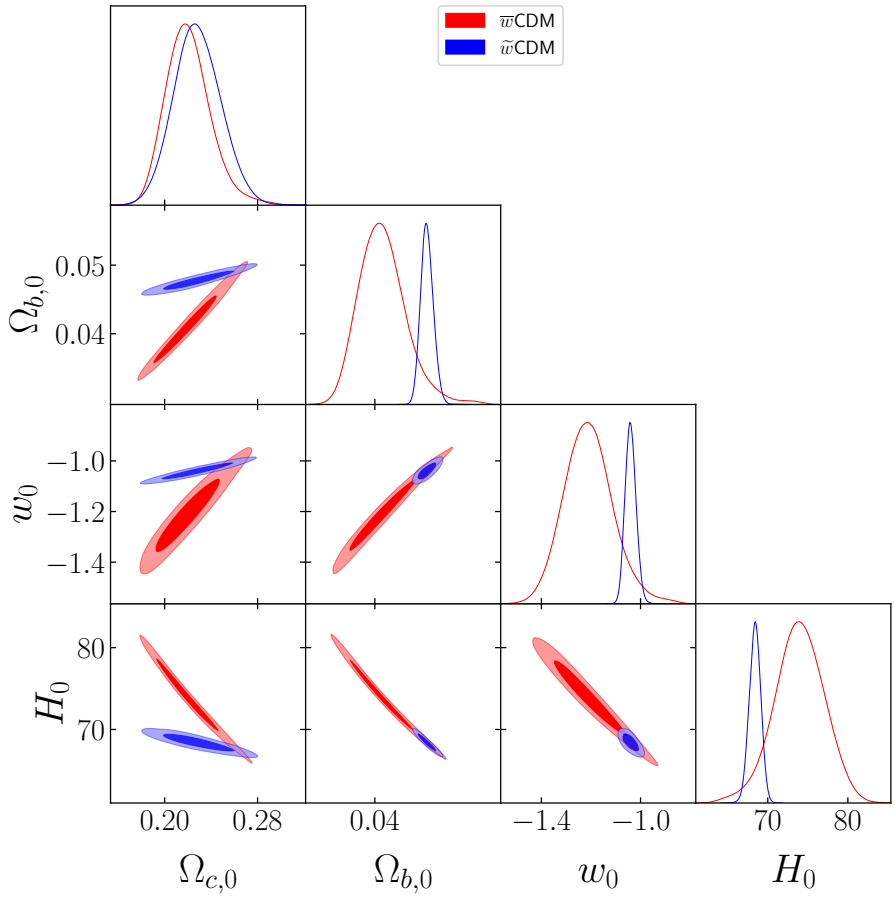

Figure 5.3: Triangle plot for $f_{gas}(z)+$CMB data. $\bar{w}$CDM is shown in red, whereas $\tilde{w}$CDM is shown in blue. Differences between the two approaches are expected for this analysis, given our choice to break the degeneracy at linear scales. Once again, the phantom w_0 for wCDM is consistent with the findings for both $f_{gas}(z)$ and CMB [15].

5.3.3 Model-independent determination of CDM energy density

With the purpose of assessing which model is favored by $f_{gas}(z)$ data, we compare our previous results with a model independent value of $\Omega_{c,0}$, obtained from a Gaussian process (GP) reconstruction of $\rho_c(z)$. We rewrite Eq. 1.69 as

$$\rho_c(z) = \rho_b(z)\Big[\frac{K(z)A(z)\Upsilon(z)}{f_{gas}^{ref}(z)}\left(\frac{d_A^{ref}(z)}{d_A(z)}\right)^{3/2} - 1\Big]. \tag{5.1}$$

We employ identical priors from Tab. 5.1 for the astrophysical parameters, as well as h and $100\,\omega_{b,0}$, and use M14 data to perform the GP reconstruction. We reconstruct $\rho_c(z)$ for five kernels and chose the one that maximized the GP marginal likelihood, Matérn(9/2) (M92). In this instance, we found $\rho_{c,0} = 29.1 \pm 6.4 \cdot 10^{-31}\mathrm{g/cm^3}$, corresponding to $\Omega_{c,0} = 0.29 \pm 0.06$, with $H_0 = (73.2 \pm 1.3)\,\mathrm{km/s/Mpc}$ (R21). Table 5.4 presents the results for all kernels tested, although they do not vary significantly. An image of this reconstruction is shown in Fig. 5.4. An analogous figure containing all the kernels used in this work is presented in Fig. 5.9.

We calculate the discrepancy $D = |X - Y|/\sqrt{\sigma_X^2 + \sigma_Y^2}$, where X and Y are the mean values of a given quantity and σ_X and σ_Y their respective errors, between our models' predictions for $\Omega_{c,0}$ and the model-independent value from GP. For the $f_{gas}(z)$, we find 0.53σ for $\bar{w}$CDM and 0.47σ for $\widetilde{w}$CDM. As presented in Tab. 5.2 and 5.1, the dissimilarities between the two approaches are small for $\Omega_{c,0}$, and exhibit no statistical relevance. The discrepancies for other samples is displayed in Tab. 5.3. For the data combination $f_{gas}(z) + \mathrm{SNIa} + \mathrm{BAO}$, we have the biggest difference between the discrepancies D, which is expected, as this data combination provides the most contrasting values of $\Omega_{c,0}$ for both models. On the other hand, the highest discrepancies are found for $f_{gas}(z) + \mathrm{CMB}$, which is attributed to the variations between $f_{gas}(z)$ and CMB data. Overall, we consider the discrepancies insignificant, and unable to determine a preference for any of the cosmologies tested. This is attributed both to the large errors associated to the current $f_{gas}(z)$ data and the similarities for the statistical analyses between $\bar{w}$CDM and $\widetilde{w}$CDM.

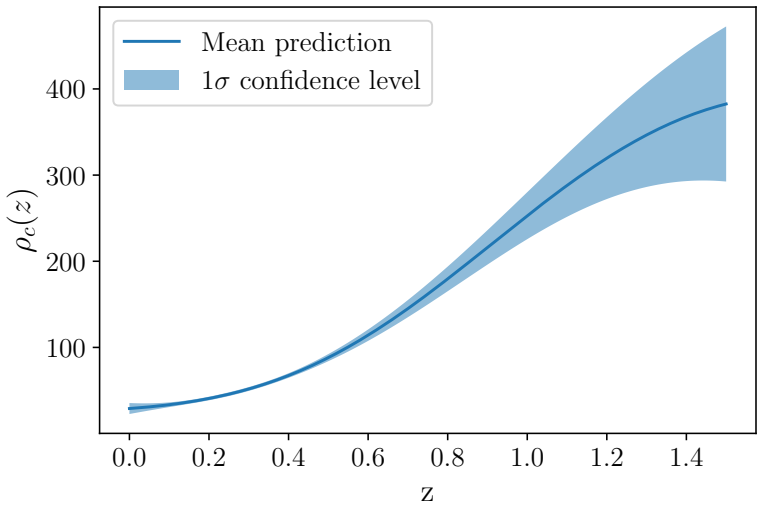

Figure 5.4: Values of the reconstructed ρ_c for GP using Matérn(9/2). Central values are denoted with a line, while the 1σ confidence level is represented by the shaded region.

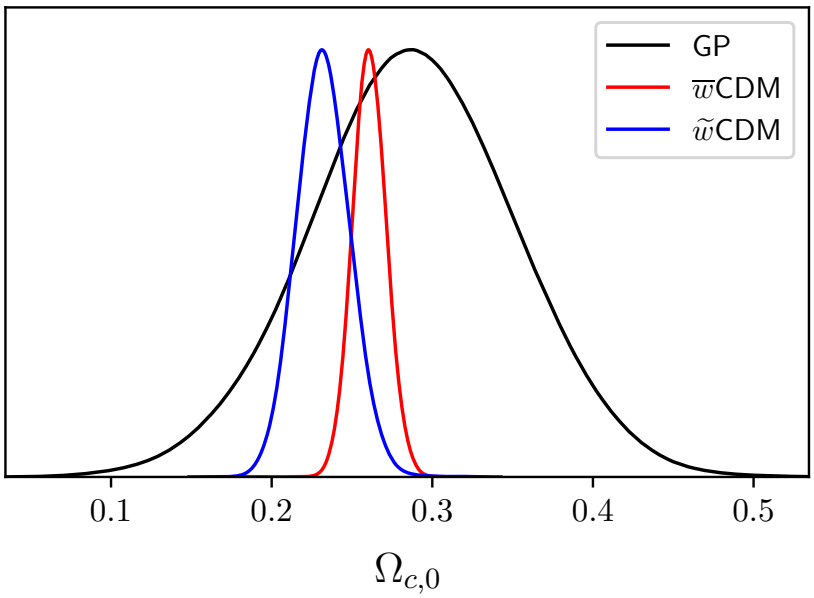

Figure 5.5: Result for $\Omega_{c,0}$ from M92 (in black), where $H_0 = 73 \pm 1.3\,\mathrm{km/s/Mpc}$ was employed. The red and blue curves are the results for $\bar{w}$CDM and $\widetilde{w}$CDM, respectively for the data combination $f_{gas}(z) + \mathrm{SNIa} + \mathrm{BAO}$.

	Analysis	Discrepancy(σ)
$\bar{w}$CDM	$f_{gas}(z)$	0.53
	$f_{gas}(z)$ + SNIa + BAO	0.43
	$f_{gas}(z)$ + CMB	1.04
$\tilde{w}$CDM	$f_{gas}(z)$	0.47
	$f_{gas}(z)$ + SNIa + BAO	0.86
	$f_{gas}(z)$ + CMB	0.91

Table 5.3: Discrepancies for $\bar{w}$CDM and $\tilde{w}$CDM in comparison with the $\Omega_{c,0}$ from the GP reconstruction, using $H_0 = 73 \pm 1.3\,\mathrm{km/s/Mpc}$. The biggest difference between models is found for $f_{gas}(z)$ + SNIa + BAO, while the highest discrepancies are found for $f_{gas}(z)$ + CMB. In general, we consider the discrepancies too small for a substantial preference for either $\bar{w}$CDM or $\tilde{w}$CDM.

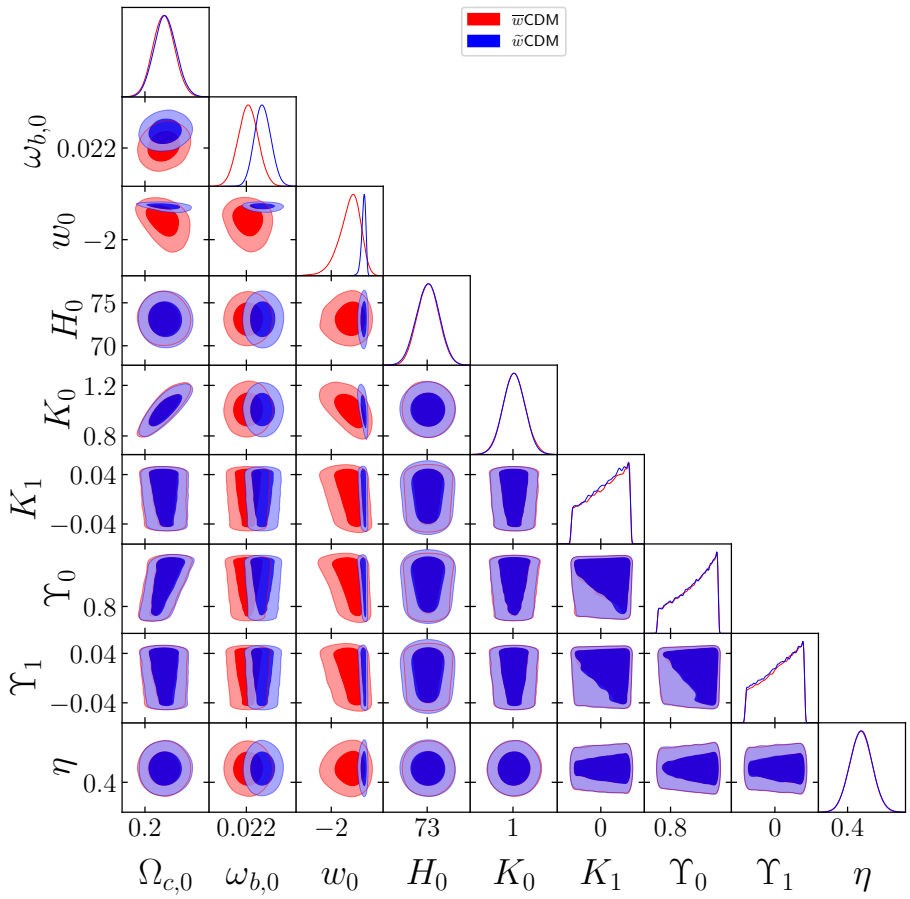

Figure 5.6: Full triangle plot for $f_{gas}(z)$. $\bar{w}$CDM is shown in red, whereas $\tilde{w}$CDM is shown in blue.

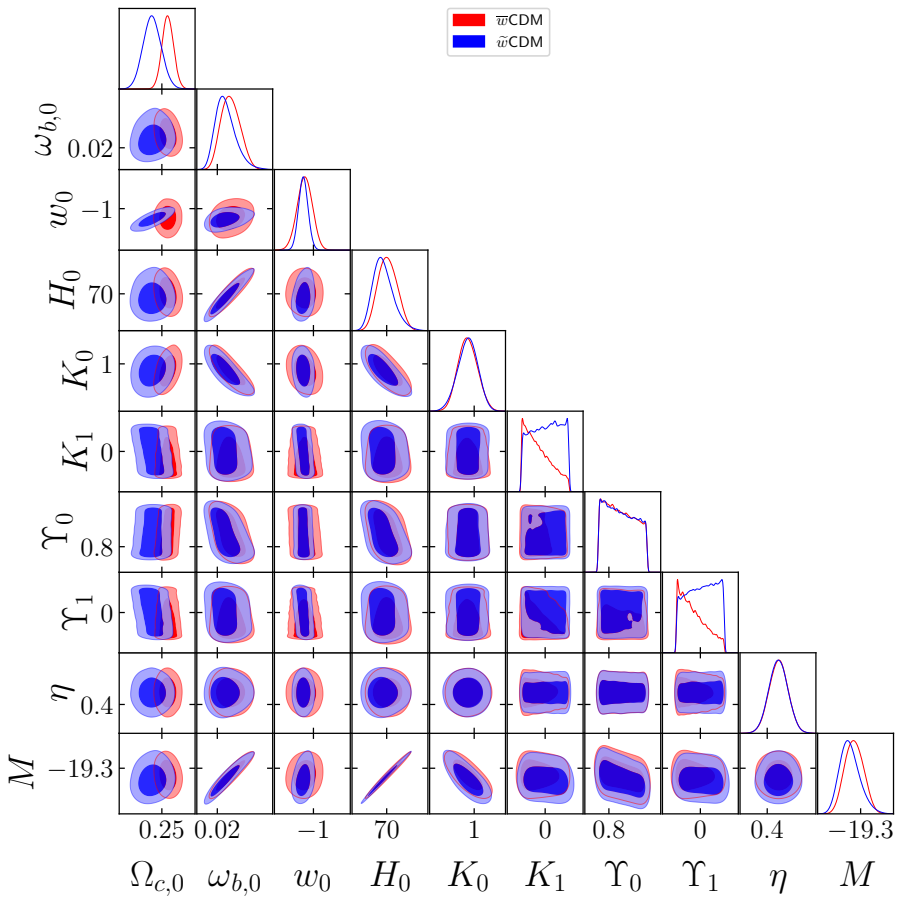

Figure 5.7: Full triangle plot for $f_{gas}(z)$+ BAO + SNIa data. $\bar{w}$CDM is shown in red, whereas $\tilde{w}$CDM is shown in blue.

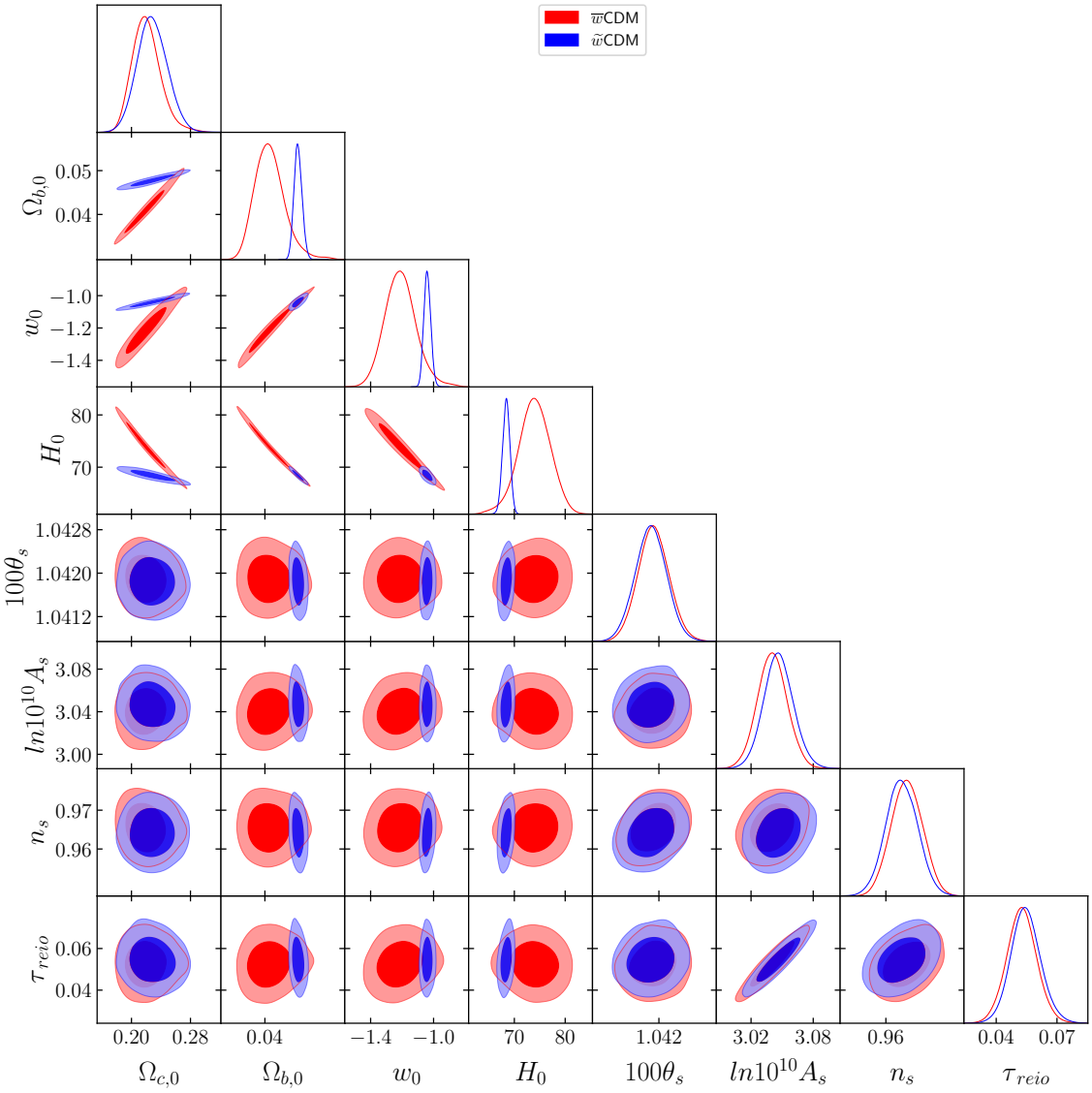

Figure 5.8: Triangle plot for $f_{gas}(z)$ + CMB data with nuisance parameters from CMB. $\bar{w}$CDM is shown in red, whereas $\tilde{w}$CDM is shown in blue.

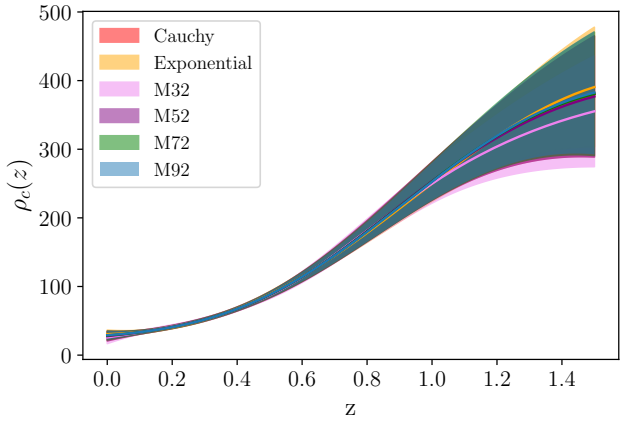

Figure 5.9: Gaussian process results with all kernels. M92 stands for the kernel Matérn(9/2), M72 for Matérn(7/2) and so on. As in Fig. 5.4, the best-fit values are denoted with a line, and the 1σ confidence level is represented by the shaded region.

Kernel	$\rho_{c,0}[10^{-31}\frac{g}{cm^3}]$	$\omega_{c,0}$	$\Omega_{c,0}$	Loglike
M92	29.1 ± 6.4	0.14 ± 0.03	0.29 ± 0.06	-161.1678
M72	28.6 ± 6.6	0.14 ± 0.03	0.28 ± 0.07	-161.2062
M52	27.7 ± 7.0	0.14 ± 0.04	0.28 ± 0.07	-161.3676
M32	25.7 ± 8.9	0.13 ± 0.05	0.26 ± 0.09	-162.2346
Exponential	30.6 ± 6	0.15 ± 0.03	0.30 ± 0.06	-161.1727
Cauchy	29.1 ± 6.4	0.14 ± 0.03	0.29 ± 0.06	-161.1766

Table 5.4: Results for GP for different kernels. M92 stands for the kernel Matérn(9/2), M72 for Matérn(7/2) and so on. For $\Omega_{c,0}$, we used $H_0 = (73.2 \pm 1.3)$ km/s/Mpc

.

Chapter 6

Conclusions and Perspectives

The theoretical and technological advancements in the past century have elevated cosmology to a science of precision, as well as establishing the ΛCDM as the best cosmological model up to date [15–21]. Nonetheless, the physical nature of the dark sector, equivalent to $\sim 95\%$ of the total energy density of the Universe, remains undetermined, due to the fact that all observations of its components are indirect. In this sense, our unfamiliarity with the dark sector motivates the pursue of alternative cosmologies, such as time dependent equations of state [72–74] and scalar fields [75].

Additionally, the possibility of a non-gravitational coupling between DE and DM has also been considered in the literature [85–87], since there is no reason, *a priori*, to assume that the dark components do not interact. In this sense, phenomenological models offer a route to explore this supposition, without resorting to the complexities of particle physics. While numerous forms of interactions have been proposed [29, 88–92, 95–97, 117], some models face instabilities at perturbative level, or violate the weak energy condition [87, 107]. When confronted with observational data, results for coupling models normally favor a small interaction in the dark sector compatible with ΛCDM at few sigma. Nevertheless, this hypothesis cannot be discarded as of yet.

Furthermore, a degeneracy in the dark sector arises from the Einstein field equations, making it impossible for models with the same total value of energy-momentum tensor to be completely distinguished by certain types of data [24–29]. This dark degeneracy is inevitable at scales where the Universe obeys the Cosmological Principle, while can be circumvented with the right parameterization choices at linear perturbative level. Even so, being able to differentiate the models at smaller scales is not always possible for all types of data [30]. The dark degeneracy has also been discussed in the literature in the context of interacting models [26, 28, 30]. Most notoriously, Ref. [30] developed connections between quantities of degenerated models with dynamical and interacting scenarios, where in the latter, the dark sector is constituted by dark matter interacting with a cosmological constant.

Throughout this thesis, we have investigated ways to obtain a better understanding

of the dark degeneracy and to contribute to the works on this subject already present in the literature. In Chapter 4, we studied how an interaction based on the generalized Chaplygin gas could act as a dynamical DE model, the $\bar{w}$gCg. We showed that the dark degeneracy mapping for this particular case leads to a time varying one-parameter EoS parameter for the DE component. This result has two remarkable features: (i) we found a dynamical evolution for the DE component with a single parameter; and (ii) the resulting $\bar{w}_x(z)$ naturally does not cross the phantom line, thereby satisfying $0 > \bar{w}_x(z) \geqslant \bar{w}_x(z=0) = w_0$ and avoiding instabilities. Another interesting property of the $\bar{w}$gCg is that at early times the DE EoS behaves as a pressureless component. Considering a DE luminal sound speed, it affects the clustering in the matter-dominated epoch. In that sense, the model works as a mechanism that prevents all pressureless component of clustering. From the observational perspective, we showed that the current available data sets, specially CMB, provide strong constraints on the extra parameter w_0, in good agreement with the ΛCDM model. We also briefly discussed the current tensions of cosmology in light of the model, and found that while it does not have much impact on the H_0 values, the S_8 tension can be alleviated to 1σ, but only at the cost of introducing a tension in w_0.

In Chapter 5, we explored the possibility of breaking this degeneracy in the background by employing $f_{gas}(z)$ data, which offers direct measurements Ω_c. We studied one of the parameterizations discussed in Ref. [30], the ($\bar{w}$CDM, $\widetilde{w}$CDM) pair. We performed a parameter estimation for different datasets and found that the degeneracy is not broken from the current $f_{gas}(z)$ data alone or combined with other probes. We compare these results with a model-independent value for $\Omega_{c,0}$ obtained through Gaussian Process by calculating the discrepancies for $\Omega_{c,0}$ in each analysis. Our results show no statistically significant preference for either of the evaluated cosmologies. We also find $\widetilde{w}$CDM to be consistent with a vanishing interaction at $\simeq 2\sigma$ for all data combination employed.

Overall, we expect future experiments to provide significantly tighter constrains for interacting models, contributing with information for the viability of this hypothesis. Moreover, if the next generations of $f_{gas}(z)$ measurements are able to considerably lower its error bars, gas mass fraction data could become a remarkable probe for breaking the dark degeneracy, especially when combined with other experiments. If, in addition to that, another type of background data independent of $H(z)$ is considered, we expect to obtain more constraining results for the dark degeneracy at background level.

Bibliography

[1] Albert Einstein. Die feldgleichungen der gravitation. *Sitzungsberichte der Königlich Preußischen Akademie der Wissenschaften*, pages 844–847, 1915.

[2] Albert Einstein. Die grundlagen der allgemeinen. *Relativitats- teorie, Annale der Physic*, 49:769, 1916.

[3] Emanuele Berti, Enrico Barausse, Vitor Cardoso, Leonardo Gualtieri, Paolo Pani, Ulrich Sperhake, Leo C Stein, Norbert Wex, Kent Yagi, Tessa Baker, et al. Testing general relativity with present and future astrophysical observations. *Classical and Quantum Gravity*, 32(24):243001, 2015.

[4] NV Krishnendu and Frank Ohme. Testing general relativity with gravitational waves: an overview. *Universe*, 7(12):497, 2021.

[5] Albert Einstein. Kosmologische betrachtungen zur allgemeinen relativitätstheorie. *Sitzungsberichte der Königlich Preussischen Akademie der Wissenschaften*, pages 142–152, 1917.

[6] Alexander Friedman. Über die krümmung des raumes. *Zeitschrift für Physik*, 10(1):377–386, 1922.

[7] Edwin Hubble. A relation between distance and radial velocity among extra-galactic nebulae. *Proceedings of the national academy of sciences*, 15(3):168–173, 1929.

[8] Arno A Penzias and Robert W Wilson. A measurement of excess antenna temperature at 4080 mhz. In *A Source Book in Astronomy and Astrophysics, 1900–1975*, pages 873–876. Harvard University Press, 1979.

[9] George Gamow. The evolution of the universe. *Nature*, 162(4122):680–682, 1948.

[10] Ralph A Alpher and Robert Herman. Evolution of the universe. *Nature*, 162(4124):774–775, 1948.

[11] Vera C Rubin and W Kent Ford Jr. Rotation of the andromeda nebula from a spectroscopic survey of emission regions. *Astrophysical Journal, vol. 159, p. 379*, 159:379, 1970.

[12] Fritz Zwicky. Die rotverschiebung von extragalaktischen nebeln. *Helvetica Physica Acta, Vol. 6, p. 110-127*, 6:110–127, 1933.

[13] Saul Perlmutter, G Aldering, M Della Valle, S Deustua, RS Ellis, S Fabbro, A Fruchter, G Goldhaber, DE Groom, IM Hook, et al. Discovery of a supernova explosion at half the age of the universe. *Nature*, 391(6662):51–54, 1998.

[14] Adam G Riess, Alexei V Filippenko, Peter Challis, Alejandro Clocchiatti, Alan Diercks, Peter M Garnavich, Ron L Gilliland, Craig J Hogan, Saurabh Jha, Robert P Kirshner, et al. Observational evidence from supernovae for an accelerating universe and a cosmological constant. *The Astronomical Journal*, 116(3):1009, 1998.

[15] Nabila Aghanim, Yashar Akrami, Mark Ashdown, Jonathan Aumont, Carlo Baccigalupi, Mario Ballardini, Anthony J Banday, RB Barreiro, N Bartolo, S Basak, et al. Planck 2018 results-vi. cosmological parameters. *Astronomy & Astrophysics*, 641:A6, 2020.

[16] Dillon Brout, Dan Scolnic, Brodie Popovic, Adam G Riess, Anthony Carr, Joe Zuntz, Rick Kessler, Tamara M Davis, Samuel Hinton, David Jones, et al. The pantheon+ analysis: cosmological constraints. *The Astrophysical Journal*, 938(2):110, 2022.

[17] Benjamin Giblin, Catherine Heymans, Marika Asgari, Hendrik Hildebrandt, Henk Hoekstra, Benjamin Joachimi, Arun Kannawadi, Konrad Kuijken, Chieh-An Lin, Lance Miller, et al. Kids-1000 catalogue: Weak gravitational lensing shear measurements. *Astronomy & Astrophysics*, 645:A105, 2021.

[18] Timothy MC Abbott, Michel Aguena, Alex Alarcon, S Allam, O Alves, A Amon, F Andrade-Oliveira, James Annis, S Avila, D Bacon, et al. Dark energy survey year 3 results: Cosmological constraints from galaxy clustering and weak lensing. *Physical Review D*, 105(2):023520, 2022.

[19] Alexandra Amon, Daniel Gruen, Michael A Troxel, Niall MacCrann, Scott Dodelson, Ami Choi, Cyrille Doux, Lucas F Secco, Simon Samuroff, Elisabeth Krause, et al. Dark energy survey year 3 results: Cosmology from cosmic shear and robustness to data calibration. *Physical Review D*, 105(2):023514, 2022.

[20] Lucas Frozza Secco, Simon Samuroff, Elisabeth Krause, Bhuvnesh Jain, J Blazek, Marco Raveri, Andresa Campos, Alexandra Amon, Anqi Chen, Cyrille Doux, et al. Dark energy survey year 3 results: Cosmology from cosmic shear and robustness to modeling uncertainty. *Physical Review D*, 105(2):023515, 2022.

[21] Adam G Riess, Wenlong Yuan, Lucas M Macri, Dan Scolnic, Dillon Brout, Stefano Casertano, David O Jones, Yukei Murakami, Gagandeep S Anand, Louise Breuval, et al. A comprehensive measurement of the local value of the hubble constant with 1 km s- 1 mpc- 1 uncertainty from the hubble space telescope and the sh0es team. *The Astrophysical journal letters*, 934(1):L7, 2022.

[22] Steven Weinberg. The cosmological constant problem. *Reviews of modern physics*, 61(1):1, 1989.

[23] Eleonora Di Valentino, Olga Mena, Supriya Pan, Luca Visinelli, Weiqiang Yang, Alessandro Melchiorri, David F Mota, Adam G Riess, and Joseph Silk. In the realm of the hubble tension—a review of solutions. *Classical and Quantum Gravity*, 38(15):153001, 2021.

[24] Ira Wasserman. Degeneracy inherent in the observational determination of the dark energy equation of state. *Physical Review D*, 66(12):123511, 2002.

[25] Claudio Rubano and Paolo Scudellaro. Quintessence or phoenix? *General Relativity and Gravitation*, 34:1931–1939, 2002.

[26] Martin Kunz. Degeneracy between the dark components resulting from the fact that gravity only measures the total energy-momentum tensor. *Physical Review D—Particles, Fields, Gravitation, and Cosmology*, 80(12):123001, 2009.

[27] Alejandro Aviles and Jorge L Cervantes-Cota. Dark degeneracy and interacting cosmic components. *Physical Review D—Particles, Fields, Gravitation, and Cosmology*, 84(8):083515, 2011.

[28] Saulo Carneiro and HA Borges. On dark degeneracy and interacting models. *Journal of Cosmology and Astroparticle Physics*, 2014(06):010, 2014.

[29] R von Marttens, L Casarini, DF Mota, and W Zimdahl. Cosmological constraints on parametrized interacting dark energy. *Physics of the Dark Universe*, 23:100248, 2019.

[30] Rodrigo von Marttens, Lucas Lombriser, Martin Kunz, Valerio Marra, Luciano Casarini, and Jailson Alcaniz. Dark degeneracy i: Dynamical or interacting dark energy? *Physics of the Dark Universe*, 28:100490, 2020.

[31] Rodrigo von Marttens, Dinorah Barbosa, and Jailson Alcaniz. One-parameter dynamical dark-energy from the generalized chaplygin gas. *Journal of Cosmology and Astroparticle Physics*, 2023(04):052, 2023.

[32] Dinorah Barbosa, Rodrigo von Marttens, Javier Gonzalez, and Jailson Alcaniz. Assessing the dark degeneracy through gas mass fraction data. *Physics of the Dark Universe*, 45:101526, 2024.

[33] Daniel Baumann. *Cosmology*. Cambridge University Press, 2022.

[34] Scott Dodelson and Fabian Schmidt. *Modern cosmology*. Academic press, 2020.

[35] Steven Weinberg. *Cosmology*. OUP Oxford, 2008.

[36] Chung-Pei Ma and Edmund Bertschinger. Cosmological perturbation theory in the synchronous and conformal newtonian gauges. *arXiv preprint astro-ph/9506072*, 1995.

[37] Oliver Piattella et al. Lecture notes in cosmology. Technical report, Springer, 2018.

[38] Barbara Ryden. *Introduction to cosmology*. Cambridge University Press, 2017.

[39] Julien Lesgourgues. The cosmic linear anisotropy solving system (class) i: overview. *arXiv preprint arXiv:1104.2932*, 2011.

[40] James M Bardeen. Gauge-invariant cosmological perturbations. *Physical Review D*, 22(8):1882, 1980.

[41] DJ Fixsen. The temperature of the cosmic microwave background. *The Astrophysical Journal*, 707(2):916, 2009.

[42] N Aghanim, C Armitage-Caplan, M Arnaud, M Ashdown, F Atrio-Barandela, J Aumont, AJ Banday, RB Barreiro, JG Bartlett, K Benabed, et al. Planck 2013 results. XXVII. Doppler boosting of the CMB: Eppur si muove. *Astronomy & Astrophysics*, 571:A27, 2014.

[43] Planck collaboration. Planck legacy archive wiki, 2023. https://wiki.cosmos.esa.int/planck-legacy-archive/index.php/File:Cmb_inpaint_T_nilc_v1.png#filelinks [Accessed: 04/11/2024].

[44] Daniel J Eisenstein, Idit Zehavi, David W Hogg, Roman Scoccimarro, Michael R Blanton, Robert C Nichol, Ryan Scranton, Hee-Jong Seo, Max Tegmark, Zheng Zheng, et al. Detection of the baryon acoustic peak in the large-scale correlation function of sdss luminous red galaxies. *The Astrophysical Journal*, 633(2):560, 2005.

[45] Dan Scolnic, Dillon Brout, Anthony Carr, Adam G Riess, Tamara M Davis, Arianna Dwomoh, David O Jones, Noor Ali, Pranav Charvu, Rebecca Chen, et al. The pantheon+ analysis: the full data set and light-curve release. *The Astrophysical Journal*, 938(2):113, 2022.

[46] David H Weinberg, Michael J Mortonson, Daniel J Eisenstein, Christopher Hirata, Adam G Riess, and Eduardo Rozo. Observational probes of cosmic acceleration. *Physics reports*, 530(2):87–255, 2013.

[47] Shin Sasaki. A new method to estimate cosmological parameters using the baryon fraction of clusters of galaxies. *Publications of the Astronomical Society of Japan*, 48(6):L119–L122, 1996.

[48] Vincent R Eke, Julio F Navarro, and Carlos S Frenk. The evolution of x-ray clusters in a low-density universe. *The Astrophysical Journal*, 503(2):569, 1998.

[49] Robert A Crain, Vincent R Eke, Carlos S Frenk, Adrian Jenkins, Ian G McCarthy, Julio F Navarro, and Frazer R Pearce. The baryon fraction of λcdm haloes. *Monthly notices of the royal astronomical society*, 377(1):41–49, 2007.

[50] Scott T Kay, Peter A Thomas, Adrian Jenkins, and Frazer R Pearce. Cosmological simulations of the intracluster medium. *Monthly Notices of the Royal Astronomical Society*, 355(4):1091–1104, 2004.

[51] N Battaglia, JR Bond, C Pfrommer, and JL Sievers. On the cluster physics of sunyaev–zel'dovich and x-ray surveys. iii. measurement biases and cosmological evolution of gas and stellar mass fractions. *The Astrophysical Journal*, 777(2):123, 2013.

[52] Susana Planelles, Stefano Borgani, Klaus Dolag, Stefano Ettori, Dunja Fabjan, Giuseppe Murante, and Luca Tornatore. Baryon census in hydrodynamical simulations of galaxy clusters. *Monthly Notices of the Royal Astronomical Society*, 431(2):1487–1502, 2013.

[53] DE Applegate, A Mantz, SW Allen, A von der Linden, R Glenn Morris, S Hilbert, Patrick L Kelly, DL Burke, H Ebeling, DA Rapetti, et al. Cosmology and astrophysics from relaxed galaxy clusters–iv. robustly calibrating hydrostatic masses with weak lensing. *Monthly Notices of the Royal Astronomical Society*, 457(2):1522–1534, 2016.

[54] Douglas E Applegate, Anja von der Linden, Patrick L Kelly, Mark T Allen, Steven W Allen, Patricia R Burchat, David L Burke, Harald Ebeling, Adam Mantz, and R Glenn Morris. Weighing the giants–iii. methods and measurements of accurate galaxy cluster weak-lensing masses. *Monthly Notices of the Royal Astronomical Society*, 439(1):48–72, 2014.

[55] Adam B Mantz, Steven W Allen, R Glenn Morris, David A Rapetti, Douglas E Applegate, Patrick L Kelly, Anja von der Linden, and Robert W Schmidt.

Cosmology and astrophysics from relaxed galaxy clusters–ii. cosmological constraints. *Monthly Notices of the Royal Astronomical Society*, 440(3):2077–2098, 2014.

[56] SW Allen, DA Rapetti, RW Schmidt, H Ebeling, RG Morris, and AC Fabian. Improved constraints on dark energy from chandra x-ray observations of the largest relaxed galaxy clusters. *Monthly Notices of the Royal Astronomical Society*, 383(3):879–896, 2008.

[57] Adam B Mantz, R Glenn Morris, Steven W Allen, Rebecca EA Canning, Lucie Baumont, Bradford Benson, Lindsey E Bleem, Steven R Ehlert, Benjamin Floyd, Ricardo Herbonnet, et al. Cosmological constraints from gas mass fractions of massive, relaxed galaxy clusters. *Monthly Notices of the Royal Astronomical Society*, 510(1):131–145, 2022.

[58] Gianfranco Bertone, Dan Hooper, and Joseph Silk. Particle dark matter: Evidence, candidates and constraints. *Physics reports*, 405(5-6):279–390, 2005.

[59] Gianfranco Bertone and Tim MP Tait. A new era in the search for dark matter. *Nature*, 562(7725):51–56, 2018.

[60] AG Adame, J Aguilar, S Ahlen, S Alam, DM Alexander, M Alvarez, O Alves, A Anand, U Andrade, E Armengaud, et al. Desi 2024 vi: Cosmological constraints from the measurements of baryon acoustic oscillations. *arXiv preprint arXiv:2404.03002*, 2024.

[61] Ashley J Ross, Lado Samushia, Cullan Howlett, Will J Percival, Angela Burden, and Marc Manera. The clustering of the sdss dr7 main galaxy sample–i. a 4 per cent distance measure at z= 0.15. *Monthly Notices of the Royal Astronomical Society*, 449(1):835–847, 2015.

[62] Shadab Alam, Marie Aubert, Santiago Avila, Christophe Balland, Julian E Bautista, Matthew A Bershady, Dmitry Bizyaev, Michael R Blanton, Adam S Bolton, Jo Bovy, et al. Completed sdss-iv extended baryon oscillation spectroscopic survey: Cosmological implications from two decades of spectroscopic surveys at the apache point observatory. *Physical Review D*, 103(8):083533, 2021.

[63] Tilman Tröster, Marika Asgari, Chris Blake, Matteo Cataneo, Catherine Heymans, Hendrik Hildebrandt, Benjamin Joachimi, Chieh-An Lin, Ariel G Sánchez, Angus H Wright, et al. Kids-1000 cosmology: constraints beyond flat λcdm. *Astronomy & Astrophysics*, 649:A88, 2021.

[64] Jerome Martin. Everything you always wanted to know about the cosmological constant problem (but were afraid to ask). *Comptes Rendus Physique*, 13(6-7):566–665, 2012.

[65] Steven Weinberg. The cosmological constant problems. In *Sources and Detection of Dark Matter and Dark Energy in the Universe: Fourth International Symposium Held at Marina del Rey, CA, USA February 23–25, 2000*, pages 18–26. Springer, 2001.

[66] Licia Verde, Tommaso Treu, and Adam G Riess. Tensions between the early and late universe. *Nature Astronomy*, 3(10):891–895, 2019.

[67] Théo Simon, Pierre Zhang, Vivian Poulin, and Tristan L Smith. Consistency of effective field theory analyses of the boss power spectrum. *Physical Review D*, 107(12):123530, 2023.

[68] Oliver HE Philcox and Mikhail M Ivanov. Boss dr12 full-shape cosmology: λ cdm constraints from the large-scale galaxy power spectrum and bispectrum monopole. *Physical Review D*, 105(4):043517, 2022.

[69] Pierre Zhang, Guido D'Amico, Leonardo Senatore, Cheng Zhao, and Yifu Cai. Boss correlation function analysis from the effective field theory of large-scale structure. *Journal of Cosmology and Astroparticle Physics*, 2022(02):036, 2022.

[70] Chiaki Hikage, Masamune Oguri, Takashi Hamana, Surhud More, Rachel Mandelbaum, Masahiro Takada, Fabian Köhlinger, Hironao Miyatake, Atsushi J Nishizawa, Hiroaki Aihara, et al. Cosmology from cosmic shear power spectra with subaru hyper suprime-cam first-year data. *Publications of the Astronomical Society of Japan*, 71(2):43, 2019.

[71] Pedro G Ferreira. Cosmological tests of gravity. *Annual Review of Astronomy and Astrophysics*, 57(1):335–374, 2019.

[72] EM Barboza Jr and JS Alcaniz. A parametric model for dark energy. *Physics Letters B*, 666(5):415–419, 2008.

[73] Michel Chevallier and David Polarski. Accelerating universes with scaling dark matter. *International Journal of Modern Physics D*, 10(02):213–223, 2001.

[74] Eric V Linder. Exploring the expansion history of the universe. *Physical review letters*, 90(9):091301, 2003.

[75] Shinji Tsujikawa. Quintessence: a review. *Classical and Quantum Gravity*, 30(21):214003, 2013.

[76] Vivian Poulin, Tristan L Smith, and Tanvi Karwal. The ups and downs of early dark energy solutions to the hubble tension: a review of models, hints and constraints circa 2023. *Physics of the Dark Universe*, page 101348, 2023.

[77] Hermano ES Velten, RF Vom Marttens, and Winifried Zimdahl. Aspects of the cosmological "coincidence problem". *The European Physical Journal C*, 74:1–8, 2014.

[78] Murat Özer and MO Taha. A possible solution to the main cosmological problems. *Physics Letters B*, 171(4):363–365, 1986.

[79] Katherine Freese, Fred C Adams, Joshua A Frieman, and Emil Mottola. Cosmology with decaying vacuum energy. *Nuclear Physics B*, 287:797–814, 1987.

[80] JC Carvalho, JAS Lima, and I Waga. Cosmological consequences of a time-dependent λ term. *Physical Review D*, 46(6):2404, 1992.

[81] Miao Li. A model of holographic dark energy. *Physics Letters B*, 603(1-2):1–5, 2004.

[82] Baojiu Li and Hongsheng Zhao. Structure formation by the fifth force: Segregation of baryons and dark matter. *Physical Review D—Particles, Fields, Gravitation, and Cosmology*, 81(10):104047, 2010.

[83] David F Mota and John D Barrow. Local and global variations of the fine-structure constant. *Monthly Notices of the Royal Astronomical Society*, 349(1):291–302, 2004.

[84] Justin Khoury and Amanda Weltman. Chameleon cosmology. *Physical Review D*, 69(4):044026, 2004.

[85] Bin Wang, Elcio Abdalla, Fernando Atrio-Barandela, and Diego Pavon. Dark matter and dark energy interactions: theoretical challenges, cosmological implications and observational signatures. *Reports on Progress in Physics*, 79(9):096901, 2016.

[86] Yuri L Bolotin, Alexander Kostenko, Oleg A Lemets, and Danylo A Yerokhin. Cosmological evolution with interaction between dark energy and dark matter. *International Journal of Modern Physics D*, 24(03):1530007, 2015.

[87] Maria Belén Gavela, D Hernandez, L Lopez Honorez, Olga Mena, and Stefano Rigolin. Dark coupling. *Journal of Cosmology and Astroparticle Physics*, 2009(07):034, 2009.

[88] Eleonora Di Valentino, Alessandro Melchiorri, Olga Mena, and Sunny Vagnozzi. Interacting dark energy in the early 2020s: A promising solution to the h0 and cosmic shear tensions. *Physics of the Dark Universe*, 30:100666, 2020.

[89] Eleonora Di Valentino, Alessandro Melchiorri, Olga Mena, and Sunny Vagnozzi. Nonminimal dark sector physics and cosmological tensions. *Physical Review D*, 101(6):063502, 2020.

[90] William Giarè, Miguel A Sabogal, Rafael C Nunes, and Eleonora Di Valentino. Interacting dark energy after desi baryon acoustic oscillation measurements. *arXiv preprint arXiv:2404.15232*, 2024.

[91] Weiqiang Yang, Supriya Pan, Eleonora Di Valentino, Olga Mena, and Alessandro Melchiorri. 2021-h0 odyssey: closed, phantom and interacting dark energy cosmologies. *Journal of Cosmology and Astroparticle Physics*, 2021(10):008, 2021.

[92] Ashadul Halder and Madhurima Pandey. Probing the effects of primordial black holes on 21-cm edges signal along with interacting dark energy and dark matter–baryon scattering. *Monthly Notices of the Royal Astronomical Society*, 508(3):3446–3454, 2021.

[93] Peng Wang and Xin-He Meng. Can vacuum decay in our universe? *Classical and Quantum Gravity*, 22(2):283, 2004.

[94] Jailson S Alcaniz and José Ademir Sales de Lima. Interpreting cosmological vacuum decay. *Physical Review D—Particles, Fields, Gravitation, and Cosmology*, 72(6):063516, 2005.

[95] Diego Pavon and Winfried Zimdahl. Holographic dark energy and cosmic coincidence. *Physics Letters B*, 628(3-4):206–210, 2005.

[96] Gabriela Caldera-Cabral, Roy Maartens, and Bjoern Malte Schaefer. The growth of structure in interacting dark energy models. *Journal of Cosmology and Astroparticle Physics*, 2009(07):027, 2009.

[97] Gabriela Caldera-Cabral, Roy Maartens, and L Arturo Urena-Lopez. Dynamics of interacting dark energy. *Physical Review D*, 79(6):063518, 2009.

[98] Michael S Turner. Coherent scalar-field oscillations in an expanding universe. *Physical Review D*, 28(6):1243, 1983.

[99] Murli Manohar Verma. Dark energy as a manifestation of the non-constant cosmological constant. *Astrophysics and Space Science*, 330:101–105, 2010.

[100] HA Borges, S Carneiro, JC Fabris, and C Pigozzo. Evolution of density perturbations in decaying vacuum cosmology. *Physical Review D*, 77(4):043513, 2008.

[101] Eleonora Di Valentino, Alessandro Melchiorri, Olga Mena, Supriya Pan, and Weiqiang Yang. Interacting dark energy in a closed universe. *Monthly Notices of the Royal Astronomical Society: Letters*, 502(1):L23–L28, 2021.

[102] Suresh Kumar and Rafael C Nunes. Echo of interactions in the dark sector. *Physical Review D*, 96(10):103511, 2017.

[103] Weiqiang Yang, Supriya Pan, Lixin Xu, and David F Mota. Effects of anisotropic stress in interacting dark matter–dark energy scenarios. *Monthly Notices of the Royal Astronomical Society*, 482(2):1858–1871, 2019.

[104] Mark S Linton, Alkistis Pourtsidou, Robert Crittenden, and Roy Maartens. Variable sound speed in interacting dark energy models. *Journal of Cosmology and Astroparticle Physics*, 2018(04):043, 2018.

[105] Luis P Chimento. Linear and nonlinear interactions in the dark sector. *Physical Review D—Particles, Fields, Gravitation, and Cosmology*, 81(4):043525, 2010.

[106] Pedro Carrilho, Chiara Moretti, Benjamin Bose, Katarina Markovič, and Alkistis Pourtsidou. Interacting dark energy from redshift-space galaxy clustering. *Journal of Cosmology and Astroparticle Physics*, 2021(10):004, 2021.

[107] Jussi Väliviita, Elisabetta Majerotto, and Roy Maartens. Large-scale instability in interacting dark energy and dark matter fluids. *Journal of Cosmology and Astroparticle Physics*, 2008(07):020, 2008.

[108] Weiqiang Yang, Supriya Pan, and David F Mota. Novel approach toward the large-scale stable interacting dark-energy models and their astronomical bounds. *Physical Review D*, 96(12):123508, 2017.

[109] Elisabetta Majerotto, Jussi Väliviita, and Roy Maartens. Adiabatic initial conditions for perturbations in interacting dark energy models. *Monthly Notices of the Royal Astronomical Society*, 402(4):2344–2354, 2010.

[110] Luca Amendola, Gabriela Camargo Campos, and Rogerio Rosenfeld. Consequences of dark matter-dark energy interaction on cosmological parameters derived<? format?> from type ia supernova data. *Physical Review D—Particles, Fields, Gravitation, and Cosmology*, 75(8):083506, 2007.

[111] Sergio Del Campo, Ramon Herrera, German Olivares, and Diego Pavon. Interacting models of soft coincidence. *Physical Review D*, 74(2):023501, 2006.

[112] Gabriel A. Hoerning, Ricardo G. Landim, Luiza O. Ponte, Raphael P. Rolim, Filipe B. Abdalla, and Elcio Abdalla. Constraints on interacting dark energy revisited: implications for the Hubble tension. 8 2023.

[113] Matteo Lucca and Deanna C. Hooper. Shedding light on dark matter-dark energy interactions. *Physical Review D*, 102(12), December 2020.

[114] Yuejia Zhai, William Giarè, Carsten van de Bruck, Eleonora Di Valentino, Olga Mena, and Rafael C Nunes. A consistent view of interacting dark energy from multiple cmb probes. *Journal of Cosmology and Astroparticle Physics*, 2023(07):032, 2023.

[115] Antonella Cid, Beethoven Santos, Cassio Pigozzo, Tassia Ferreira, and Jailson Alcaniz. Bayesian comparison of interacting scenarios. *Journal of Cosmology and Astroparticle Physics*, 2019(03):030, 2019.

[116] R von Marttens, HA Borges, S Carneiro, JS Alcaniz, and W Zimdahl. Unphysical properties in a class of interacting dark energy models. *The European Physical Journal C*, 80(12):1110, 2020.

[117] Miguel Quartin, Mauricio O Calvao, Sergio E Joras, Ribamar RR Reis, and Ioav Waga. Dark interactions and cosmological fine-tuning. *Journal of Cosmology and Astroparticle Physics*, 2008(05):007, 2008.

[118] Luis P Chimento, Alejandro S Jakubi, Diego Pavon, and Winfried Zimdahl. Interacting quintessence solution to the coincidence problem. *Physical Review D*, 67(8):083513, 2003.

[119] Karim A Malik, David Wands, and Carlo Ungarelli. Large-scale curvature and entropy perturbations for multiple interacting fluids. *Physical Review D*, 67(6):063516, 2003.

[120] Renyue Cen. Decaying cold dark matter model and small-scale power. *The Astrophysical Journal*, 546(2):L77, 2001.

[121] Houri Ziaeepour. Quintessence from the decay of superheavy dark matter. *Physical Review D*, 69(6), March 2004.

[122] Eleonora Di Valentino, Alessandro Melchiorri, and Olga Mena. Can interacting dark energy solve the h 0 tension? *Physical Review D*, 96(4):043503, 2017.

[123] M Lucca and DC Hooper. Tensions in the dark: shedding light on dark matter-dark energy interactions (2020). *arXiv preprint arXiv:2002.06127*.

[124] Adam G. Riess, Stefano Casertano, Wenlong Yuan, Lucas M. Macri, and Dan Scolnic. Large magellanic cloud cepheid standards provide a 1 *The Astrophysical Journal*, 876(1):85, May 2019.

[125] Daniel Moshe Scolnic, DO Jones, A Rest, YC Pan, R Chornock, RJ Foley, ME Huber, R Kessler, Gautham Narayan, AG Riess, et al. The complete light-curve sample of spectroscopically confirmed SNe Ia from Pan-STARRS1 and cosmological constraints from the combined pantheon sample. *The Astrophysical Journal*, 859(2):101, 2018.

[126] Rodrigo Von Marttens, Javier E Gonzalez, Jailson Alcaniz, Valerio Marra, and Luciano Casarini. Model-independent reconstruction of dark sector interactions. *Physical Review D*, 104(4):043515, 2021.

[127] T Harko, K Asadi, H Moshafi, and H Sheikhahmadi. Observational constraints on the interacting dark energy—dark matter (idm) cosmological models. *Physics of the Dark Universe*, 38:101131, 2022.

[128] Winfried Zimdahl and Diego Pavón. Statefinder parameters for interacting dark energy. *General Relativity and Gravitation*, 36:1483–1491, 2004.

[129] Maria Tsedrik, Chiara Moretti, Pedro Carrilho, Federico Rizzo, and Alkistis Pourtsidou. Interacting dark energy from the joint analysis of the power spectrum and bispectrum multipoles with the eftoflss. *Monthly Notices of the Royal Astronomical Society*, 520(2):2611–2632, 2023.

[130] Marco Baldi, Valeria Pettorino, Georg Robbers, and Volker Springel. Hydrodynamical n-body simulations of coupled dark energy cosmologies. *Monthly Notices of the Royal Astronomical Society*, 403(4):1684–1702, 2010.

[131] Gary Bernstein. Metric tests for curvature from weak lensing and baryon acoustic oscillations. *The Astrophysical Journal*, 637(2):598, 2006.

[132] Robert R Caldwell and Marc Kamionkowski. Expansion, geometry, and gravity. *Journal of Cosmology and Astroparticle Physics*, 2004(09):009, 2004.

[133] Lucas Lombriser and Andy Taylor. Classifying linearly shielded modified gravity models in effective field theory. *Physical Review Letters*, 114(3):031101, 2015.

[134] Lucas Lombriser and Andy Taylor. Breaking a dark degeneracy with gravitational waves. *Journal of Cosmology and Astroparticle Physics*, 2016(03):031, 2016.

[135] Lucas Lombriser and Nelson A Lima. Challenges to self-acceleration in modified gravity from gravitational waves and large-scale structure. *Physics Letters B*, 765:382–385, 2017.

[136] Ignacy Sawicki, Ippocratis D Saltas, Mariele Motta, Luca Amendola, and Martin Kunz. Nonstandard gravitational waves imply gravitational slip: On the difficulty of partially hiding new gravitational degrees of freedom. *Physical Review D*, 95(8):083520, 2017.

[137] Rodrigo F vom Marttens, Luciano Casarini, William S Hipólito-Ricaldi, and Winfried Zimdahl. Cmb and matter power spectra with non-linear dark-sector interactions. *Journal of Cosmology and Astroparticle Physics*, 2017(01):050, 2017.

[138] Pierre Astier, J Guy, N Regnault, R Pain, E Aubourg, D Balam, S Basa, RG Carlberg, S Fabbro, D Fouchez, et al. The supernova legacy survey: measurement of, and w from the first year data set. *Astronomy & Astrophysics*, 447(1):31–48, 2006.

[139] William J Wolf and Pedro G Ferreira. Underdetermination of dark energy. *Physical Review D*, 108(10):103519, 2023.

[140] Michele Moresco, Lucia Pozzetti, Andrea Cimatti, Raul Jimenez, Claudia Maraston, Licia Verde, Daniel Thomas, Annalisa Citro, Rita Tojeiro, and David Wilkinson. A 6% measurement of the hubble parameter at z 0.45: direct evidence of the epoch of cosmic re-acceleration. *Journal of Cosmology and Astroparticle Physics*, 2016(05):014, 2016.

[141] Florian Beutler, Chris Blake, Matthew Colless, D Heath Jones, Lister Staveley-Smith, Lachlan Campbell, Quentin Parker, Will Saunders, and Fred Watson. The 6df galaxy survey: baryon acoustic oscillations and the local hubble constant. *Monthly Notices of the Royal Astronomical Society*, 416(4):3017–3032, 2011.

[142] Shadab Alam, Metin Ata, Stephen Bailey, Florian Beutler, Dmitry Bizyaev, Jonathan A Blazek, Adam S Bolton, Joel R Brownstein, Angela Burden, Chia-Hsun Chuang, et al. The clustering of galaxies in the completed sdss-iii baryon oscillation spectroscopic survey: cosmological analysis of the dr12 galaxy sample. *Monthly Notices of the Royal Astronomical Society*, 470(3):2617–2652, 2017.

[143] Antony Lewis. GetDist: a Python package for analysing Monte Carlo samples. *arXiv preprint arXiv:1910.13970*, 2019.

[144] M.C. Bento, O. Bertolami, and A.A. Sen. Generalized Chaplygin gas, accelerated expansion and dark energy matter unification. *Phys. Rev. D*, 66:043507, 2002.

[145] J. S. Alcaniz, Deepak Jain, and Abha Dev. High - redshift objects and the generalized Chaplygin gas. *Phys. Rev. D*, 67:043514, 2003.

[146] J. V. Cunha, J. S. Alcaniz, and J. A. S. Lima. Cosmological constraints on Chaplygin gas dark energy from galaxy clusters x-ray and supernova data. *Phys. Rev. D*, 69:083501, 2004.

[147] V. Gorini, A.Y. Kamenshchik, U. Moschella, O.F. Piattella, and A.A. Starobinsky. Gauge-invariant analysis of perturbations in Chaplygin gas unified models of dark matter and dark energy. *JCAP*, 02:016, 2008.

[148] Oliver F. Piattella. The extreme limit of the generalized Chaplygin gas. *JCAP*, 03:012, 2010.

[149] J.C. Fabris, S.V.B. Goncalves, H.E.S. Velten, and W. Zimdahl. Matter Power Spectrum for the Generalized Chaplygin Gas Model: The Newtonian Approach. *Phys. Rev. D*, 78:103523, 2008.

[150] Alexander Yu. Kamenshchik, Ugo Moschella, and Vincent Pasquier. An Alternative to quintessence. *Phys. Lett. B*, 511:265–268, 2001.

[151] J.C. Fabris, S.V.B. Goncalves, and P.E. de Souza. Density perturbations in a universe dominated by the Chaplygin gas. *Gen. Rel. Grav.*, 34:53–63, 2002.

[152] Neven Bilic, Gary B. Tupper, and Raoul D. Viollier. Unification of dark matter and dark energy: The Inhomogeneous Chaplygin gas. *Phys. Lett. B*, 535:17–21, 2002.

[153] Abha Dev, Deepak Jain, and J. S. Alcaniz. Cosmological consequences of a Chaplygin gas dark energy. *Phys. Rev. D*, 67:023515, 2003.

[154] Weiqiang Yang, Supriya Pan, Sunny Vagnozzi, Eleonora Di Valentino, David F. Mota, and Salvatore Capozziello. Dawn of the dark: unified dark sectors and the EDGES Cosmic Dawn 21-cm signal. *JCAP*, 11:044, 2019.

[155] Havard Sandvik, Max Tegmark, Matias Zaldarriaga, and Ioav Waga. The end of unified dark matter? *Phys. Rev. D*, 69:123524, 2004.

[156] R.R.R. Reis, Ioav Waga, M.O. Calvao, and S.E. Joras. Entropy perturbations in quartessence Chaplygin models. *Phys. Rev. D*, 68:061302, 2003.

[157] W.S. Hipolito-Ricaldi, H.E.S. Velten, and W. Zimdahl. Non-adiabatic dark fluid cosmology. *JCAP*, 06:016, 2009.

[158] W.S. Hipolito-Ricaldi, H.E.S. Velten, and W. Zimdahl. The Viscous Dark Fluid Universe. *Phys. Rev. D*, 82:063507, 2010.

[159] Xin Zhang, Feng-Quan Wu, and Jingfei Zhang. A New generalized Chaplygin gas as a scheme for unification of dark energy and dark matter. *JCAP*, 01:003, 2006.

[160] David Wands, Josue De-Santiago, and Yuting Wang. Inhomogeneous vacuum energy. *Class. Quant. Grav.*, 29:145017, 2012.

[161] Yun-He Li and Xin Zhang. Large-scale stable interacting dark energy model: Cosmological perturbations and observational constraints. *Phys. Rev. D*, 89(8):083009, 2014.

[162] Yuting Wang, David Wands, Lixin Xu, Josue De-Santiago, and Alireza Hojjati. Cosmological constraints on a decomposed Chaplygin gas. *Phys. Rev. D*, 87(8):083503, 2013.

[163] Yuting Wang, David Wands, Gong-Bo Zhao, and Lixin Xu. Post-*Planck* constraints on interacting vacuum energy. *Phys. Rev. D*, 90(2):023502, 2014.

[164] R.F. vom Marttens, L. Casarini, W. Zimdahl, W.S. Hipólito-Ricaldi, and D.F. Mota. Does a generalized Chaplygin gas correctly describe the cosmological dark sector? *Phys. Dark Univ.*, 15:114–124, 2017.

[165] Micol Benetti, Welber Miranda, Humberto A. Borges, Cassio Pigozzo, Saulo Carneiro, and Jailson S. Alcaniz. Looking for interactions in the cosmological dark sector. *JCAP*, 12:023, 2019.

[166] Micol Benetti, Humberto Borges, Cassio Pigozzo, Saulo Carneiro, and Jailson Alcaniz. Dark sector interactions and the curvature of the universe in light of Planck's 2018 data. *JCAP*, 08:014, 2021.

[167] Thejs Brinckmann and Julien Lesgourgues. Montepython 3: boosted mcmc sampler and other features. *Physics of the Dark Universe*, 24:100260, 2019.

[168] Ashley J. Ross, Lado Samushia, Cullan Howlett, Will J. Percival, Angela Burden, and Marc Manera. The clustering of the SDSS DR7 main Galaxy sample – I. A 4 per cent distance measure at $z = 0.15$. *Mon. Not. Roy. Astron. Soc.*, 449(1):835–847, 2015.

[169] Shadab Alam et al. The clustering of galaxies in the completed SDSS-III Baryon Oscillation Spectroscopic Survey: cosmological analysis of the DR12 galaxy sample. *Mon. Not. Roy. Astron. Soc.*, 470(3):2617–2652, 2017.

[170] Shadab Alam et al. Completed SDSS-IV extended Baryon Oscillation Spectroscopic Survey: Cosmological implications from two decades of spectroscopic surveys at the Apache Point Observatory. *Phys. Rev. D*, 103(8):083533, 2021.

[171] Uendert Andrade, Dhayaa Anbajagane, Rodrigo von Marttens, Dragan Huterer, and Jailson Alcaniz. A test of the standard cosmological model with geometry and growth. *Journal of Cosmology and Astroparticle Physics*, 2021(11):014, 2021.

[172] Planck Collaboration, N Aghanim, Y Akrami, M Ashdown, J Aumont, C Baccigalupi, M Ballardini, AJ Banday, RB Barreiro, N Bartolo, et al. Planck 2018 results. V. CMB power spectra and likelihoods. *Astronomy & Astrophysics*, 2020.

[173] K Kuijken, C Heymans, A Dvornik, H Hildebrandt, JTA de Jong, AH Wright, T Erben, M Bilicki, B Giblin, H-Y Shan, et al. The fourth data release of the kilo-degree survey: ugri imaging and nine-band optical-ir photometry over 1000 square degrees. *Astronomy & Astrophysics*, 625:A2, 2019.

[174] Peter Schneider, Ludovic Van Waerbeke, and Yannick Mellier. B-modes in cosmic shear from source redshift clustering. *Astron. Astrophys.*, 389:729–741, 2002.

[175] Alexander Mead, Catherine Heymans, Lucas Lombriser, John Peacock, Olivia Steele, and Hans Winther. Accurate halo-model matter power spectra with dark energy, massive neutrinos and modified gravitational forces. *Mon. Not. Roy. Astron. Soc.*, 459(2):1468–1488, 2016.

[176] Supriya Pan, German S. Sharov, and Weiqiang Yang. Field theoretic interpretations of interacting dark energy scenarios and recent observations. *Phys. Rev. D*, 101:103533, May 2020.

[177] Sveva Castello, Stéphane Ilić, and Martin Kunz. A cautionary tale: Dark energy in single-field, slow-roll inflationary models. *arXiv preprint arXiv:2203.08762*, 2022.

[178] Adam G Riess, Stefano Casertano, Wenlong Yuan, J Bradley Bowers, Lucas Macri, Joel C Zinn, and Dan Scolnic. Cosmic distances calibrated to 1% precision with gaia EDR3 parallaxes and Hubble space telescope photometry of 75 Milky Way cepheids confirm tension with ΛCDM. *The Astrophysical Journal Letters*, 908(1):L6, 2021.

[179] Benjamin Audren, Julien Lesgourgues, Karim Benabed, and Simon Prunet. Conservative Constraints on Early Cosmology: an illustration of the Monte Python cosmological parameter inference code. *JCAP*, 1302:001, 2013.

[180] Ryan J Cooke, Max Pettini, Regina A Jorgenson, Michael T Murphy, and Charles C Steidel. Precision measures of the primordial abundance of deuterium. *The Astrophysical Journal*, 781(1):31, 2014.